Copper diffusion in In_2S_3 and charge separation at In_2S_3/CuSCN and TiO_2/In_2S_3 interfaces

A dissertation submitted to the

Physics Department, Freie Universität Berlin

for the award of the degree of

Doctor of Natural Science (Dr. rer. nat.)

Presented by

Albert Owino Juma

(Kakamega, Kenya)

November, 2013

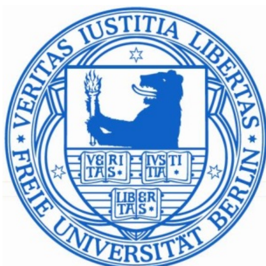

Examiners: 1. PD. Dr. Thomas Dittrich

2. Prof. Dr. Martin Weinelt

Thesis defended on 29.11.2013

ABSTRACT

The concept of inorganic nanostructured solar cells consists of a very thin absorber layer sandwiched between highly structured electron and hole conductors. When a $TiO_2/In_2S_3/CuSCN$ nanocomposite heterostructure is illuminated with light, photo-generated electrons in In_2S_3 can be injected into the conduction band of TiO_2 and holes into the valence band of CuSCN. Charge transfer at the interfaces is limited by the deposition parameters, band alignment and diffusion of Cu from CuSCN into In_2S_3, which was the focus of this work. TiO_2 nanoparticles were screen printed onto SnO_2:F (FTO)-coated glass substrates to give a layer of nanoporous (np) TiO_2. In_2S_3 layers were deposited by thermal evaporation or ion layer gas reaction (ILGAR) methods producing Cl-free ($In(acac)_3$ precursor) and Cl-containing ($InCl_3$ precursor) layers. A spray-spin method was developed for deposition of CuSCN onto In_2S_3. Diffusion of Cu into In_2S_3 layers was investigated by Rutherford backscattering spectrometry (RBS) while charge transport mechanisms were studied with surface photovoltage (SPV) technique in the fixed capacitor configuration. The activation energy (E_a) for Cu diffusion in thermally evaporated and Cl-free ILGAR In_2S_3 layers was 0.30 and 0.24 eV, respectively but increased to between 0.72 and 0.78 eV for Cl-containing In_2S_3 with residual Cl concentrations of 7.8 – 13.8 at.%. The diffusion prefactor (D_0) was six orders of magnitude higher for Cl-containing compared to Cl-free layers. The relationship between E_a and D_0 was described by the Meyer-Neldel rule with a Meyer-Neldel energy of 40 meV. The presence of Cl has no significant influence on the structural properties of In_2S_3 but resulted in a modified diffusion mechanism for Cu diffusion. The photovoltage of In_2S_3/CuSCN samples decreased after annealing for longer than 2 min at 200°C. A defect band was formed near the interface where holes accumulated and electrons tunneled through traps to recombine. The minimum distribution of tail states and hence the lowest disorder was achieved for Cl-containing In_2S_3 layers. The conduction band offset at the np-TiO_2/In_2S_3 interface was 0.05 and 0.30 eV for Cl-free and Cl-containing In_2S_3, respectively. Bulk or interface recombination mechanism dominated charge transport at the interface with Cl-free or Cl-containing In_2S_3, respectively.

Table of Contents

1. Introduction 1

2. Diffusion and electronic processes at disordered interfaces 7

    2.1. Extremely thin absorber and nanocomposite solar cells 7

    2.2. Atom and ion diffusion in solids 9

        2.2.1. Diffusion mechanisms 10

        2.2.2. Cu diffusion in solar cells 13

        2.2.3. Cu in In_2S_3 14

        2.2.4. Meyer-Neldel rule for atom diffusion 15

    2.3. Electronic transport in disordered semiconductors 17

        2.3.1. Electronic transport in the conduction band 18

        2.3.2. The multiple trapping transport model 19

        2.3.3. The hopping transport model 20

        2.3.4. Trap-limited transport in nanocomposites 22

    2.4. Interface formation 23

        2.4.1. Semiconductor heterojunctions 23

        2.4.2. Charge transport at heterojunction interfaces 26

        2.4.3. Interface states and Fermi level pinning 28

3. Experimental methods 31

    3.1. Sample preparation 31

        3.1.1. Thermal evaporation of In_2S_3 31

        3.1.2. Ion layer gas reaction of In_2S_3 33

        3.1.3. Spray-spin deposition of CuSCN 36

        3.1.4. Sample preparation for investigation of Cu (I) diffusion in In_2S_3 layers37

        3.1.5. Screen printing of nanoporous TiO_2 layers 39

    3.2. Rutherford backscattering spectrometry analysis 40

        3.2.1. Instrumentation for Rutherford backscattering analysis 40

        3.2.2. Fundamentals of Rutherford backscattering spectrometry 42

Kinematic factor and mass resolution 42

Scattering cross section 45

Energy loss and depth profiling 46

3.2.3. Experimental conditions and analysis of depth profiles 47

3.3. Surface photovoltage and surface analysis 50

3.3.1. Surface photovoltage principle 51

3.3.2. Spectral dependent surface photovoltage measurements 52

3.3.3. Transient surface photovoltage measurements 55

3.3.4. Ultraviolet photoelectron spectroscopy 55

3.4. Structural and optical properties of In_2S_3 layers 57

3.4.1. Phase analysis by X-ray diffraction 57

3.4.2. Morphology and thickness analysis of In_2S_3 layers 58

3.4.3. Optical characterization of In_2S_3 thin films 60

4. Copper diffusion in In_2S_3 layers 63

4.1. Copper distribution in In_2S_3 layers 63

4.1.1. Cu diffusion in thermally evaporated In_2S_3 layers 63

4.1.2. Cu diffusion in In_2S_3 layers deposited from $In(acac)_3$ precursor 68

4.1.3. Cu diffusion in In_2S_3 layers deposited from $InCl_3$ precursor 74

4.2. Diffusion coefficients and mechanisms 81

4.2.1. One dimensional diffusion model 81

4.2.2. Thermal activation of Cu diffusion 86

4.2.3. The role of Cl on Cu diffusion in In_2S_3 layers 89

5. Charge separation at In_2S_3/CuSCN interfaces 95

5.1. Spectral dependent charge separation at In_2S_3/CuSCN interfaces 95

5.1.1. Role of layer thickness for charge separation in In_2S_3 layers 95

5.1.2. Role of annealing temperature for charge separation at In_2S_3/CuSCN interfaces 100

5.1.3. Modulated charge separation in In_2S_3:Cu layers 108

5.2. Time dependent relaxation of separated charge carriers at In_2S_3/CuSCN interfaces 110

5.2.1. Relaxation of photo-generated charge carriers in In_2S_3 layers 110

5.2.2. Role of annealing temperature for relaxation of separated charge carriers at In_2S_3/CuSCN interfaces 112

5.2.3. Surface photovoltage transients for PVD-In_2S_3:Cu.......................... 115

5.3. Correlation of the density of Cu at ZnO-nanorod/In_2S_3 interfaces with ZnO-nr/In_2S_3/CuSCN solar cells 117

6. Charge separation across np-TiO_2/In_2S_3 interfaces 121

6.1. Work function analysis and optical band gap 121

6.2. Charge transfer across np-TiO_2/ILGAR(Cl)-In_2S_3 interface 124

6.3. Charge transfer across np-TiO_2/ILGAR(acac)-In_2S_3 interface 130

6.4. Band diagram of TiO_2/In_2S_3 interface... 135

7. Summary and outlook 139

8. References.. 143

List of publications 160

Acknowledgements.. 162

Curriculum Vitae 164

1. Introduction

The sun is the largest source of energy, from which 3.9 x 10^{24} J = 1.08 x 10^{18} KWh of energy reach the earth per year [1]. This is about ten thousand times more than the annual global primary energy demand and much more than all the energy reserves available on earth. Solar energy can be converted into electricity or heat for human use. Solar cells convert solar irradiance directly into electricity. Advancement in solar cell technology and increasing installation of photovoltaic (PV) systems across the world has led to a decrease in the cost of solar power generation [2]. The PV market demands that stakeholders should work towards reduction of the production cost and improvement of solar conversion efficiency of the PV modules.

The stability of the PV modules over time is important in addressing the problem of sustainability. This requires knowledge of the degradation rates of the various PV technologies. A high degradation rate translates directly into less power production and reduced future cash flows [3]. The degradation rates for c-Si solar modules are about 0.5 %/year and are due to losses in the fill factor and in the short circuit current density [3]. For a-Si, the degradation rate is approximately 1 %/year. The degradation rates in $Cu(In,Ga)Se_2$ (CIGS) have been studied for relatively shorter periods of time and they can vary significantly depending on the module type and location. The primary loss mechanism in CIGS solar cells is related to an increase in the series resistance. An array of CIGS in Germany evaluated after 6 years of operation for different temperatures and irradiance windows showed no degradation [4]. A CdTe system analyzed in Colorado, USA degrades at 0.6 %/year. In Germany similar modules were found to be stable. Thin film degradation rates improved significantly within the last few years but the impact of the climate is yet to be satisfactorily addressed [3].

The photovoltaic effect was first discovered in 1839 by Becquerel when he shed light onto an AgCl electron in an electrolyte solution [5]. The first pn junction solar cell was fabricated in Bell Laboratories and patented in 1946 [6]. Single crystal and multi-

crystalline Si solar cells, based on the pn junction concept, dominate the PV market today due to its well developed technology, high material quality and stability, abundance and good passivation abilities. The conversion efficiency has reached close to 25%. The disadvantage is the high production cost and indirect band gap which limits effective light absorption [7].

Alternative materials and technologies have been proposed over the years for low cost and efficient solar cells. Cu_2S/CdS was, for a long time, the most developed and efficient solar cell with an efficiency of more than 9 % [8]. Later attention shifted to amorphous Si solar cells employing *p-i-n* configuration, which have reached an efficiency of about 10 % [7]. Chalcopyrite $Cu(In,Ga)Se_2$ thin film solar cells with CdS buffer layer have attained an efficiency of 20.3 % on laboratory scale [9]. Cadmium telluride (CdTe) thin films have a direct band gap of 1.45 eV ideal for PV application. A certified record efficiency of 18.7% for CdTe solar cells has already been reached [10]. A problem with the CdTe solar cells is the toxicity of Cd.

The use of nanostructured and new materials in emerging PV technologies has the potential to increase the efficiency of solar cells and to reduce production costs significantly [7]. Oriented nanowires, nanorods and nanoporous inorganic structured substrates filled with organic or inorganic sensitizers have the advantage of large donor-acceptor interfacial area, continuous and minimum conduction path for charge carriers. Light scattering and trapping enhances absorption and increases the conversion efficiency. Si and ZnO nanowires and TiO_2 nanoporous structures have been tasted for PV application and they show good potential for cheaper solar cells.

Among the emerging technologies is the concept of inorganic solid state nanostructured solar cells [11]. Dye sensitized solar cells have already received much attention and they have inspired the development of new concepts based on nanostructured substrates. The record efficiency now stands at 15 % for sensitization with $CH_3NH_3PbI_3$ perovskite [12]. The concept of ultra-thin nanocomposite absorbers aims to increase the diffusion length of the absorber material; for example, it has been shown that the diffusion length can be increased by one order of magnitude in a np-TiO_2/In_2S_3 nanocomposite absorber [13]. The extremely thin absorber solar cell introduced by Koenenkamp [14] consists of a very thin absorber layer sandwiched between highly structured transparent electron and hole conductors which enhance light management

and increase absorption. Examples of nanostructured solar cells include ZnO-nr/In_2S_3/CuSCN [15], np-TiO_2/$In(OH)_xS_y$/PbS/PEDOT:PSS [16], np-TiO_2/CdS/CuSCN [17] and ZnO-nr/In_2S_3/$CuInS_2$ [18] among others. Another concept is the depleted-heterojunction colloidal quantum dot solar cells [19].

In a solar cell, absorption of the incident illumination is followed by separation of electrons and holes, which are then transported in opposite directions to the external contacts. Copper containing materials have been used as hole conductors along with different electron conductors. Intermixing of Cu from the hole conductor or absorber layer at the interface results in the formation of interfacial layers with complex elemental compositions depending on the type of electron conductor or buffer layer, respectively. For example, in Cu_2S/CdS solar cells, heat treatment at 200°C to attain optimum performance [8] is usually accompanied by diffusion of Cu from the Cu_2S surface layer into CdS, which eventually degrades the solar cell by decreasing the fill factor and short circuit current density [20, 21]. Interfacial intermixing has been reported for other solar cell configurations at In_2S_3/CuSCN [22], $Cu(In,Ga)Se_2$/In_2S_3 [23], $Cu(In,Ga)Se_2$/CdS [24] and ZnS/Zn(S,O) [25] interfaces.

Figure 1.1 illustrates the major processes that take place across the interface of a solar cell with a Cu containing hole conductor. Examples of the electron conductors include CdS, In_2S_3, Zn(O,S), ZnS or Sb_2S_3 while hole conductors are CuSCN, CuI, $Cu(In,Ga)Se_2$ or $CuInS_2$. Transport of electrons and holes in their respective conductors away from the interface is accompanied by diffusion of Cu across the interface into the electron conductor. Electronic transport across the heterojunction depends on the band alignment, charge selectivity of the interface and electronic properties of the electron and hole conductors while Cu diffusion is enhanced during heat treatment.

Formation of efficient charge-selective contacts and enhanced electronic transport in most technologies require moderate post deposition heat treatment. On the other hand, diffusion of Cu across the interface results in an interfacial layer with a high density of Cu which modifies the band alignment and changes the electronic transport processes. Annealing the solar cells for a longer time and/or at higher temperature destroys the solar cells [23, 26, 22, 21, 20]. This means that there exists a critical amount of diffused Cu that is required to achieve optimal solar cell performance. For most of the solar cells the optimum annealing temperature is 200-230°C.

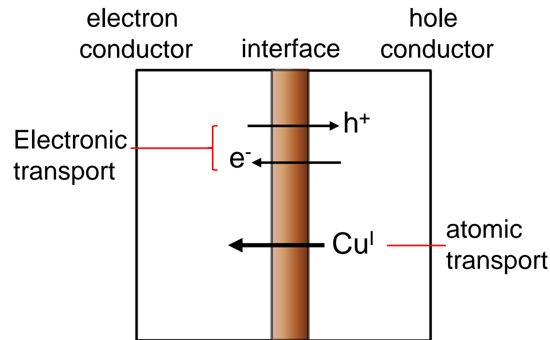

Figure 1.1: Electronic and atomic transport processes across an interface between an electron conductor and a Cu containing hole conductor. Electronic transport consists of transfer of photogenerated electrons and holes away from the interface in their respective conductors while atomic transport involves diffusion of Cu from the hole conductor into the electron conductor.

To determine by how much Cu diffusion contributes to the improvement and/or degradation of the solar cells utilizing Cu containing thin films, the exact amount of diffused Cu must be known. For example, Kranz and colleagues recently reported a conversion efficiency of 13.6 % for CdTe solar cells on a flexible metal foil with controlled doping of CdTe with Cu [27]. A thin Cu film less than a monolayer thick was deposited on top of CdTe and diffusion was performed at 400°C. As a result, the hole density increased, and the carrier life time and carrier collection in the solar cell were improved. The optimum density of Cu was obtained to be 6.5 - 8 x 10^{14} cm^{-3}. Such information on the optimal concentrations of Cu for other solar cell concepts is still unavailable in literature.

The band alignment at the heterointerfaces is crucial for the performance of solar cells and other optoelectronic devices. It should be adjusted such that photo-generated electrons are injected into the conduction band of the electron conductor and the holes into the valence band of the hole conductor [15]. The formation of charge selective contacts and the reduction of recombination are important because of the high density of electronic states available for both holes and electrons [11]. Therefore, material properties, suitable deposition methods and interface formation in semiconductor devices should be well understood to be able to improve their performance.

The formation of charge selective contacts requires knowledge of the electronic properties of the materials, charge separation and transport processes across the

interfaces. Charge transport and recombination across heterojunctions is limited by electronic defect states as well as by the band alignment. Surface or interface defects manifest as energetic states in the band gap of a semiconductor which act as recombination centers for charge carriers. An increase in the density of these defect states results in a higher recombination loss in the device. Atomic intermixing at the interfaces and the formation of interfacial layers can also change the band alignment and current transport properties.

Recombination of photo-generated charge carriers limits the conversion efficiency in solar cells. At low concentrations of excess charge carriers, Schockley-Read-Hall (SRH) recombination involving a single defect level in the band gap can dominate while Auger recombination can dominate at higher carrier concentrations [28]. Tunneling enhanced recombination across the interface can accompany SRH when there is high charge density in the space charge region (SCR). This can occur in the bulk or at the interface through trap states. Interface engineering and passivation of electronically active surfaces and/or interfaces is needed to be able to control recombination losses.

The results presented in this thesis were obtained after performing model experiments to investigate the formation of In_2S_3/CuSCN and np-TiO_2/In_2S_3 charge selective contacts for np-TiO_2/In_2S_3/CuSCN nanocomposite solar cells. This work focused on the diffusion of Cu from CuSCN into In_2S_3 layers deposited by thermal evaporation and ion layer gas reaction (ILGAR®) method. The other focus was on the formation of charge selective contacts investigated by monitoring charge separation across np-TiO_2/In_2S_3 and In_2S_3/CuSCN interfaces.

This thesis is divided into seven chapters where **chapter one** and **chapter seven** are the introduction and summary, respectively. **Chapter two** covers the fundamentals of diffusion in solids and electronic processes at disordered interfaces. Mechanisms of diffusion are presented and the Meyer-Neldel compensation rule is explained with regard to atomic diffusion. Electronic transport processes involving transport in bands, multiple trapping and hopping mechanisms in disordered semiconductors are then presented. This is followed by a review of heterojunction interface formation and charge transport processes across interfaces.

Chapter three presents the experimental methods used. This includes methods for sample preparation, measurements and analysis. The deposition methods for In_2S_3,

CuSCN and np-TiO_2 layers are first explained, followed by a description of the diffusion experiments and analysis of the data. Rutherford backscattering spectrometry (RBS) method for depth profiling is introduced including details of instrumentation and data analysis. A description of surface photovoltage (SPV) method for investigating charge separation is given and lastly structural and optical methods are presented.

Chapter four discusses the results of Cu diffusion from CuSCN source layers analyzed by depth profiling using RBS. A one dimensional diffusion model was applied to simulate and fit the depth profiles and obtain coefficients of Cu diffusion in In_2S_3 layers. Activation energies and diffusion prefactors of Cl-free and Cl-containing layers are compared. It is then shown that the relationship between the diffusion prefactors and activation energies of Cu diffusion can be described within the Meyer-Nedel compensation rule.

Chapter five contains the results from experiments on charge separation in thermally evaporated In_2S_3/CuSCN disordered heterojunction as a function of In_2S_3 layer thickness and annealing temperature. The results are correlated to current-voltage results for ZnO-nr/In_2S_3/CuSCN solar cells obtained from literature. As a conclusion, the optimal absorber thickness and annealing conditions that may enhance the conversion efficiency are obtained.

Chapter six covers results for interface formation and energy band alignment at np-TiO_2/In_2S_3 heterointerfaces investigated by spectral dependent SPV. Np-TiO_2 and In_2S_3 layers were deposited by screen printing and spray-ILGAR, respectively. A model for the band alignment at np-TiO_2/In_2S_3 interface developed using the work functions of Cl-free and Cl-containing In_2S_3 layers determined from ultra-violet photoelectron spectroscopy (UPS), their optical band gaps, and the shift in the onset of SPV absorption for np-TiO_2/In_2S_3 compared to bare In_2S_3 is presented at the end.

2. Diffusion and electronic processes at disordered interfaces

Properties of materials can be modified for various applications by introduction of foreign atoms. Foreign atoms can be introduced by annealing of a multilayer system, diffusion ion implantation or during preparation processes such as sputtering. The motion of the foreign atom inside the host material due to a gradient in chemical potential, concentration gradient or applied force field constitutes diffusion. On the other hand, the formation of disordered heterojunctions depends on the deposition parameters, chemical composition or stoichiometry, electronic properties and band alignment at the interfaces. This chapter starts with a background on extremely thin absorber and nanocomposite solar cells. This is followed by a description of atomic and ionic diffusion processes and of the Meyer-Neldel compensation rule. The formation of heterointerfaces and band alignments are then presented, highlighting the role of interface and bulk defects. The last section of chapter two covers charge transport and recombination processes across heterojunctions.

2.1. Extremely thin absorber and nanocomposite solar cells

A very thin absorber layer of the order of tens of nanometers is sandwiched between structured electron and hole conductors. The structuring of the electron conductor improves light absorption through multiple scattering and increases the effective thickness of the absorber. Nanoporous (np)-TiO_2 [13] and ZnO-nanorods [29] have been used as nanostructured electron conductors and CuSCN as the hole conductor for inorganic nanostructured solar cells. The absorber layer is locally thin but it is highly

folded when deposited on the structured substrate to increase the optical density and photon management. The band alignment should be optimized such that photo-generated electrons are injected into the conduction band of the electron conductor and the holes into the valence band of the hole conductor [15].

The open circuit voltage (V_{oc}) and short circuit current (I_{sc}) increased considerably after annealing ZnO-nr/In_2S_3/CuSCN [22] or np-TiO_2/In_2S_3/CuSCN [13] at 200°C for about 2 min thereby improving the conversion efficiency. This improvement was associated with the formation of In_2S_3/CuSCN charge selective contact. Annealing for longer times and/or higher temperatures led to the degradation of the solar cells due to enhanced diffusion of Cu into the In_2S_3 absorber. Slight intermixing of Cu with In_2S_3 at the In_2S_3/CuSCN interface created a thin In_2S_3:Cu interfacial layer with reduced band gap, which enhanced light absorption. Diffusion of Cu up to the ZnO/In_2S_3 interface was considered as the limiting factor for the solar cells and should be avoided to maintain high conversion efficiency [29]. Knowledge of the diffusion coefficients and activation energy of Cu in photovoltaic materials is important for controlling the heat treatment process and improving solar cell performance.

In_2S_3 layers exhibit varied properties depending on the deposition methods and conditions [30]. It has been shown that photo-excited electrons can be injected from In_2S_3 into np-TiO_2 [13]. The nature of semiconductor interfaces and hence band alignment depends very much on deposition processes and chemical composition of the layers. Charge transport and band alignment at np-TiO_2/In_2S_3 interface will therefore depend on the properties of In_2S_3 and hence the method of deposition. The choice of deposition method and parameters is therefore important.

Model experiments to investigate the formation of disordered In_2S_3/CuSCN and np-TiO_2/In_2S_3 heterojunctions and charge transport in these layer systems can provide information relevant for the improvement of solar cell performance. A study of Cu diffusion from CuSCN source layer into different In_2S_3 layers can provide information on diffusion coefficients and activation energies. Understanding band alignment at np-TiO_2/In_2S_3 interface can be investigated as a function of In_2S_3 layer properties by monitoring charge transfer and recombination mechanisms across interfaces.

2.2. Atom and ion diffusion in solids

Studying diffusion of atoms or ions in solids involves the investigation of their motion from one point to another in a host matrix. The diffusing foreign atom or ion is mostly referred to as a solute and the host matrix, which could be a metal or semiconductor crystal or thin film, is called the solvent. The combination of a foreign diffusing species and a host matrix then becomes a solid solution. In crystals, the position and motion of a solute atom is restricted to certain sites and paths, respectively. In amorphous solids, random motion of the solute atom is usually assumed due to the irregularity of the lattice sites and orientation.

The change in the concentration ($C(x,t)$) of the diffusing species with time can be described by Fick's second law of diffusion [31]

$$\frac{dC(x,t)}{dt} = D\frac{d^2C(x,t)}{dx^2} \tag{2.1}$$

where D is the diffusion constant. Solving equation 2.1 for a case with constant source concentration gives an error function describing the concentration profiles of the diffusing species

$$C(x,t) = C_0\left[1 - erf\left(\frac{x}{2\sqrt{Dt}}\right)\right] \tag{2.2}$$

where C_0 is the initial surface concentration at $x=0$ and t is the diffusion time. The value of D is usually obtained by fitting equation 2.2 to the measured concentration profiles. D is a function of temperature and obeys the Arrhenius plot of the form [31]

$$D(T) = D_0 exp\left(-\frac{E_A}{k_BT}\right) \tag{2.3}$$

where

$$D_0 = gfv_0a^2exp\left(\frac{\Delta S}{k_B}\right) \tag{2.4}$$

and g is the geometric factor, f the correlation factor, v_0 the attempt frequency approximated to be equal to the Debye frequency of the lattice (10^{13} Hz), a is the lattice parameters and ΔS is the change in the activation entropy. The values of g, f and a all depend on the type of lattice.

2.2.1. Diffusion mechanisms

Interstitial mechanism

When the solute atoms are relatively smaller than the solvent atoms, they are mostly accommodated in the host matrix by occupying interstitial sites. The interstitial solute atoms diffuse by moving from one interstitial site to a neighboring one as shown in figure 2.1 [31]. The solute moves from one equilibrium position to a saddle point, where maximum strain in the lattice occurs, and finally to another equilibrium position. No permanent distortion is caused in the lattice during this transition. This is also called direct interstitial mechanism.

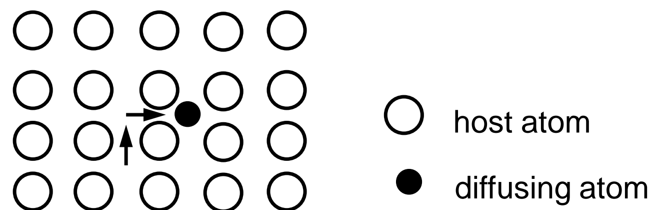

Figure 2.1: Interstitial diffusion mechanism. The diffusing atom (filled circle) moves from one interstitial position to another in host matrix (open circles).

Interstitial diffusion does not require defects to take place; therefore the diffusion coefficients are usually high. Small foreign atoms like C, N and O tend to diffuse in metals or other materials by this mechanism [31]. Large ions may also diffuse by interstitial mechanism if the anion sub-lattice contains empty sites in lines or planes that can serve as pathways for diffusion [32].

Vacancy mechanism

A vacancy refers to an unoccupied lattice site. A foreign atom diffuses by vacancy mechanism if it moves from a substitutional lattice site into a neighboring vacant site [32, 31] as illustrated in figure 2.2. The solute atom diffuses through the solid by making a series of exchanges with adjacent vacancies. The vacancy moves in the opposite direction. The vacancy mechanism is the dominant process for self-diffusion in substitutional alloys and in several ionic crystals and ceramic materials [31].

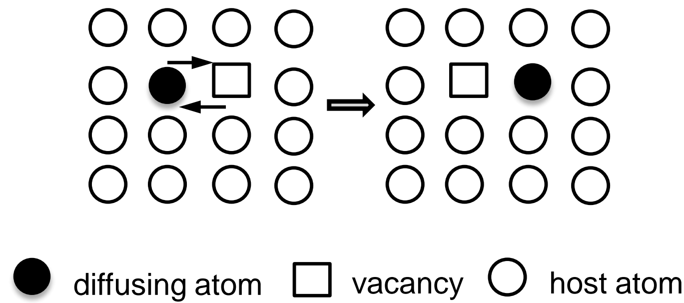

Figure 2.2: Vacancy diffusion mechanism. The diffusing atom (filled circle) moves to occupy a neighboring vacancy (open square) in the host matrix (open circles).

Interstitialcy mechanism

This mechanism is favored when the interstitial solute atom is almost of the same size as the solvent atoms [31]. A self-interstitial atom replaces a substitutional atom on a lattice site, which then replaces another solvent atom into interstitial position as it occupies the substitutional site as illustrated in figure 2.3. If the substitutional atom is displaced in the same direction as the interstitial atom, the process is termed collinear jump, and if it jumps in a different direction it is non-collinear jump.

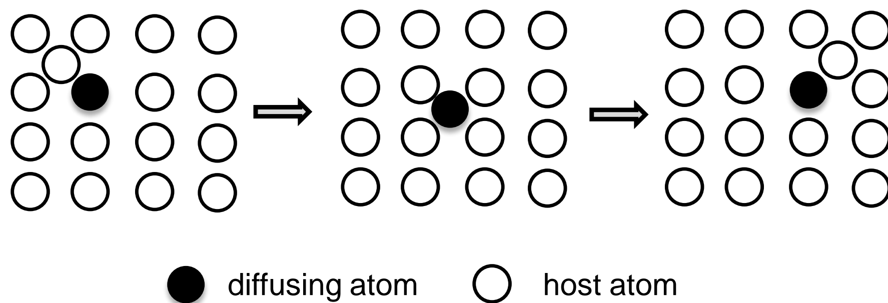

Figure 2.3: Interstitialcy diffusion mechanism. Self-interstitial atom (open circles) replaces a substitutional atom (filled circle), which then replaces a lattice host atom pushing it into self-interstitial.

The interstitialcy mechanism is not favored in metals because the formation of self-interstitials requires higher formation enthalpy compared to vacancies. The diffusion coefficient is proportional to the concentration of interstitial atoms or ions in the host matrix [32]. The interstitialcy and vacancy mechanisms are important for self-diffusion for example in Si and some silver halides.

Dissociative and kick-out mechanisms

Some solute atoms may occupy interstitial (*I*) and substitution (*S*) sites of the solvent matrix (A) which is therefore referred to as a hybrid solute [31]. The diffusion coefficient of hybrid solutes in interstitial configuration is usually higher than that in the substitutional configuration. On the other hand, the solubility limit for the interstitial arrangement is lower than for substitutional arrangement. This could lead to a fast diffusion of *I* and then *S* in an interstitial-substitutional exchange process.

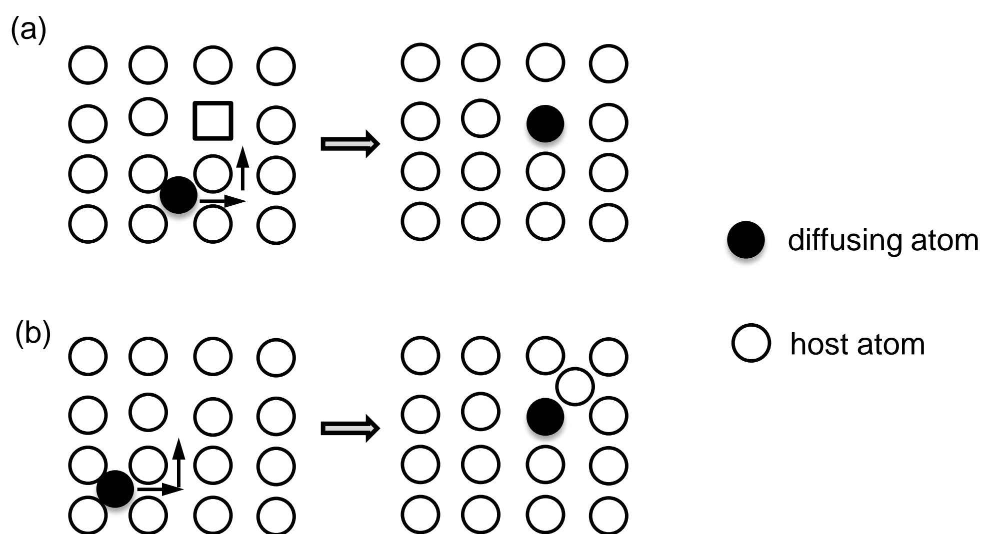

Figure 2.4: Interstitial-substitutional exchange diffusion mechanism. Foreign interstitial atom (filled circle) occupies a vacancy (Open Square) in dissociative mechanism (a) or replaces a lattice atom (open circles) in kick-out mechanism (b).

When the exchange involves a vacancy (*V*), the mechanism is referred to as dissociative or Frank-Turnbull mechanism as shown in figure 2.4 (a). It can be illustrated as $I \rightleftharpoons V = S$. This mechanism was first proposed for fast diffusion of Cu in Germanium [33]. Diffusion of metallic solute atoms in polyvalent metals like Pb, Ti and Zr is dominated by the dissociative mechanism [31]. When the exchange involves self-interstitial atoms (AI), the mechanism is termed kick-out mechanism as illustrated in figure 2.4 (b). It can be illustrated as $AI \rightleftharpoons S + I$. This mechanism was first proposed for diffusion of Au, Pt and Zn in Si [31].

2.2.2. Cu diffusion in solar cells

Cu is known to be a fast diffuser in many materials. This fast diffusion is because it occupies interstitial positions and migrates as a singly ionized interstitial Cu with positive charge [34]. The velocity of diffusion depends on the geometry of the host matrix as well as on the relative concentration of interstitial and substitutional Cu. Substitutional Cu is relatively immobile because a vacancy is required for a transition from interstitial to substitutional position. The fast diffusion of Cu in semiconductors strongly affects performance of devices.

It has been shown from experiments and theoretical calculations that Cu diffuses by different mechanisms in semiconductors. Copper diffuses as an interstitial in Si with activation energy of 0.18 eV, which is the lowest for atomic diffusion in Si [35]. In amorphous Ge, Cu diffuses by interstitial mechanism with activation energy of 0.5 eV in the temperature range of 20 to 200 °C [36]. Copper diffuses in CdS in the temperature range 146-400°C by interstitial mechanism before occupying a Cd vacancy as in dissociative mechanism [37]. Diffusion of Cu in SiO_2 takes place by interstitial mechanism with an activation energy of 1.82 eV in the temperature range of 350-450 °C [38]. The activation energy for Cu diffusion in CdTe between 97 and 300 °C temperature is 0.67 eV. Cu diffuses by interstitial-substitutional mechanism. Cu diffusion in In_2S_3 in the temperature range 150-250 °C proceeds with an activation energy of 0.3 eV [39]. Diffusion in crystalline In_2S_3 is dominated by vacancy and insertion-substitutional mechanisms [40, 41].

Control of Cu diffusion in electronic and optoelectronic devices has been investigated for several decades but still remains a challenge today. Cu leads to an increase in leakage currents at p-n junctions and creates minority carrier recombination centers in Si solar cells [35]. In thin film solar cells, the excess diffusion of Cu from $Cu(In,Ga)(S,Se)_2$ (CIGS) absorber into CdS or In_2S_3 buffer layers during preparation or post-deposition heat treatment leads to a deterioration of the conversion efficiency [23, 26, 42]. Investigation of the CIGS/In_2S_3 interface showed a strong intermixing and the formation of an interfacial layer with high Cu concentration. This leads to Cu depletion on the CIGS side and to a compositionally graded interface [42]. Annealing the solar cells at 300°C leads to the formation of $CuIn_5S_8$ interfacial layer and to complete degradation of the solar cells.

CdS/CdTe solar cells made with Cu-containing back contact experience enhanced performance with minimal Cu diffusion but deteriorate afterwards due to increased diffusion [43, 44]. Cu forms mid gap defects that act as recombination centers and lower charge carrier life time, open circuit voltage and fill factor. The conversion efficiency deteriorates with increasing Cu diffusion.

Heat treatment of the Cu_2S/CdS heterojunction solar cells decreases the short circuit current density and the fill factor while the diffusion length of Cu diffusion increases [20]. It has been shown that an insulating layer of CdS is formed at the Cu_2S/CdS junction as Cu diffuses from Cu_2S into CdS during moderate heat treatment at 200°C that is needed for optimum performance [45]. At elevated temperatures above 100°C, a CdS photovoltaic cell shows steady loss of current output and fill factor and an increase if series resistance. The increase in series resistance was associated with diffusion of Cu from Cu_2S surface layer into CdS, which increases the width of the insulating CdS interface layer.

Nanostructured solar cells having Cu containing hole conductors suffer from stability problems due to uncontrolled Cu diffusion from the hole conductor into the absorber with post-deposition annealing and/or longer storage times [29, 13, 46, 22]. For example, the efficiency increased strongly after annealing a complete ZnO/In_2S_3/CuSCN solar cell for about 2 min at temperature of 200°C but degraded after annealing for longer times and/or at higher temperature. This was due to diffusion and intermixing of Cu and In_2S_3 at the interface with CuSCN hole conductor [22, 47].

2.2.3. Cu in In_2S_3

In_2S_3 crystallizes in three phases namely α, β and γ phases. The γ-In_2S_3 phase is stable at temperatures above 754°C, α-In_2S_3 is stable at temperatures between 420 and 754°C while β-In_2S_3 is stable at temperatures below 420°C [48]. The transitions at 420 and 754°C are reversible and are only possible for stoichiometric crystals. β-In_2S_3 is stable at room temperature and has a structure based on a cationic-deficient spinel superstructure containing 16 molecules of In_2S_3 [49]. Indium atoms occupy all octahedral sites and 2/3 of the tetrahedral metal sites. 1/3 of the metal positions remain vacant, which amounts to 4 cationic vacancies per unit cell, and are ordered into a 4_I

screw by alignment of three spinel blocks in c-direction [48]. A unit cell for an In_2S_3 crystal is shown in figure 2.5.

The defective structure of In_2S_3 allows it to accommodate different foreign atoms. Cu diffuses in In_2S_3 by vacancy [40] or insertion and substitution mechanism [41]. When Cu is introduced into In_2S_3, 2/3 of the atoms fill up the cationic vacancies and 1/3 substitutes for In to maintain electro-neutrality. First principle calculations have shown that Cu-3d states contribute to the formation of the valence band maximum (VBM) resulting in a shift of VBM to higher binding energy with increasing Cu amounts [41]. This explains experimental results showing a decrease in the optical band gap with increasing Cu content [50]. When Cu is introduced into In_2S_3, the lattice parameter (a) and electron conductivity drops with increasing Cu content, although In_2S_3:Cu maintains n-type conductivity [51].

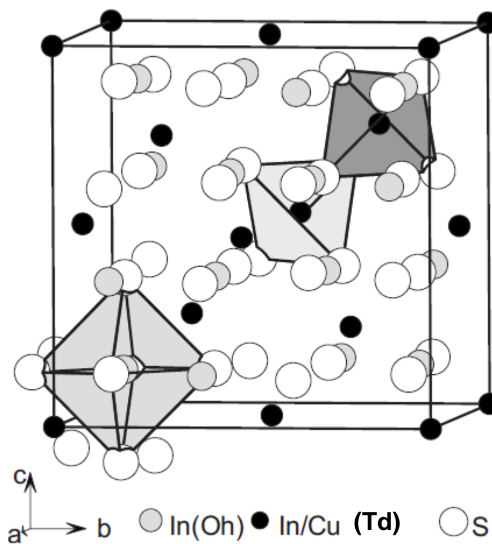

Figure 2.5: Unit cell for In_2S_3. In and Cu atoms (filled black circles) are statistically distributed on the tetrahedral sites, while In (gray circles) fills the octahedral sites [41]. The open circles denotes S atoms.

2.2.4. Meyer-Neldel rule for atom diffusion

The Meyer-Neldel (compensation) rule (MNR) describes groups of related thermally activated processes that obey the Arrhenius plot

$$X(T) = X_0 exp\left(-\frac{E_A}{k_B T}\right), \qquad (2.5)$$

where X represents the rate of the activated process, X_0 is the pre-exponential factor, E_A is the activation energy and k_B is the Boltzmann constant. When the activation energy within a group of processes is varied, the value of X_0 follows the exponential relation,

$$X_0 = X_{00} exp\left(\frac{E_A}{E_{MN}}\right) \qquad (2.6)$$

where E_{MN} is the Meyer-Neldel energy and X_{00} is a proportionality constant. The increase in X_0 when E_A is increased according to equation 2.6, compensates for the decrease in the activation factor in equation 2.5 so that the process takes place at a larger rate than would be expected if only E_A was known [52].

The value of $E_{MN} = k_B T_0$ is proportional to the characteristic energy of the heat bath or reservoir [53] that supplies the energy needed for the transition to the activated state. It is of the order of the energy of the excitations in the reservoir. Some authors have considered T_0 as a characteristic temperature at which the different Arrhenius plots of the samples with different activation energies converge [54, 55, 56]. Others have associated the value of T_0 with the average of the experimental temperature range [54, 56, 57]. For example, the iso-kinetic temperature T_0 for self-diffusion in Ge was reported as 1175 K (E_{MN} = 101 meV) within the experimental range of 973 – 1203 K, while for self-diffusion in Si the value of T_0 was 1575 K (E_{MN} = 136 meV) within the range of 1130 – 1673 K [54]. Similar analyses are given by Kirchheim and Huang and they show a deviation of between 10 and 20 % between T_0 and average temperature of the experimental range [56].

The exact origin of the mechanisms leading to the MNR is still under discussion although the explanation of Yelon and Movaghar (YM model) involving multi-excitation processes has received relatively wider acceptance [53, 58, 59]. The YM model is considered to hold for most cases. Other explanations of the origin of MNR are specific to the material or phenomenon in question. The statistical shift model, which describes MNR as a consequence of the change in the Fermi level with temperature was found to hold for DC conductivity in hydrogenated amorphous silicon (a-Si:H) [60]. A model based on the one-phonon activated process with a distribution of densities of the

initial and final states was also proposed to explain the origin of the MNR for defect relaxation in a-Si:H [61].

The YM model emphasizes that a multi-excitation process, for example multi-phonon excitations, is the origin of the MN behavior [59]. MNR arises for the kinetic process of which E_A is larger than the energies of excitation that contribute to the activation as well as k_BT. When E_A is large, the number of different paths to the final state via multiphonon processes increases exponentially with E_A, according to equation 2.6. Generally, the MNR is obtained by counting the number of ways in which the heat bath can furnish the energy required to surmount an activation barrier.

The exponential in equation 2.6 arises from the entropy of combining multiple excitations in the thermal reservoir available for the kinetic processes. The existence of MNR arise from the fact that energy is extracted from a particular reservoir. This is why different phenomena for the same material should show the same MN slope and hence the same E_{NM}. Diffusing species in the same matrix or the same diffusing species at different concentrations or in matrices of different defect structures should satisfy the MNR with about the same value of E_{MN} [56, 53]. This denotes that the source of energy and mechanisms of transfer are the same for all such processes. This is because the excitations causing the activated diffusion processes come from the same reservoir, which contains the excitations of the lattice (phonons).

2.3. Electronic transport in disordered semiconductors

Electrons in a disordered semiconductor see a random background potential different from the periodic potential of a perfect crystal. They find potential wells where they are localized forming band related tail states [62]. The width of the band tails is related to the degree of disorder in the semiconductor. Most of the charge carriers injected into a material with broad distribution of localized states become localized [63]. Electronic transport in disordered semiconductors take place via three main processes as shown in figure 2.6 namely, band conduction (a), trapping detrapping (b) and hopping mechanisms (c).

2.3.1. Electronic transport in the conduction band

In a broader temperature range, the direct current (DC) conductivity in disordered materials is given by [64]

$$\sigma = \sigma_0 \cdot exp\left[-\left(\frac{\Delta}{k_B T}\right)^{\beta}\right] \tag{2.7}$$

where the pre-exponential factor σ_0 depends on the system, the power exponent β depends on the material and temperature range, Δ is the activation energy, T is temperature in Kelvin scale and k_B is the Boltzmann constant. In many disordered inorganic materials, σ_0 is of the order of $10^2 - 10^4\ \Omega^{-1}cm^{-1}$. The value of β is close to unity for temperatures close to or higher than room temperature, but it is less than unity for lower temperatures. The electrons in states within the range of width of order $k_B T$ above the mobility edge dominates band conduction [64].

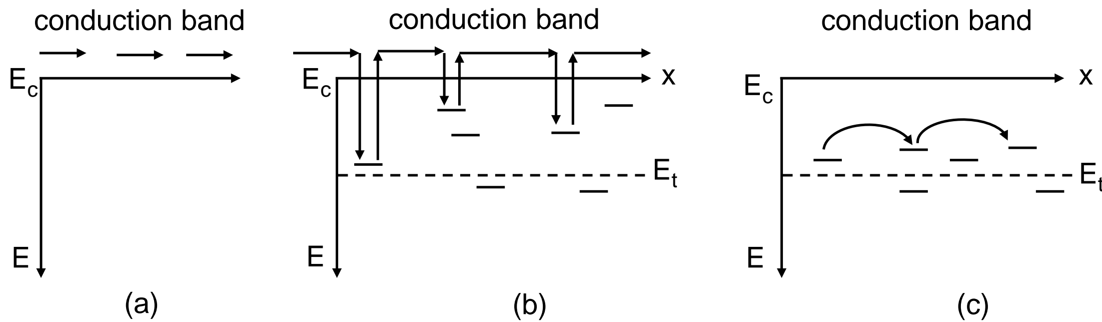

Figure 2.6: Electronic transport processes in disordered semiconductors consisting of normal band conduction (a), trapping and detrapping (b) and hopping (c) mechanisms.

Band conduction, shown in figure 2.6 (a), is only significant at high temperatures or when the materials have a very low density of localized states at the mobility edge. At high temperatures, a fraction of electrons can be found in the delocalized states above the mobility edge and they dominate conductivity in the disordered system [64]. Transport in this case is similar to that in ordered crystalline semiconductors. At lower temperatures, transitions of carriers between localized and extended states occur in the multiple trapping mechanisms, while in the hopping transport the transitions are from localized to localized states as shown in figure 2.6 (b) and (c), respectively.

2.3.2. The multiple trapping transport model

A charge carrier can be thermally activated from a defect state below the mobility edge into the delocalized states where it is free to move by conduction band transport. After a while the carrier gets trapped again and become immobile as shown in figure 2.6 (b). The multiple trapping (MT) model states that, the decaying carrier mobility is a consequence of charge carriers being trapped below the band edges where they remain immobile until they are again re-emitted into the bands [65]. The traps could be deep traps located near the center of the band gap or shallow traps located close to the valence and/or conduction band edges. The emission rate v_i of a carrier from a single trap state i of energy E_t, where v_0 is the attempt to escape rate usually assumed to be equal to the frequency of phonons of the order 10^{12} - 10^{13} s^{-1}, k_B the Boltzmann constant and T the temperature, is given by the expression [66],

$$v_i = v_0 exp\left(-\frac{E_t}{k_B T}\right). \quad (2.8)$$

The trap energies can be distributed exponentially,

$$g(E) = \frac{N_t}{k_B T_0} exp\left(\frac{E}{k_B T_1}\right) \quad (2.9)$$

where N_t is the total trap density and T_1 is the distribution parameter in temperature units. The product $k_B T_1$ gives the slope of the exponential tail state distribution. The main features of MT model are the trapping times, carrier reemission for intermediate times and carrier recombination which occurs at longer times.

If we consider an energy distribution of electrons in the extended states above the conduction band (E_c) generated by a short laser pulse, the states below E_c will at first be uniformly populated. The distribution of the carriers after the first trapping events will be determined by the density of states in the band tail [64]. Charge carriers in shallow states will be released into extended states above E_c with time, while the trapping process remains random. This leads to a redistribution of trapped carriers from shallow states into deeper energy states in the band tail. The demarcation energy $E_D(t)$ separates those states whose occupation remains uniform from those in quasi thermal equilibrium and it corresponds to the energy at which the trap release time $\tau(E)$ is of the order of the delay time after the laser pulse, t [67]. The value of $\tau(E)$ is given as the inverse of the

emission rate in equation 2.8. The demarcation energy $E_D(t)$ is obtained by setting the condition $\tau(E_D) = t$ giving

$$E_D(t) = k_B T ln(v_0 t) \tag{2.10}$$

2.3.3. The hopping transport model

At lower temperatures, only few electrons occupy extended states while many electrons are in localized states below the conduction band edge. Hopping electron transitions between localized states dominates charge transport in disordered systems [64]. Hopping transport dominates conductivity when there is a large density of defect states at the Fermi level as shown in figure 2.6 (c). Hopping can also take place in the band tails where the density of states is very large but the carrier concentration is low. The distribution of waiting times is determined by the distribution of distances r_{ij} between two sites i and j. The probability of a carrier to hop from one localized state i at energy E_i to another localized state j at energy E_j, with spatial separation r_{ij} between them is given by the Miller-Abraham's relation [68, 69],

$$v_{ij} = v_0 exp\left(-\frac{2r_{ij}}{\alpha}\right) exp\left(-\frac{E_j - E_i}{k_B T}\right); \quad E_j > E_i \tag{2.11}$$

$$v_{ij} = v_0 exp\left(-\frac{2r_{ij}}{\alpha}\right); \quad E_j < E_i \tag{2.12}$$

where α is the localization length and determines the exponential decay of the electron wave function in the localized states and v_0 is the attempt to jump frequency and is on the order of $10^{-12}\ to\ 10^{-13}\ s^{-1}$. v_0 depends on the electron interaction mechanisms that cause the transitions. The hopping transition of a carrier from site i to j of energies E_i and E_j, respectively is illustrated in figure 2.7.

If the localization if strong, where $r_0/\alpha \gg 1$, an electron will jump to the nearest neighboring state. The hopping distance is limited to the nearest neighbor hopping sites by an average distance r_0. This is called the nearest neighbor or Miller-Abrahams hopping [68]. If $r_0/\alpha \leq 1$ or the temperature is sufficiently low, then the second term on the right hand side of equation 2.11 contributes significantly to the hopping probability. The carriers then hop preferentially to sites more far away in space but

closer in energy. This constitutes the variable-range hopping introduced by Mott and Davis [70, 71].

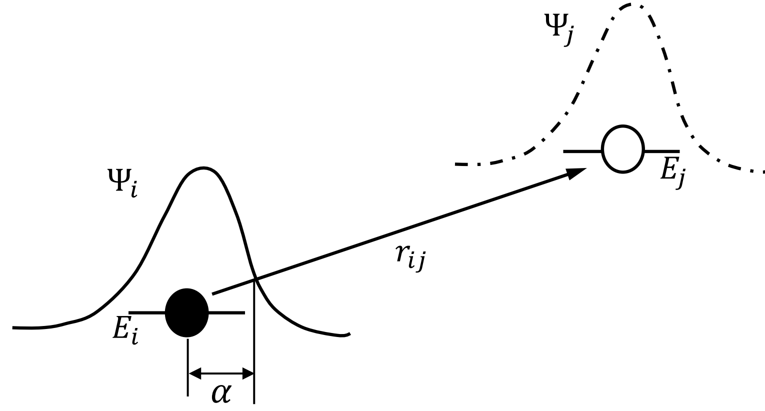

Figure 2.7: Hopping transition from a localized occupied state *i* to an unoccupied state *j* with energies E_i and E_j, respectively. Ψ_i and Ψ_j are the wave functions of the electron when at site *i* or *j*, respectively.

In the case of nearest neighbor hopping, electrons hop preferentially to spatially nearest sites. This hopping takes place at high enough temperatures when the thermal energy $k_B T$ is larger than the energy scale of the DOS. The hopping rates of an electron from site *i* to site *j* are determined by spatial terms only given by equation 2.12. If the temperature is not high and the thermal energy is comparable to or smaller than the energy spread of the localized states involved in charge transport, then both the energy and spatial dependent terms of the hopping rates become important [64]. The lower the temperature the more significant the energy-dependent terms in equation 2.11 become. If the spatially nearest neighbor has a relatively higher energy, the electron will prefer to hop to a distant site that has energy closer to the initial one. Therefore, the length of electron transitions increases with decreasing temperature.

According to Mott [71], filled and empty states near the Fermi level have almost similar energies, therefore efficient transport transitions of electrons occur close to the Fermi level. At low temperatures, the density of states near the Fermi level has a parabolic shape and vanishes exactly at the Fermi energy. The temperature dependence of conductivity for variable range hopping mechanism takes the form $ln\sigma \sim T^{-\frac{1}{4}}$ [71]. The jumping rate is given by the expression

$$v_{ij} = v_0 exp\left(-\frac{A}{k_B T^{1/4}}\right) \tag{2.13}$$

2.3.4. Trap-limited transport in nanocomposites

In nanocomposite solar cells, materials with different electronic properties are interpenetrated to enhance local charge separation with separate transport paths for electrons and for holes. The transport of photogenerated electrons through the network of interconnected nanoparticles is crucial for the performance of these devices [72]. The electrons, from a sensitizer that absorbs light, are injected into the nanoporous network and they travel in the network until they recombine or are collected at the external electrodes [73]. It has been shown from theoretical [74] and experimental [75] analysis that electronic transport in nanoporous TiO_2 is controlled by trapping and detrapping processes in a large density of band gap states distributed in energy at the TiO_2/sensitizer interface [72, 75]. The photogenerated electrons drift through the particulate TiO_2 towards the internal interface due to a gradient in the Fermi level. During the motion some electrons can be lost through recombination or trapping in states from which they can be reemitted thermally [75].

Electron transport in porous and nanocrystalline metal oxides exhibits a strong nonlinear dependence on the electron density and electron injection, which is usually explained in terms of the trap filling effect [73]. As more electrons are injected into a system with a distribution of trap states, the deep traps are progressively filled leaving only shallow traps for conduction. The resident times of the electrons trapped in deep traps is much longer than for the electrons in shallow traps, therefore the mobility of the electrons is enhanced as the electron density is increased. The population of trap states also enhances recombination with increasing electron density. This is observed as a faster decay of transient current or voltages as the electron density increases [74].

Electronic transport in the np-TiO_2/sensitizer nanocomposites exhibit anomalous properties with extremely slow, non-exponential current and charge recombination transients and intensity dependent response times [74]. This behavior is attributed to the high density of intra-band trap states in np-TiO_2.

Photovoltage (PV) experiments on np-TiO_2 showed retarded transients characteristic of diffusion transport with a linear dependence of the PV amplitude on laser intensity [76]. Trapping of charge carriers in electronic states in the forbidden gap is the reason for the retardation of the PV transients. Surface states on np-TiO_2 are due to oxygen vacancies

and they depend on the ambient conditions [76]. The size of the TiO_2 nanoparticles and porosity is also crucial for charge transport in np-TiO_2.

2.4. Interface formation

2.4.1. Semiconductor heterojunctions

When two different semiconductors are brought into tight contact they form a heterojunction. The properties of the interface at the heterojunction will be different from those of the free surfaces of the individual semiconductors. Because of the abrupt change in the crystal structure, periodicity of the lattice and the resultant disorder near the interface, the material properties at the interface are different from the bulk [77]. When the transition region from one material to the next one is very thin, the heterojunction is said to be abrupt.

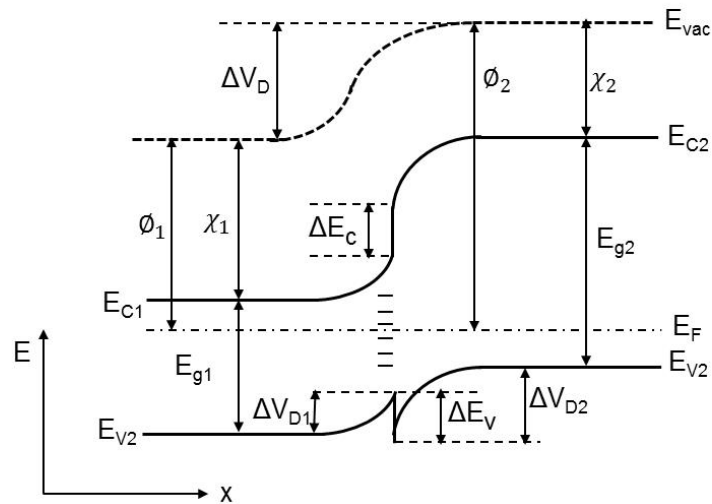

Figure 2.8: Energy band alignment at a heterojunction in equilibrium. Two materials of band gaps E_{g1} and E_{g2}, work functions $\emptyset_1$ and $\emptyset_2$, and electron affinities χ_1 and χ_1 are brought into contact to form a heterojunction with conduction and valence band offsets ΔE_c and ΔE_v, respectively. E_{vac} is the vacuum level, E_{c1}, E_{v1} and E_{c2}, E_{v2} are the conduction and valence band edges for small band gap (1) and large band gap (2) semiconductors, respectively. $\Delta V_{D1} + \Delta V_{D2} = \Delta V_D$ is the sum of the partial built-in voltages and E_F is the Fermi level. After [78].

The energy band alignment across the interface is the most important property of the heterojunction. It determines the conduction and valence band discontinuities and hence the barriers for electrons or holes across the interface. The interface dipole can alter the band alignment at the heterojunction and change the electronic properties of the entire system [79]. Interchange of atoms or interdiffusion at the interface introduces electronic and atomic dipole moments that change the band discontinuities and transport properties.

Figure 2.8 shows the energy band alignment of two semiconductors, one with a small band gap (E_{g1}) and a second with a larger band gap (E_{g2}). The two semiconductors have different work functions ϕ, electron affinities χ and dielectric functions ϵ. The differences in energy of the conduction and valence band edges are the conduction (ΔE_c) and valence band offsets (ΔE_v), respectively. The difference in the work functions of the two semiconductors is the total built-in voltage in the heterojunction. Because of the difference in the dielectric constants, the electrostatic field is discontinuous at the interface [78].

An additional dipole at the interface adjusts the potential difference across the heterojunction. A very thin barrier is transparent to charge carriers and can reduce the barrier height. The dipole layer can be a result of surface states at the interface – a density of 10^{12} - 10^{13} cm^{-3} is sufficient to modify the barrier height [80]. There might be a dielectric layer at the interface due to surface oxidation. The different dielectric constant of the surface layer causes a polarization layer at the interface. The dipole layer could be a result of a configuration of polar molecules at the surface [80].

Semiconductor heterojunctions can be classified as (i) straddled or type I heterojunction, (ii) staggered or type II heterojunction and (iii) broken-gap or Type III heterojunction. In the straddling or type I heterojunction, the conduction band of the first semiconductor lies lower but the valence band is higher than the conduction band and valence band of the second semiconductor, respectively. For staggered or Type II heterojunction, both conduction and valence bands of the first semiconductor are lower than the conduction and valence bands of the second semiconductor, respectively, such that electrons are collected at the lower conduction band in the first semiconductor and holes at the higher valence band in the second semiconductor. The broken-gap or Type III heterojunction in which both conduction and valence bands of the first

semiconductor are lower than the valence band of the second semiconductor is rare [81]. Several theories have been developed to determine band alignments at semiconductor heterojunctions.

Electron affinity rule

The electron affinity rule was proposed by Anderson [78] based on the Ge-GaAs heterojunction and it states that, the conduction band offset is the difference between the electron affinities of the two semiconductors. The valence band offset is then given by the difference in the ionization energy between the two semiconductors.

$$\Delta E_c = \chi_2 - \chi_1 = \Delta\chi \quad (2.14)$$

$$\Delta E_v = I_2 - I_1 = \Delta I \quad (2.15)$$

where χ_1 and χ_2 are the electron affinities and I_1 and I_2 ionization potentials of SC_1 and SC_2, respectively. The dependence of the electron affinity on surface termination and orientation is the main weakness of the electron affinity rule for determination of band offsets.

Common anion rule

The common anion rule states that the valence band discontinuity at the interface will be very small for semiconductors with the same anion. When the anion atom species for the two semiconductors forming a heterostructure is the same, for example (Al,Ga)As/GaAs, the valence band offsets will be much smaller than the conduction band offset [82]. This proceeds from the fact that valence band wave functions are derived mainly from the anion atomic wave functions and tend to be more localized than conduction band wave functions [79]. Density functional theory (DFT) calculations by Wei and Zunger, which included interface dipoles, revealed a deviation from the common anion rule band alignment for the III-V semiconductors [83, 84]. This was due to stronger interfacial dipoles from induced gap states. Calculations for II-VI semiconductors were in agreement with the common anion rule.

Tersoff's effective dipole model

Tersoff proposed a model for determining band offsets similar to Anderson's electron affinity model but which takes into account the influence of interface dipoles [85].

Dipole charges at the heterointerface associated with gap states induced by the band discontinuities tend to drive the band alignment towards that value which will give a zero dipole [85]. There exists some effective energy E_B such that states higher or lower in the gap have more conduction or valence character, respectively. The gap states at this energy are non-bonding in character and E_B plays a role similar to the Fermi level in metals. Any discontinuity in E_B at the interface amounts to a discontinuity in the electronegativity, which gives rise to a charge-transfer dipole [86]. Obtaining the zero-dipole line-up requires, therefore, aligning E_B of the respective semiconductors.

2.4.2. Charge transport at heterojunction interfaces

A heterojunction has an electrostatic field at the interface to draw photo-generated charge carriers away from and/or past the recombination centers in the space charge region and at the interface. Charge carriers can attain high enough energy to jump, by thermal emission and diffusion, over the barrier to the other side of the interface [87]. Traps usually exist in semiconductors and empty traps in the depletion region can affect transport at the interface by acting as active recombination sites for electrons and holes. The different transport mechanisms at the interface are illustrated in figure 2.9.

Thermionic emission is the excitation of charge carriers over the top of the barrier at the interface [80] as shown by process *a* in figure 2.9. A carrier is transferred from an allowed state in one material into allowed states in the second material with no change in the total energy. Direct tunneling through the barrier is shown by process *b*. This process depends on the barrier height and the extension of the barrier region. It is significant when the internal field is large, and this occurs when the applied voltage is high or the depletion region is narrow [80]. Tunneling becomes more dominant for heavily doped semiconductors and/or for operation at low temperature [81].

Thermally enhanced field emission is shown in figure 2.9 by process *c*. This process dominates for high doping levels where the space charge region becomes narrow [88]. Field emission is a pure tunneling process that occurs near the Fermi level, while thermally enhanced field emission is tunneling of thermally excited carriers at energies between thermionic emission and the Fermi level. Multistep or indirect tunneling (*d*) involves tunneling from one defect to another in the barrier region. It can involve

phonons and occur for a range of barrier thicknesses and doping levels. An electron in the conduction band can also be trapped by a localized state at or near the interface and be emitted later. This depends on the population of the carriers and the capture cross-section.

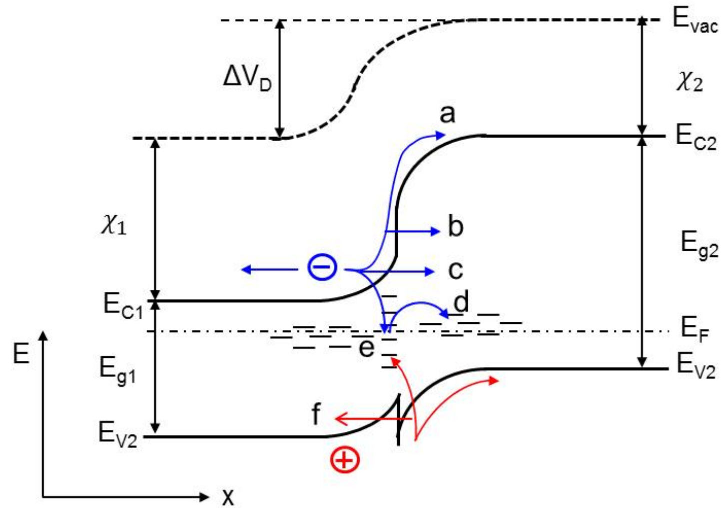

Figure 2.9: Mechanisms of electronic transport across a heterojunction interface. Charge carrier transport across the interface can proceed by thermionic emission (a), tunneling through the barrier (b), thermally enhanced field emission (c), multiple (indirect) tunneling (d), interface recombination (e) and minority carrier injection (f).

Trap-assisted interface recombination is denoted by *e* in figure 2.9. An electron from the conduction band is trapped in an interface trap where it recombines with a hole from the valence band. Interface recombination is determined by the density of interface states at the boundary [77]. Combination of different materials, for example in thin film solar cells, leads to a high interface density of states, and hence high recombination velocities. Minority carriers can be injected into gap states in the small band gap material by process *f*. The minority carrier diffusion current is much smaller than the majority-carrier thermionic emission current [81]. At sufficiently high forward bias, the drift component of minority current increases and therefore it enhances the overall injection efficiency.

2.4.3. Interface states and Fermi level pinning

At the surface of a semiconductor, the periodicity of the crystal lattice and symmetry are destroyed. Electrons on the surface are held by almost half of their bonds and are at higher energies compared with those in the bulk of the crystal. They induce energetic levels close to the mid band gap and are referred to as surface states or traps, which are also deep defects in the band gap [89, 90]. Deep defects act as recombination centers for minority and majority charge carriers, which lowers the carrier life time. Charge carriers can also be trapped and released when the applied voltage changes [91].

Interface states, for example, result from a lattice mismatch between two semiconductors, different morphological phases and chemical compositions [92]. Disordered interfaces contain localized states extending the whole range of the interface. The density of interface states plays an important role in limiting the efficiency of current transport in the heterojunction. The presence of interfacial density of states denotes disorder and atomic intermixing at the heterojunction. Atomic intermixing at the interface could be responsible for the variation of energy band offsets and density of states with growth conditions.

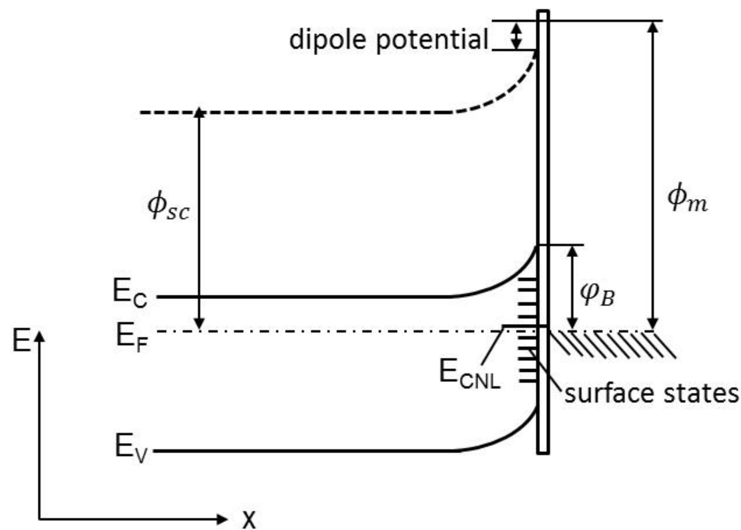

Figure 2.10: Potential and charge distribution at n-type semiconductor/metal interface. $\emptyset_{sc}$, E_F, E_c and E_v are the work function, Fermi level, conduction and valence band edges, respectively, for the semiconductor. E_{CNL}, φ_B and $\emptyset_m$ are the charge neutrality level, barrier height and the metal's work function.

The energy alignment for an n-type semiconductor/metal interface is given in figure 2.10. The barrier height φ_B for electrons (holes) is the difference between the Fermi level and the conduction (valence) band edge. The surface states are distributed continuously in energy within the energy gap. They are characterized by a charge neutrality level (E_{CNL}) such that states above E_{CNL} are neutral when empty and negatively charged when occupied (acceptor-like states) and the states below E_{CNL} are neutral when occupied by electrons and positively charged when empty (donor like states). There is no charge at the interface if $E_F = E_{CNL}$. A negative (positive) charge will occur if $E_F >(<) E_{CNL}$. The position of E_{CNL} is determined by the distribution of the surface states [88].

The Fermi level lies between the highest filled and lowest empty energy states. The states can be donor or acceptor like depending on their energy position relative to the Fermi level. The density of surface states can be large enough to cause Fermi level pinning where the states determine the position of the Fermi level. An electric field is established in the semiconductor normal to the surface causing downward or upward surface band bending for p-type or n-type semiconductor, respectively [89]. Fermi level pinning results in barriers heights being almost independent of the contact metal. Fermi level pinning is more pronounced in semiconductors with covalent bonding like Si, Ge and less pronounced for polar bonded materials like metal oxides.

Bulk defects comprise of point, line and volume defects in the semiconductor. Point defects can be intrinsic (vacancies, interstitials and antisites) or extrinsic (impurities) and can change the bonding and distribution of electronic states with energy and momentum. Line defects like dislocations disrupt the lattice periodicity and may contain dangling bonds with associated energetic states in the band gap [91]. They decrease the carrier mobility by increasing scattering sites. These defects create bands of surface states and a large density of defect states at the interface which can act as traps for minority carriers and/or recombination centers. An interface in a heterostructure develops a contact potential that produces an electric field. The electric field can enhance trapping of one or both types of charge carriers [91].

The rate of charge carrier recombination at the surface is known as the surface recombination velocity (S_t) and it depends on thermal velocity (v), capture cross-section (σ_t) and the density of surface states (N_t) [93] as

$$S_t = v\sigma_t N_t \tag{2.16}$$

Large values of S_t denote high recombination rate and hence lower carrier life time. The minority charge carriers are characterized by a diffusion length,

$$L_{min} = \sqrt{\pi D \tau_{eff}}, \tag{2.17}$$

where D is the carrier diffusion coefficient and τ_{eff} the effective minority carrier life time, which is inversely proportional to S_t. The diffusion length is the distance a photo-generated minority carrier can travel in a field-free region before recombining [93]. Trap-assisted recombination reduces the carrier lifetime and hence it limits the performance of optoelectronic devices [89]. Surface recombination can be reduced by deposition of a passivation layer on top of the semiconductor.

3. Experimental methods

In this chapter, the methods employed in the preparation of samples and analyses are presented. Methods used to deposit In_2S_3 and CuSCN layers are described followed by a discussion of the different substrates onto which these layers were deposited. The second part of this chapter introduces Rutherford backscattering spectrometry (RBS) used for compositional analysis and depth profiling in diffusion experiments. Surface photovoltage (SPV) technique is then described and lastly methods for investigating the structural and optical properties of In_2S_3 layers are presented.

3.1. Sample preparation

3.1.1. Thermal evaporation of In_2S_3 layers

Thermal evaporation is a physical vapor deposition (PVD) method for depositing thin films. An evaporation system includes a vacuum chamber with its accessories, evaporation source and control electronics [94]. The systems include monitors for thickness control and shutters to expose or block off the source from the substrate. A typical thermal evaporation system is illustrated in figure 3.1 (a). It consists of the source material in a crucible with resistive heating and a substrate fixed above and facing downwards towards the source in the vacuum chamber.

A typical PVD process proceeds as shown in figure 3.1 (b). The solid source material in the crucible is vaporized by resistive heating and the vapor condenses onto a colder substrate above to form a thin film layer. The thickness of the layer is monitored in terms of the amount of material deposited on to a detector consisting of a crystal

microbalance. The resonance frequency of the crystal is detuned by the increasing mass during deposition, which allows for precise control of the deposition process. For thermal evaporation the pressure in the chamber is usually between 10^{-5} to 10^{-8} mbar [94].

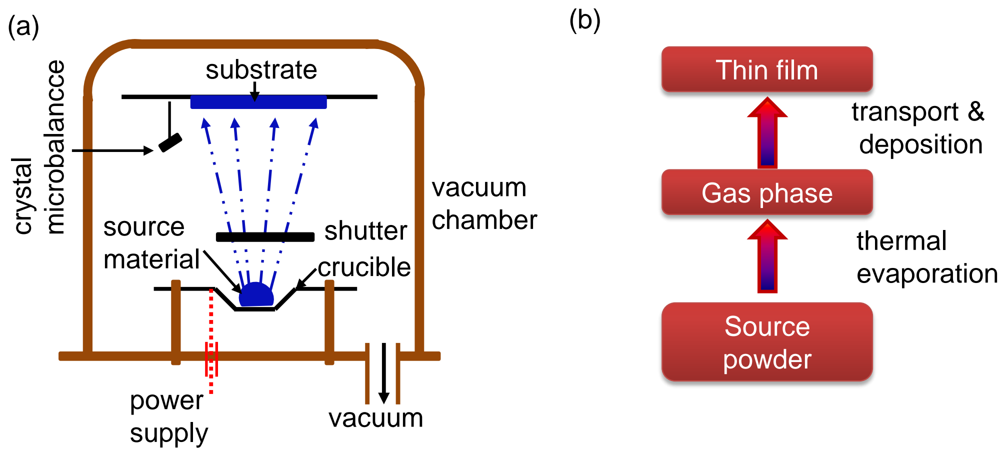

Figure 3.1: Set-up for deposition of In_2S_3 layers by thermal evaporation (a) and the sequence of the deposition process (b).

In_2S_3 layers were deposited from commercial In_2S_3 powder. In_2S_3 starts to sublime when heated in vacuum (10^{-5}mbar) at temperatures above 695°C. It has been shown in literature that maintaining the crucible temperature at about 720°C helps to preserve the composition of the vapor without preferential evaporation of sulfur [94, 95]. At higher temperatures, the difference in partial pressures of In and S results in non-stoichiometric layers with mixed composition. The crucible temperature was therefore set at 720°C with a ramp time of 30°C. The substrate was not actively heated so its temperature stayed below 50°C [96, 97]. The distance between the crucible and substrate was 40 cm.

Thermally evaporated In_2S_3 layers on SnO_2:F and c-Si substrates were used for SPV and Cu diffusion experiments, respectively. For SPV experiments, samples with varying thicknesses between 5 and 80 nm were prepared. For diffusion experiments, layers of about 100 nm thickness were used. The thicknesses of the layers were determined during deposition with the crystal microbalance and confirmed by measurements using a Dektak step profiler. In the following sections, In_2S_3 layers deposited by PVD are denoted by PVD-In_2S_3.

3.1.2. Ion layer gas reaction of In_2S_3 layers

Ion layer gas reaction (ILGAR®) method is a sequential technique for deposition of metal sulfide thin films on different types of substrates [98, 99]. A metal salt is first deposited onto the substrate from a solution and then chemically converted into a chalcogenide by exposure to a corresponding hydrogen chalcogenide gas. The reaction at the solid/gas interface ensures homogeneous and nanocrystalline layers [100, 101]. In the spray-ILGAR process the metal salt is delivered from a precursor solution. The solution is nebulized to an aerosol and transported onto a heated substrate by a nitrogen carrier gas [102]. The precursor solvent vaporizes and a very thin layer (1-2 nm) is deposited. H_2S gas is then introduced to convert the metal precursor layer to the corresponding sulfide. There is a pause between these two steps to clear the aerosol or reaction gas. These steps are repeated until the desired thickness is reached [102, 101].

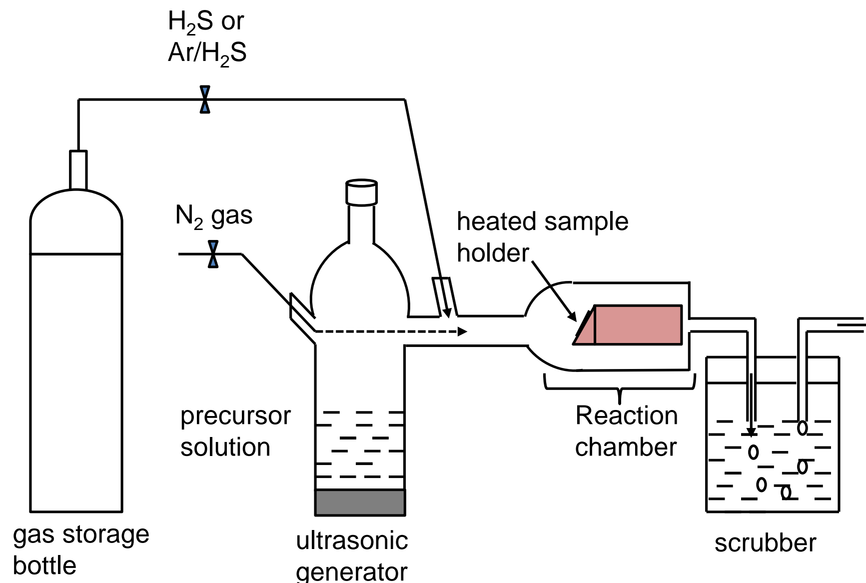

Figure 3.2: Spray-ILGAR set-up for deposition of In_2S_3 layers from precursor solutions.

A schematic diagram of the spray-ILGAR set-up is shown in figure 3.2. The spray-ILGAR setup consists of a glass vessel for holding the precursor solution connected to an ultrasonic generator. The glass vessel has an inlet for the career gas (N_2) and for H_2S gas. Two different concentrations of H_2S were available from storage bottles; pure H_2S and H_2S diluted in Ar (Ar/H_2S mixture with percentage ratio of 95/5). A horizontal tube connects the glass vessel to the sample holder made of stainless steel with an integrated

heating plate. The sample is placed on the holder tilted by 45° in order to enable a homogeneous access of the precursor to the substrate surface. The sample can be heated up to a maximum temperature of 300°C. As the aerosol comes into contact with the heated substrate, it decomposes and adheres to the surface forming a homogeneous thin film [102] in contrast to PVD. The scrubber contains NaOH and collects the waste, which includes toxic H_2S. The height of the liquid column in the scrubber is crucial and must be maintained constant. A different height results in a different back pressure and this can change the pressure condition in the reaction chamber.

The spray-ILGAR deposition process proceeds as illustrated in figure 3.3. The standard process consists of four progressive steps; 1) spraying precursor ($\Delta t_1 = 60\,s$), 2) pause to purge the system and clear the precursor aerosol ($\Delta t_2 = 10\,s$), 3) sulfurization of the deposited precursor layer using H_2S ($\Delta t_3 = 20\,s$), and 4) pause to purge the system and clear the H_2S ($\Delta t_4 = 10\,s$). These four steps constitute one ILGAR cycle [99, 102]. Each step can be modified to change the properties of the deposited layer. For example, in some cases, a continuous background flow of 5% H_2S gas was maintained together with the carrier gas throughout the deposition period.

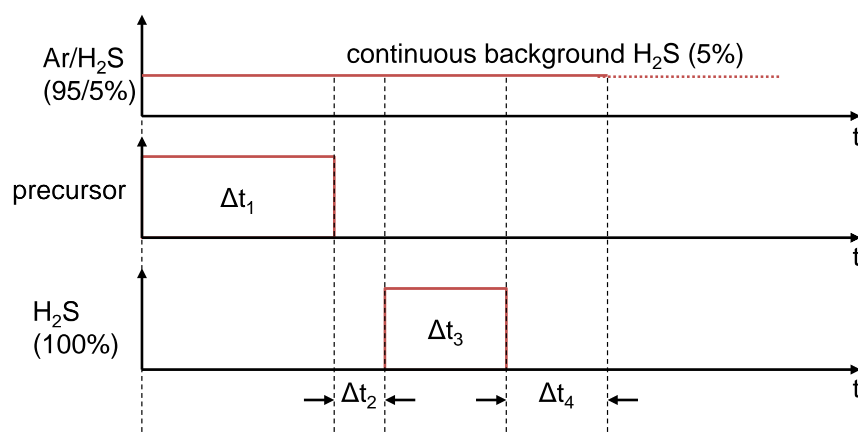

Figure 3.3: A schematic presentation of the spray-ILGAR deposition time for one cycle

$InCl_3$ precursor salt is a white powder. It has a density of 3.46 g/cm^3, molecular weight of 221.18, a melting point of 586°C and boiling point of 800°C [103]. Each In^{3+} ion is bonded ionically to three Cl^- ions as shown in figure 3.4 (a). In(acac)$_3$ is a white powder with a density of 1.41 g/cm^3, molecular weight of 412.14, melting point of 187-189°C and boiling point of 260-280°C [104]. The crystal structure of In(acac)$_3$ molecule is

shown in figure 3.4 (b). Metal acetylacetonates are complexes of acetylacetonate ions and a metal, in this case In. Three oxygen atoms of the acetylacetonate ion bind to one In^{3+} ion. Most metal acetylacetonates are soluble in organic solvents.

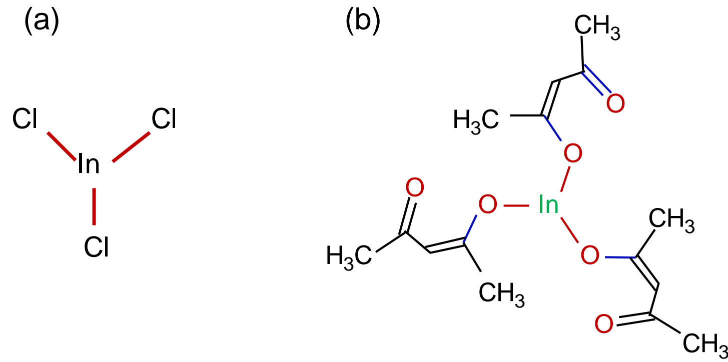

Figure 3.4: Crystal structures for (a) $InCl_3$ and (b) $In(acac)_3$ precursor salt

To prepare a precursor solution for In_2S_3 deposition, $InCl_3$ or $In(acac)_3$ salt was dissolved in ethanol in an ultrasonic bath. For example, to prepare 25 mM precursor solution of $InCl_3$, 0.553 g of $InCl_3$ salt (Alfa Aesar) was weighed on a balance and dissolved in 100 ml of ethanol. To prepare 25 mM of $In(acac)_3$ precursor solution, 1.03 g of $In(acac)_3$ salt (Sigma-Aldrich) was weighed and dissolved in 100 ml of ethanol. The precursor solution was nebulized by the ultrasonic generator. The aerosol was then transported through the glass tube to the heated substrate by the N_2 gas flow. The substrate temperature was varied between 150 and 200 °C for various experiments. The thickness of a layer deposited by one ILGAR cycle is on the order of 1-3 nm depending mainly on the time Δt_1. The deposition rate depended on the precursor type, concentration of the solution and on substrate temperature.

The amount of residual Cl in In_2S_3 layers deposited from $InCl_3$ precursor was controlled by adjusting the durations of Δt_i $(i = 1,2,3,4)$ steps. For example, increasing the duration for the spraying step (Δt_1) produces a thicker precursor layer. With a fixed sulfurization time (Δt_3), this would result in incomplete sulfurization of the precursor layer and hence higher residual Cl. On the other hand, a longer sulfurization period (Δt_3) with a fixed Δt_1 will increase the sulfurization time and a lower residual Cl content would be expected. In the following, In_2S_3 layers prepared from $InCl_3$ or

$In(acac)_3$ precursor solutions are denoted by ILGAR(Cl)-In_2S_3 or ILGAR(acac)-In_2S_3, respectively.

3.1.3. Spray-spin deposition of CuSCN

CuSCN is known to be an air-stable Cu (I) source [105] and was deposited onto c-Si / In_2S_3 layers by a modified spray-spin method [106]. CuSCN layers have been used as hole conductors for dye sensitized [107], extreme thin absorber [46] and nanostructured solar cells [13]. Usually, CuSCN layers are deposited by drop casting from a highly concentrated solution of CuSCN in propyl sulfide [107]. In our experiments, CuSCN was sprayed from a diluted solution of CuSCN in propyl sulfide. For thid purpose, a setup shown in figure 3.5 (a) was made.

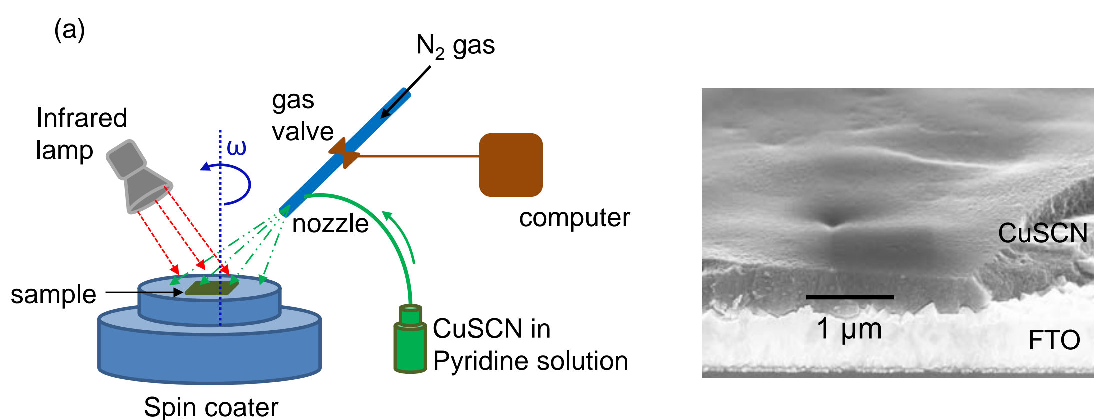

Figure 3.5: Spray-spin setup for the deposition of CuSCN from pyridine solution (a) and SEM micrograph of a cross section of a CuSCN layer deposited by 10 spray-spin cycles onto a SnO_2:F substrate (b). The sample was tilted at 30°.

The setup consists of a spin coater for holding and rotating the substrate, an infrared lamp for heating the substrate during deposition, a spray nozzle connected to a reservoir of CuSCN solution and a computer-controlled gas valve for regulating the nitrogen flow for spraying. The spray mechanism has a nozzle for spraying the solution from a small bottle through a narrow tube connected to it. N_2 gas at a pressure of 2-3 bar was used as the carrier gas. The nozzle was operated by a valve, which was controlled by a relay box and computer program.

CuSCN is a pale yellow powder insoluble in water and many other solvents. It is slightly soluble in n-propyl sulfide [107]. Two solutions were prepared with concentrations of 0.05 M and 0.11 M by dissolving 0.13 or 0.26 g of CuSCN powder in 20 ml of n-propyl sulfide and stirring continuously with a magnetic stirrer for 48 hrs. we also found that CuSCN well soluble in pyridine. This was important for removal of CuSCN from In_2S_3:Cu/CuSCN after annealing and before depth profiling with Rutherford backscattering spectrometry (RBS).

To deposit CuSCN, the substrate was first placed on the spin coater and heated using the IR lamp for about one minute. The spin coater (SPIN150-NPP) was programed to run in two steps; first rotating at 1000 revolutions per minute (rpm) for 10 s followed by 2000 or 3000 rpm for 10 s. The valve was opened to spray the solution onto the rotating substrate for 5 s during the first rotation step, and then left to dry at higher speed in the second step. This constituted one spray-spin cycle. A scanning electron microscope (SEM) micrograph of CuSCN deposited onto SnO_2:F substrate is shown in figure 3.5 (b) for a CuSCN layer deposited for 10 spin cycles from a 0.11 M solution. Ten spray-spin cycles resulted in CuSCN layers with average thicknesses of about 1 or 0.5 µm for deposition from 0.11 or 0.05 M solution, respectively.

3.1.4. Sample preparation for investigation of Cu (I) diffusion in In_2S_3 layers

The diffusion of Cu (I) into In_2S_3 layers was performed from a CuSCN source. The copper profiles were measured by RBS. For this purpose, the CuSCN layer had to be completely removed after the diffusion step. The atomic mass of Si (14) is much lower than that of In (114), Cu (63.5) and S (32). Therefore, a Si substrate does not disturb the RBS signals from In, Cu and S.

The diffusion experiments involved several steps from deposition of In_2S_3 and CuSCN layers to annealing, etching and finally Rutherford backscattering spectrometry (RBS) analysis. A scheme of these experiments is illustrated in figure 3.6 (a). First, In_2S_3 layers were deposited onto c-Si substrates of one inch diameter by either PVD or spray-ILGAR. For optimal RBS analysis, thicknesses of In_2S_3 layers of 100 nm were used. Second, a CuSCN layer was deposited by spin-spray method. Third, diffusion of Cu

was performed. Most samples were annealed for temperatures between 150 and 250°C for 5 min. C-Si/In_2S_3/CuSCN samples were cut into smaller pieces of about 7 x 7 mm sizes. Three sets of samples were identified by the deposition method for In_2S_3 layers. For each set, one reference sample was not annealed.

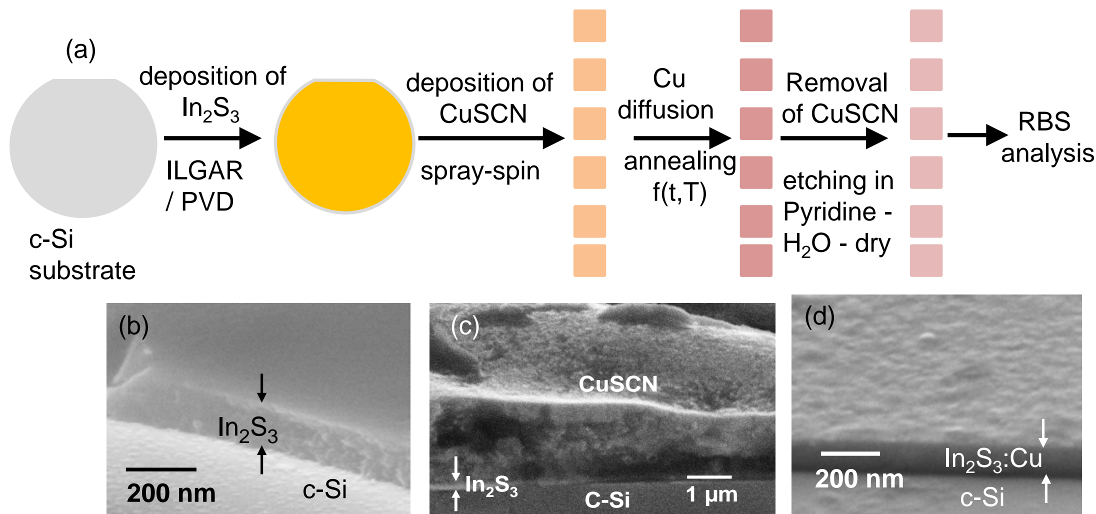

Figure 3.6: Scheme of the diffusion experiment involving deposition of In_2S_3 and CuSCN layers, annealing at different temperatures for 5 min, removal of CuSCN by etching in pyridine solution and RBS analysis. SEM micrographs for c-Si/In_2S_3 (b), c-Si/In_2S_3/CuSCN (c) and c-Si/In_2S_3:Cu after annealing at 200°C for 5 min and etching away CuSCN (d) are shown.

Fourth, CuSCN was successfully etched away from the annealed c-Si/In_2S_3/CuSCN samples in a cyclic process. The sample was first dipped into pyridine solution for 1 sec, then rinsed in water and dried in a flow of N_2 gas. This procedure was repeated until CuSCN was completely removed. Figure 3.6 (b-d) give an impression about the layer thicknesses and surface morphologies before deposition of CuSCN (b), after deposition of CuSCN (c) and after removal of CuSCN (d). The thickness of In_2S_3 remained constant while the roughness increased after annealing and removal of CuSCN. The remaining c-Si / In_2S_3:Cu samples were taken for RBS measurements and analysis. Details of the RBS analysis are presented in section 3.2 of this chapter.

3.1.5. Screen printing of nanoporous TiO_2 layers

Nanoporous-TiO_2 layers were prepared by screen printing a commercial paste of nanoparticles on SnO_2:F substrates. Glass substrates coated with SnO_2:F were used for surface photovoltage (SPV) measurements. The substrates were cleaned in acetone followed by ethanol placed in an ultrasonic bath for 3 min each and then rinsed in di-ionized water. The substrates were then dried by blowing with N_2 gas. A commercial paste containing nanoparticles of 25 nm diameter was placed onto a screen on top of the SnO_2:F substrate and spread over the substrate as shown in figure 3.7 (a). The fresh np-TiO_2 layer was first dried at 120°C for two minutes 4 min after printing.

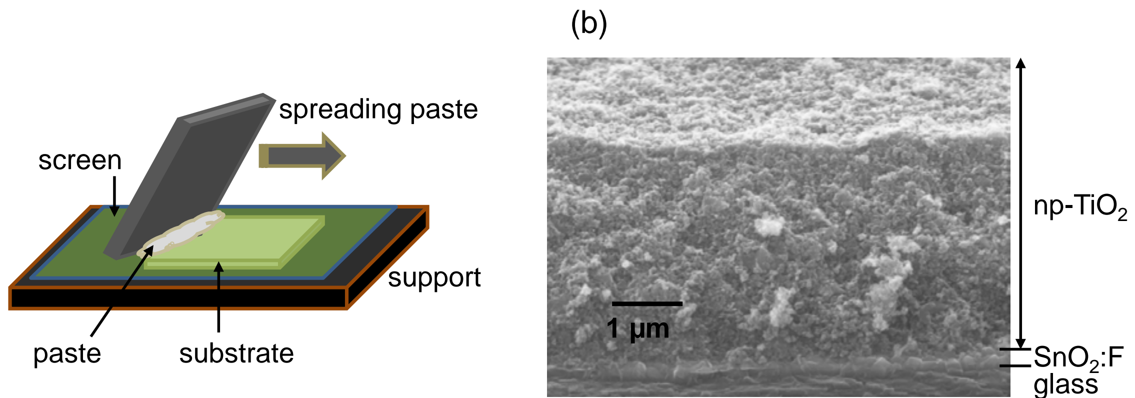

Figure 3.7: Setup for screen printing of nanoporous TiO_2 layers from paste (a) and SEM micrograph of a cross section of a np-TiO_2 layer on SnO_2:F coated glass tilted at 30°(b).

The SnO_2:F/np-TiO_2 substrates were annealed on a hot plate in the following steps: first ramping the temperature to 280°C in 10 min, holding it constant at 280°C for 10 min, followed by ramping up the temperature to 380 °C in 5 min and holding it constant for 15 min, and again ramping the temperature up to 520 °C in 10 min and holding it constant for 30 min. The samples were then left to cool slowly. The organics in the paste were burned out during annealing leaving behind a porous layer of interconnected TiO_2 nanoparticles. The thickness of the np-TiO_2 layers was measured using Dektak step profiler and amounted to about 3µm. A SEM micrograph of np-TiO_2 layer on SnO_2:F substrate is shown in figure 3.7 (b).

3.2. Rutherford backscattering spectrometry analysis

Rutherford backscattering spectrometry (RBS) is a fast and non-destructive method which has been used for depth dependent stoichiometry analysis of materials. RBS utilizes ions scattered by nuclei at a given depth when an incident ion beam penetrates a sample [108]. It is well suitable for the analysis of elements in a layer that are heavier than the elements of the substrate. RBS is an absolute method used for determination of stoichiometry, elemental composition or distribution of an impurity with depth in a material. In this work, RBS was used to investigate depth distribution and diffusion parameters of Cu in different In_2S_3 layers.

3.2.1. Instrumentation for Rutherford backscattering analysis

Typical setups for RBS experiments consist of devices for ion generation and handling, target system and detection and analyzing system [109] as shown in figure 3.8. An ion beam is generated by the ion source and accelerated to energies in the order of MeV before impinging onto the target. Backscattered ions are detected and processed by linear and digital electronic devices to produce a spectrum on a computer.

The beam generation and the beam handling systems consist of the ion source, the accelerator, the ion focusing system, the magnet and the collimator [109]. For RBS, ions beams are typically produced by Van de Graaff accelerators of a few MeV with about 10^{-4} relative resolution. Tandem accelerators are more versatile than Van de Graaff accelerators having a negative ion source outside the accelerator. Ions from the accelerator pass through the analyzing magnets and through the switching magnet which direct the beam to the appropriate beam line. Electrostatic and /or magnetic focusing and steering deflectors direct the beam towards the experimental target chamber [110].

The collimator is a system of diaphragms for shaping the beam, limiting the angular divergence and protecting the target from scattered particles. Ions scattered from the edges of the diaphragms may cause background signal because they strike the target outside the beam spot or on the sample holder. This is eliminated by the use of anti-scattering diaphragms [109, 110].

The target system consists of the sample holder, the beam measurement devices, the detector system and other devices within the vacuum chamber [109]. In most laboratories, several different sample holders are required for routine or specialized experiments.

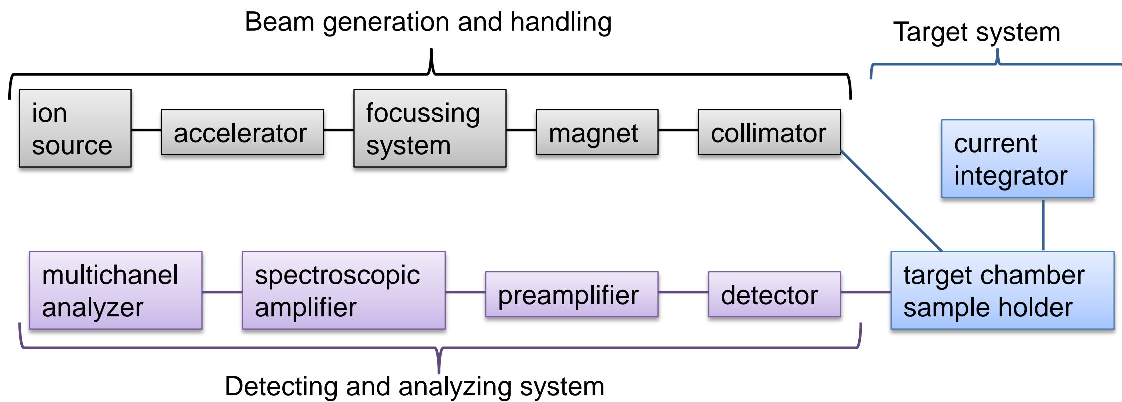

Figure 3.8: Block diagram of the experimental arrangement for RBS measurements

The detecting and analyzing system consists of the detector, the preamplifier, the spectroscopic amplifier and the multichannel analyzer [109]. The detector measures the energy of the scattered ions [110]. Electric or magnetic detectors use homogeneous electric or magnetic field of a cylindrical capacitor as energy dispersive elements for backscattered particles, respectively. Magnetic detectors have better energy resolution but they require longer data accumulation times [111].

Semiconductor detectors are usually silicon or germanium p-n or p-i-n diodes or surface barrier diodes operated in reverse mode [109]. Ionizing radiation penetrating the depletion layer generates charge carriers which are collected at the electrodes. The number of carriers generated by one ion is proportional to its energy. Thus the generated carriers provide information about the energy of the ionizing radiation and the time of occurrence. In reverse mode, a thick enough depleted layer is formed at the front side from which free charge carriers created by the backscattered ions can be extracted and collected [110].

The output signal from the detector is amplified by the charge-sensitive preamplifier designed to preserve signal-to-noise ratio [109]. The preamplifier output is shaped and filtered by the spectroscopic amplifier to improve signal-to-noise ratio and shorten the

pulse length. The output pulse has a constant shape with amplitude proportional to the height of the input step pulse.

Multichannel analyzer (MCA) is a set of devices that allow data acquisition, storage, display and interpretation [109]. They may be connected to a computer for the purpose of data acquisition, management and storage. An input signal causes an increase of one register in the memory corresponding to a channel of the spectrum. Suitable software is needed for energy calibration, energy to depth conversion and computation of depth profiles and concentrations of atoms in the target.

3.2.2. Fundamentals of Rutherford backscattering spectrometry

In a RBS experiment, a well-collimated mono-energetic ion beam of energy E_0 and atomic mass M_1 impinges on to a target with atoms of masses M_2^i ($i = 1,2,3, ...$). The detector registers ions backscattered at an angle θ in a solid angle $\Delta\Omega$ given by the detector geometry [109]. The energy of the detected ions gives information about the identity of the atoms present in the target and about the depth from where the scattering process took place. The number of detected ions provides information on the quantity of atoms in the target.

The three main concepts of RBS can be summarized as (i) kinematic factor which enables analysis of target composition, (ii) differential scattering cross section which allows quantitative analysis and (iii) energy loss which makes possible depth profiling [108]. Each of these concepts has analytical ability that makes RBS a method of choice for material analysis.

Kinematic factor and mass resolution

During a backscattering process, the incident ion of mass M_1 collides with a stationary atom of mass M_2 and some energy is transferred from the incident ion to the target atom. The energy of the backscattered ion (E) is reduced after collision and can be expressed as [109, 111],

$$E = KE_0 \quad (3.1)$$

where K is called kinematic factor and depends only on the scattering angle and the ratio of the masses M_1/M_2 according to

$$K = \left\{ \frac{\cos\theta + \left[(M_1/M_2)^2 - \sin^2\theta\right]^{1/2}}{1 + M_2/M_1} \right\}^2 \quad (3.2)$$

The lowest and highest values of K are at $\theta = 180°$ and at $\theta = 90°$, respectively. From equation 3.6 we obtain,

$$K(\theta = 180°) = \left(\frac{M_2 - M_1}{M_1 + M_2}\right)^2 \quad (3.3)$$

$$K(\theta = 90°) = \frac{M_2 - M_1}{M_1 + M_2} \quad (3.4)$$

Low values of K mean that the energy difference between the incident and backscattered ions is large. In practice, the detector is placed at angles $\theta < 180°$; typically at $\theta \approx 160°\ or\ 170°$. Mostly H^+ or He^+ ions are used for backscattering experiments. Because of the dependence of K on M_2, the atoms in a target can be identified using equation 3.6 by measuring the energy E of the scattered ions, provided that M_1 and E_0 of the incident ion are known [109]. The elemental composition of a target sample can therefore be determined by RBS measurements.

As an example, figure 3.9 shows simulated RBS spectra of In_2S_3 layers of different thicknesses deposited on silicon. Typical RBS spectra for In_2S_3 layers of different thicknesses on c-Si substrate are shown in figure 3.9. The spectra were calculated for ion beam energy of 1.4 MeV, an incident angle 0°, a scattering angle of 170°, a solid angle of 5 msr and a charge of 5 µC. The measurement geometry is shown as an insert in figure 3.9.

The position of the peaks depends on the atomic mass of the respective element detected. The signals from In appear at channel numbers 370 to 440 and S at channel numbers 250 to 300. The width of the peak corresponds to the thickness of the layer. The continuous part at low channel numbers refers to the Si substrate. The position of the Si surface or onset of the signal from Si substrate shifted depending on the thickness of the In_2S_3 over-layer. For a thick over-layer, the incident as well as backscattered ions

will travel a longer distance to and from the Si surface, respectively, thereby losing more energy due to collisions with atoms in the over layer.

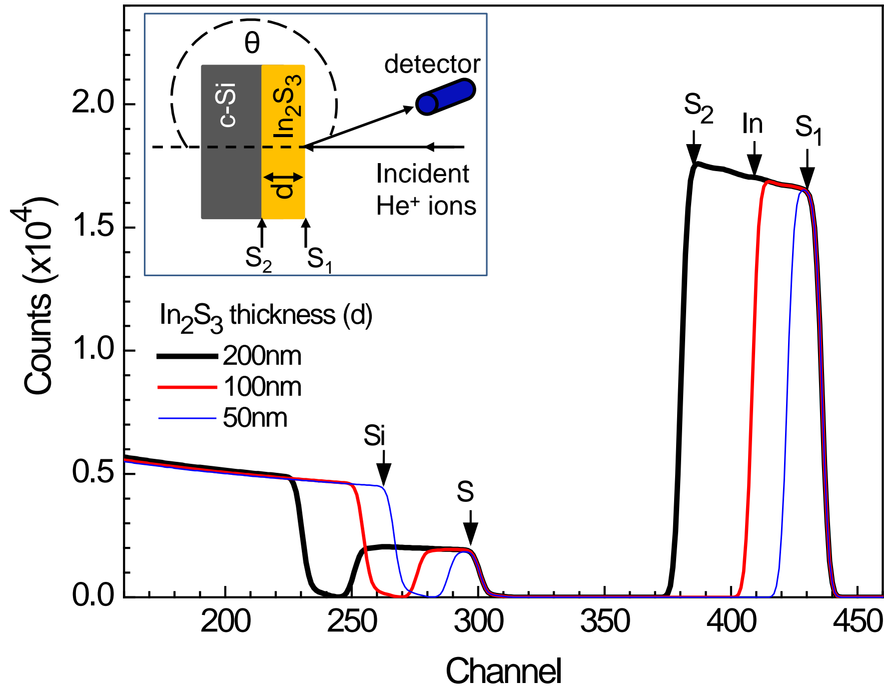

Figure 3.9: RBS spectra of In_2S_3 layers with different thicknesses on Si substrate. The insert shows the measurement geometry. S_1 and S_2 denote the signals from the front and back surfaces of the thickest In_2S_3 layer, respectively. Spectra for the different thicknesses were calculated for an ion energy of 1.4 MeV, a scattering angle of 170°, an incident angle of 0°, a solid angle of 5 msr and a charge of 5 μC.

To differentiate two atom types in a target, the difference in the energy of the ions scattered by the two atoms M_2^1 and M_2^2 should be as large as possible. To distinguish between the two atom types whose difference in mass is δM_2 the energy change ΔE_2 must be greater than the energy resolution δE_d of the detector. The limit is given by [109],

$$\delta E_d \leq \Delta E_2 = E_0 \left(\frac{dK}{dM}\right) \delta M_2 \qquad (3.5)$$

To obtain good resolution, the coefficient of δM_2 has to be as large as possible. This can be achieved by (i) increasing the primary energy E_0, (ii) using large mass M_1 and (iii) measuring at scattering angles very close to 180° [111]. For He^+ ions with energy $E_0 = 1.4\ MeV$, the energy resolution of the detector δE_d was 14 KeV (FWHM) for the

measurements performed at the RBS system in the ion beam lab, Institute of solid state Physics, University of Jena.. Resolution for neighbouring masses with $\delta M_2 = 1$ is only possible up to target masses $M_2 = 32\, amu$ [109]. Generally, mass resolution deteriorates for higher target masses.

Scattering cross section

The scattering cross section (σ) is the probability of a scattering event to occur and result in a signal in the detector [111]. If Q is the total number of incident particles hitting the target and dQ the number of detected particles recorded by the detector in a solid angle $d\Omega$, the differential scattering cross section is defined as,

$$\frac{d\sigma}{d\Omega} = \left(\frac{1}{Nt}\right)\left[\frac{(dQ/d\Omega)}{Q}\right] \qquad (3.6)$$

N is the volume density of atoms in the target and t its thickness. Nt is the number of target atoms per unit area also called areal density. The number of scattering events within a finite solid angle Ω is described by the integral scattering cross section Σ,

$$\Sigma = \int_{\Omega} \left(\frac{d\sigma}{d\Omega}\right) d\Omega \qquad (3.7)$$

The detector angle of a typical detector system with a surface barrier detector is of the order of $10\, msr$ or less $(1\, sr\ = (180°/\pi)^2)$. The scattering cross section is therefore given as [111],

$$\sigma \equiv \left(\frac{1}{\Omega}\right) \int_{\Omega} \left(\frac{d\sigma}{d\Omega}\right) d\Omega \qquad (3.8)$$

The Rutherford cross section is expressed as [111],

$$\frac{d\sigma}{d\Omega} = \left(\frac{Z_1 Z_2 e^2}{4E}\right)^2 \frac{4}{sin^4\theta} \frac{\left\{\left[1-\left((M_1/M_2)sin\theta\right)^2\right]^{1/2} + cos\theta\right\}^2}{\left[1-\left((M_1/M_2)sin\theta\right)^2\right]^{1/2}} \qquad (3.9)$$

Z_1 and Z_2 are the atomic numbers of the incident particle and target atom with mass M_1 and M_2, respectively. The order of magnitude of the differential cross section is given

by the factor $\left(\frac{Z_1 Z_2 e^2}{4E}\right)$. For larger backscattering angles and $(M_1/M_2) \ll 1$, equation (3.14) can be approximated to [111],

$$\sigma \cong 0.02073 \left(\frac{Z_1 Z_2}{4E}\right)^2 \left[sin^{-4}\left(\frac{\theta}{2}\right) - 2\left(\frac{M_1}{M_2}\right)^2\right] \qquad (3.10)$$

where E is given in units of MeV and σ in b/sr $[1b(barn) = 10^{-24}\, cm^2]$. $e^2 = q^2/4\pi\varepsilon_0 = 1.4398 \times 10^{-13} MeV$, where $\varepsilon_0 = 8.85434 \times 10^{-12} Asec/Vm$ and $q = 1.602 \times 10^{-19} A\, sec$. Taking an energy of 1 MeV for the incident ion beam, the ratio $(q^2/4\pi\varepsilon_0 E)$ becomes $((1.60206 \times 10^{-19})^2/4\pi \times 8.85434 \times 10^{-12}) = 2.0731 \times 10^{-30} m^2$. This is equal to $0.020731\, b$. Tables of scattering cross section of elements for 1 MeV He^+ ions as a function of scattering angles can be found in literature [109, 111, 112].

Given the values of σ and Ω, the number of incident and detected particles can be counted and the number of atoms per unit area (areal density) can be calculated. The total number of detected particles is given by,

$$A = \sigma \cdot \Omega \cdot Q \cdot Nt \qquad (3.11)$$

Energy loss and depth profiling

When an incident ion penetrates a target and is scattered at a depth z from the surface, the energy of the scattered ion will be affected by the energy loss due to inelastic scattering events with the electrons and small angle elastic collisions with the nuclei of the target atoms. The energy loss (dE) per unit length (ds) is called specific energy loss or stopping power and depends on the atomic number of the ion, the composition of the target and the ion energy [109]. The stopping cross section (ε) is therefore defined as,

$$\varepsilon = \frac{1}{N}\left(\frac{dE}{dS}\right) \qquad (3.12)$$

During its travel from the surface to the depth z, the ion loses some energy and its energy just before collision is E_1. Its energy just after elastic scattering becomes $E_1 K$. On its way out of the target, the ion losses more energy and eventually leaves the target

with energy E_2. In a RBS experiment the energy of the backscattered ions is measured but the depth and the identity of the target atom may not be known. To get information about the depth position of the scattering atom, the energy scale of the RBS spectrum has to be converted into a depth scale [109]. This is achieved using tabulated values of $\varepsilon(E)$ with software developed for this purpose.

The stopping cross section of a compound A_mB_n is obtained by linear combination of the stopping cross section values of the elements weighted by their respective amount in the compound. This is referred to as the Bragg's law and is expressed as [111],

$$\varepsilon^{AB} = m/(m+n)\,\varepsilon_A + n/(m+n)\,\varepsilon_B \tag{3.13}$$

The accessible depth (z_a) is the region under the surface which can be investigated. This is usually of the order of $1 - 10\ \mu m$ but depends mainly on the ion energy, ion mass and the target properties [109]. The maximum measurable depth is determined by the lowest energy of the backscattered ions recorded by the detector. General criteria for determining z_a is such that all ions with energy in the range

$$\Delta E_2 = \frac{3}{4} K E_0 = [\varepsilon] N z_a \tag{3.14}$$

will be detected. $[\varepsilon]$ is the stopping cross section factor. The value of z_a depends a lot on the incidence and exit angles between the beam and normal to the target. Depth resolution (δz) is given by the uncertainty in E_2. For RBS measurements, depth resolutions of up to 0.5 nm can be achieved [113].

3.2.3. Experimental conditions and analysis of depth profiles

RBS measurements were performed using the 3 MV Tandetron-accelerator named "JULIA" (Jena University Laboratory of Ion Accelerator) with assistance from the ion beam physics group. A multiple sample holder that holds up to 9 samples was. The sample to be measured was selected by rotating the sample holder until it was directly facing the incident ion beam. Rotation could be done in a vertical axis perpendicular to the ion beam (-180° to +180°) or tilting around a horizontal axis perpendicular to the ion beam (-10° to +10°) using a precision goniometer.

A He^+ ion beam with an energy of 1.4 MeV was used at normal incidence to the sample. The scattering angle was 168° and the charge of the incident ions was 10 μC. The measurement time was about 10-12 min per sample. The spectra were recorded and saved on a personal computer using RUBSODY[1] software.

Nuno's Data Furnace (NDF) code [114, 115] was used to calculate the RBS spectra from experimental parameters. The code solves the so called RBS inverse problem by determining the depth profiles from the RBS spectra. To handle the spectra and control experimental parameters, SPEWA [116] software was used. A screen shot of the data handling program is shown in figure 3.10.

Experimental details such as the ion beam energy, scattering angle, incident angle, charge, energy resolution of the detector, solid angle and measurement geometry are entered into the program. The elements present in the sample and their atomic densities were entered. The layer structure for example, an In_2S_3 layer on top of c-Si substrate, was defined in relation to the elemental composition.

For the analysis of Cu diffusion in In_2S_3 layers, a constant atomic density of In_2S_3 was used because the amount of diffused Cu was relatively low to cause a significant influence. The atomic density (N) of In_2S_3 was calculated from the expression,

$$N(cm^{-3}) = \frac{\rho\left(\frac{g}{cm^3}\right) . N_A(mol^{-1})}{m(g/mol)} \qquad (3.15)$$

where ρ is the density, $N_A = 6.02 \times 10^{23} mol^{-1}$ the Avagadro's number and m the molar mass. For In_2S_3, $\rho = 4.90\ g/cm^3, m_{In2s3} = 2/5\, m(In) + 3/5\, m(S) = 2/5\,(114.82) + 3/5\,(32.06)$ giving atomic density of $4.53 \times 10^{22} cm^{-3}$. The optimal thickness for analysis of Cu diffusion in In_2S_3 layer was determined by simulation such that the signal from Cu is not disturbed by that from In. In_2S_3 layer of about 100 nm thickness was chosen after preliminary simulations using SPEWA software for which the In and Cu signal cannot overlap.

---

[1] RUBSODY Software was developed in-house for handling measured data by the ion beam group in Institute of Solid State Physics, University of Jena, Germany.

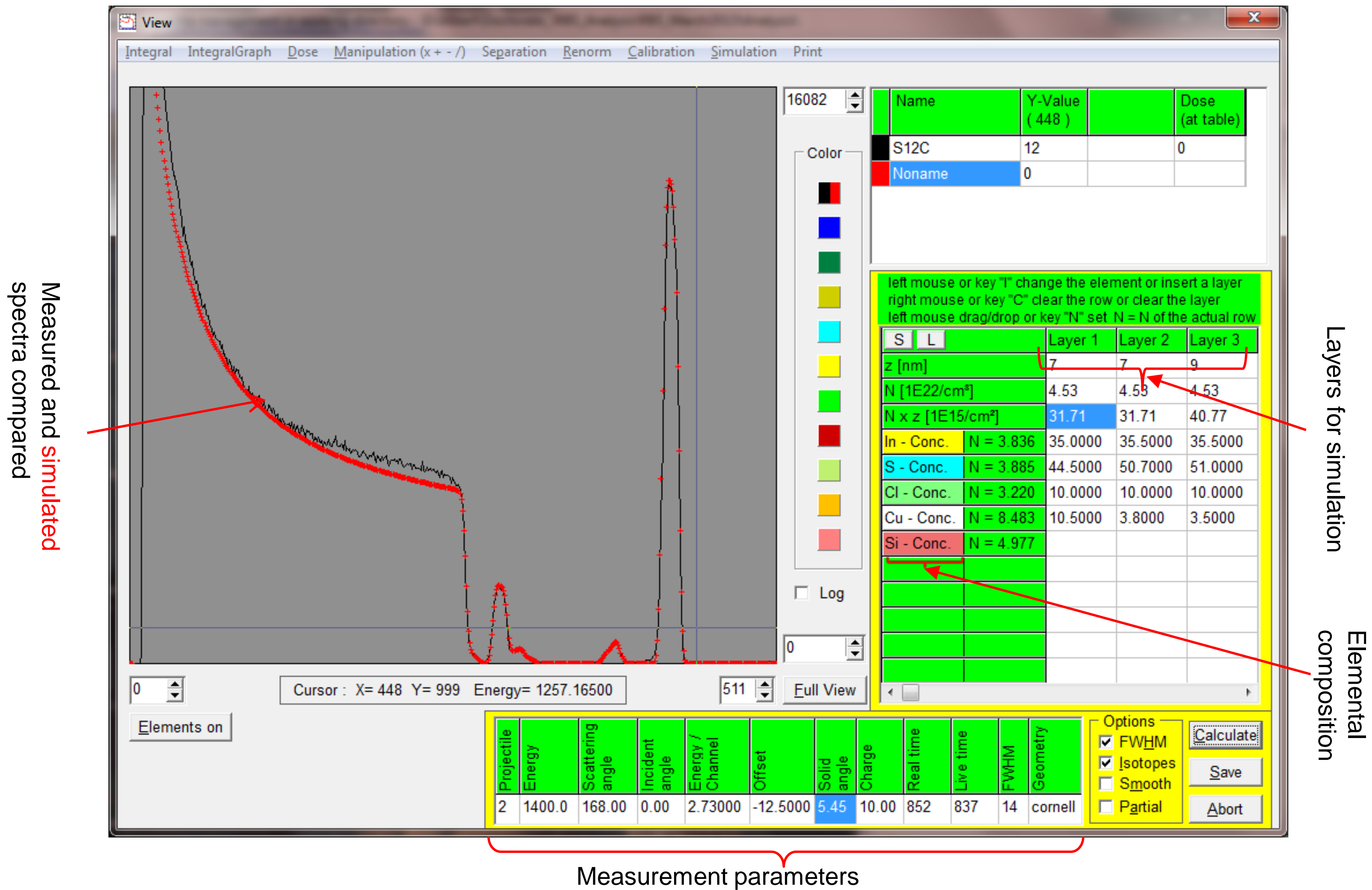

Figure 3.10: Screen shot of the software used for simulation of RBS spectra

The layer thickness was divided into several sub layers called layer 1, layer 2 and so on. The thickness and stoichiometry of each layer were adjusted each time and the theoretical RBS spectra corresponding to the set layer structures calculated and compared to the measured data in the same window as shown in figure 3.10. The stopping cross section values were calculated by the program from a database of tabulated elemental values using Bragg's law (equation 3.17) [115].

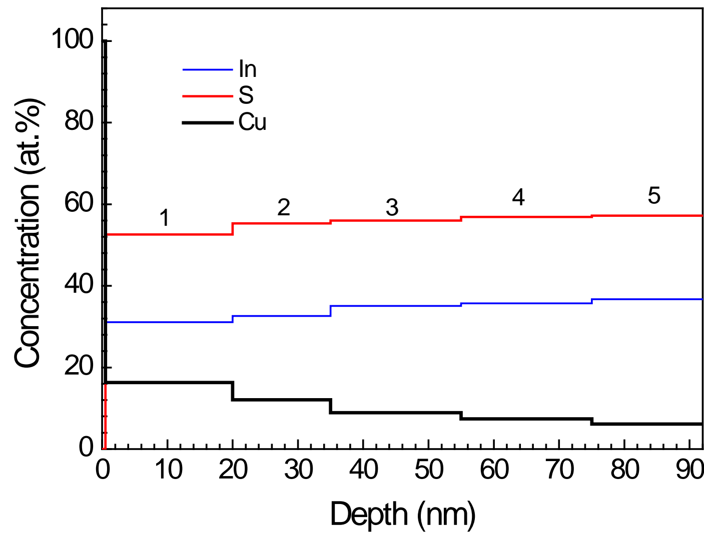

Figure 3.11: Depth profile extracted from simulation of RBS spectrum

An example of depth profiles obtained for a layer of In_2S_3:Cu is shown in figure 3.11. The In_2S_3:Cu was sub divided into five layers as indicated in figure 3.11. The concentrations of In, S and Cu changed with the depth. The depth scale was converted from the areal density in units of cm^{-2} to nm by dividing areal densities by the atomic density N (see equation 3.19). The total amount of each element was obtained from the integral of the respective signal in the spectra and/or integrating the depth profiles.

3.3. Surface photovoltage and surface analysis

Surface photovoltage (SPV) spectroscopy is a highly sensitive and nondestructive method for investigating charge separation in semiconductor materials. Directed photo-induced charge separation at a surface or interface is detected as a voltage and provides information about defect states, charge transport and recombination mechanisms. SPV

has also been applied for the determination of surface band bending and distribution of surface states [117, 118], charge carrier diffusion length [119], energy band alignments [120] and formation of charge-selective contacts [106]. It can be applied to thin film structures, multilayers, bulk semiconductor systems as well as complete devices.

3.3.1. Surface photovoltage principle

SPV can be defined as an illumination induced change the surface work function. This change can be a result of charge transfer and/or redistribution due to illumination [121]. SPV signal is formed when there is charge generation and separation in space. Non-uniform generation and recombination of charge carriers can also result into a SPV signal [121].

When two materials of different work functions are connected electrically, electrons will flow from the material with the smaller work function to that with higher work function until the Fermi levels are aligned as shown in figure 3.12 (a) [122]. This arrangement forms a capacitor configuration. The difference in their work functions is called contact potential difference (CPD). Under illumination, free charge carriers are generated and the change in the surface dipole results in a change of the semiconductor's work function, shown in figure 3.12 (b). The change in the surface work function induces a current to flow through a large resistance between the semiconductor and the reference electrode until the Fermi levels are re-aligned. The change in the CPD due to illumination is measured as a voltage across a measurement resistor (R_m). The measurement time is limited by the $R_m C$ time constant, where C is the capacitance. The SPV signal is equal to the negative change in the CPD ($SPV = -\Delta CPD$).

The SPV signal is proportional to the number of charges (Q) separated in space and the perpendicular distance (d) between the centers of the charges as illustrated in figure 3.12 (c).

$$SPV = \frac{Q}{\varepsilon\varepsilon_0}.d \qquad (3.16)$$

ε is the dielectric constant of the semiconductor and $\varepsilon_0 = 8.85 \times 10^{-14} As/Vcm$ is the permittivity of free space. The number of separated charges and charge separation

distance depend on the wavelength of illumination, absorption properties of the sample, defects and other material properties [122].

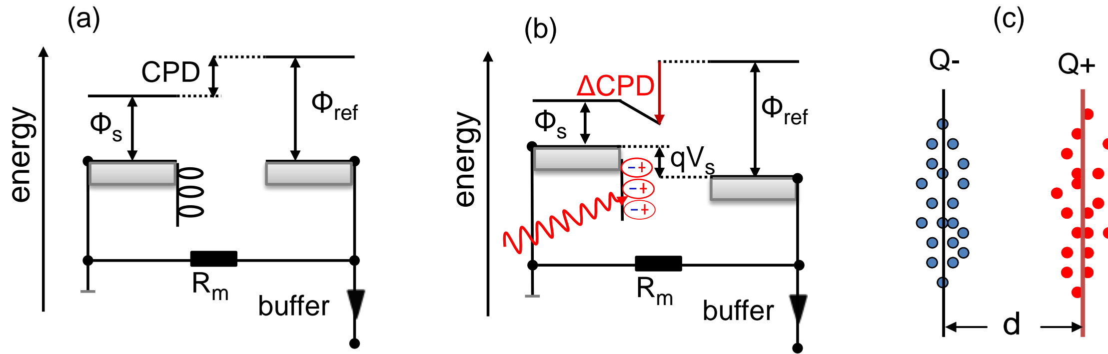

Figure 3.12: Illustration of the SPV principle (a) in the dark and (b) under illumination. The magnitude of the SPV signal depends on the amount of charges separated and the distance between the centers of the charges (c).

3.3.2. Spectral dependent surface photovoltage measurements

Modulated spectral dependent SPV measurements were carried out in the fixed capacitor configuration shown in figure 3.13. In this arrangement, a 10-30 µm thick mica sheet was placed between the sample electrode and a quartz cylinder of about 7 mm diameter coated on the front side with SnO_2:F. The quartz cylinder with the SnO_2:F electrode was pressed gently onto the sample using a cardanic spring. The SnO_2:F electrode, the mica sheet and the sample formed a parallel plate capacitor arrangement. The capacitance of this arrangement was of the order of $100\,pF$. The SPV signal generated under illumination was measured across a measurement resistance $R_m = 10\ G\Omega$ using a lock-in amplifier [122]. Therefore the modulation period should be shorter than 1 s.

The incident light was chopped at a frequency of 8 hz. A halogen lamp was used as a light source. A prism monochromator between the halogen lamp and the chopper was used to select the wavelength for illumination. A reference signal from the chopper was fed into the lock-in amplifier. The lock-in amplifier measured the signal from the sample as an in-phase (X) and a phase-shifted by 90° (Y) signal with respect to the chopped light.

The X signal follows the modulation of the reference signal and contains information about the direction of charge separation. A positive or negative X signal implies photo-induced electrons are separated towards the internal or outer surface, respectively. The Y signal characterizes the phase shift between the SPV signal and the chopped light [76]. It points to a slow increase or decrease of the SPV signal in relation to the half period of modulation. The amplitude of the SPV signal is given by

$$SPV_{amp} = \sqrt{X^2 + Y^2} \qquad (3.17)$$

and the phase angle by

$$\varphi = tan^{-1}(Y/X). \qquad (3.18)$$

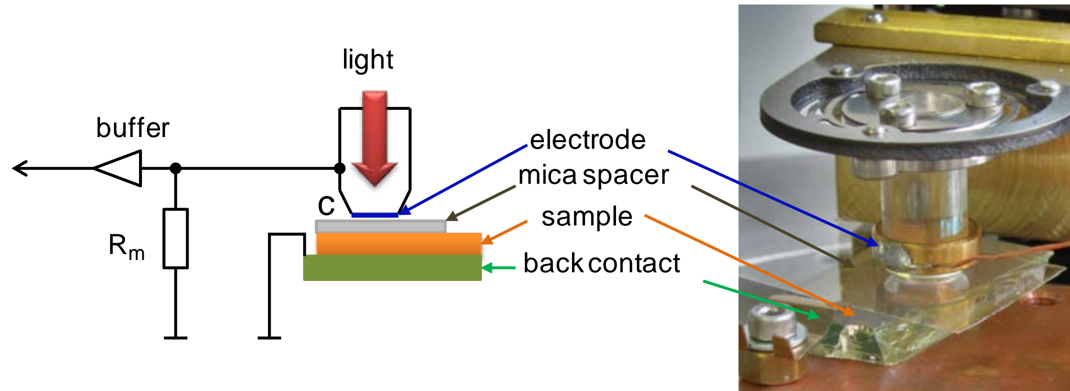

Figure 3.13: SPV measurement in the fixed capacitor arrangement

The wave at the maximum of the SPV amplitude cannot be related to an absorption peak or a peak as in spectroscopy. The SPV signal is given by the absorption and photon flux as well as the dependence of charge transfer relaxation on the light intensity and the electronic states involved [123]. The SPV amplitude is only proportional to the photon flux in the low signal case and if there is only one mechanism of charge separation and recombination. Therefore the only parameters that can be reliably extracted from the SPV amplitude are the (i) maximum amplitude, (ii) the characteristic energy parameter of the tail states and (iii) the SPV onset energy characteristic of the mobility edge.

For unchanged mechanisms of charge separation and relaxation, the distribution of defect states below the band gap can be investigated by dividing the normalized SPV

amplitude by the photon flux. Fitting the leading edge of the normalized SPV divided by photon flux $(SPV_{amp}^{ph}/\Phi\ )$signal with an exponential function gives a tail energy parameter (E_t) that characterizes the distribution of the tail states.

$$\frac{SPV_{amp}^{ph}}{\Phi} = A \cdot \ exp\left(\frac{hv}{E_t}\right) \qquad (3.19)$$

For conventional semiconductors, the onset of the SPV signal is a signature of the band gap in the sense of mobility band gap. This is different from the optical band gap, and usually lower in value, because it includes contributions to charge separation from states below the band gap. Further, one has to keep in mind that surface states can also contribute to the SPV signal.

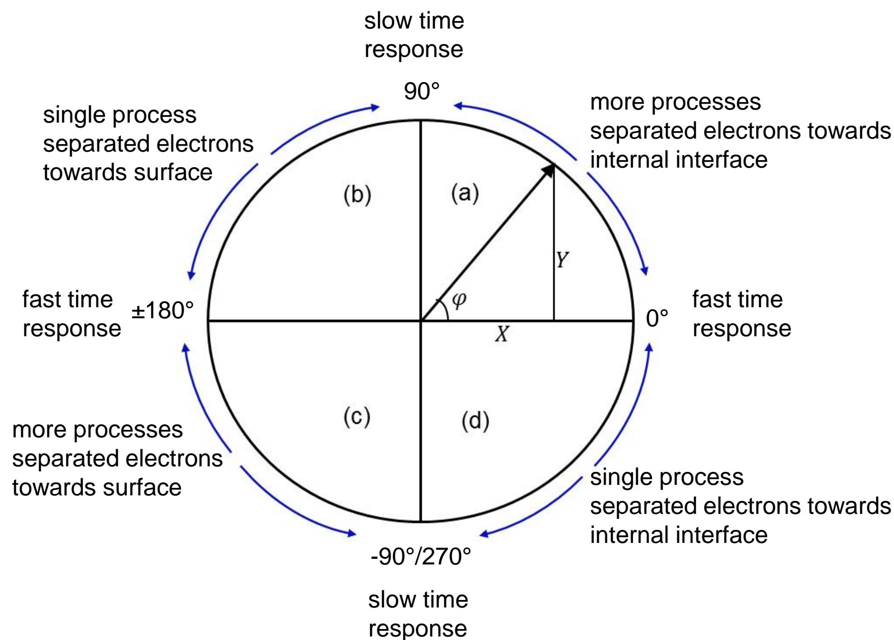

Figure 3.14: SPV phase angles with corresponding time response characteristics in relation to the modulation of the incident light. Description in the text.

The phase angle φ of the SPV signal gives information about the direction of charge separation and the time response of the sample in relation to the period of modulation and can be explained using figure 3.14. For example, φ value of 0° or 180° means fast spectral response which follows the modulation of the incident light. A value of φ between 0° and -90° corresponds to charge separation with electrons separated preferentially towards the internal surface, respectively [106]. In addition, a positive

value of X with $0° \leq \varphi \leq 90°$ implies that there is more than one process of charge separation and relaxation with photo-excited electrons separated preferentially towards the internal interface [123]. On the other hand, a negative value of X with $-180° \leq \varphi \leq -90°$, means that there is more than one process of charge separation and relaxation with photo-excited electrons accumulating at the surface.

3.3.3. Transient surface photovoltage measurements

Time-resolved SPV measurements were performed with the setup illustrated in figure 3.13. In these measurements, illumination was done using laser pulses of 5ns width and energy of 3-5 $\mu J/cm^2$. The measurements were taken in the time range between $1\ ns$ and $100\ ms$. A Nd:YAG laser (ESKPLA) with tunable wavelength between visible to infrared range was used for illumination. The transients were recorded with a repetitive rate of 0.2 Hz and averaged over 8 measurements using an oscilloscope (HP 54510B, 500 MHz). A part of the light pulse was reflected by a beam splitter to a Si photodiode with an amplifier for triggering. For each measurement condition, a transient was measured in the dark and subtracted from the transients under illumination to reduce noise.

SPV transients allows for investigation of dynamic properties of photo-induced charge transfer processes. Direct information on generation, separation and recombination of photo-excited charge carriers can be obtained [124]. A positive (negative) transient denotes faster separation of photo-excited electrons (holes) towards the internal interface.

3.3.4. Ultraviolet photoelectron spectroscopy

Photoelectron spectroscopy is a method used for investigating occupied electronic states of materials. An electron is excited by a photon from a ground state to the vacuum level and its kinetic energy is measured with reference to the Fermi level [125]. When the energy of excitation is less than 100 eV, the method is called Ultraviolet photoelectron spectroscopy (UPS). If the excitation energy is > 100 eV then it is x-ray photoelectron spectroscopy (XPS) [125, 126]. UPS was used to measure the work

function of ILGAR-deposited In_2S_3 layers. This was achieved by measuring the kinetic energy spectrum of the emitted electrons as illustrated in figure 3.15. The kinetic energy of the emitted is given by Einstein's photoelectric equation;

$$K \cdot E = h\upsilon - I \qquad (3.20)$$

where $h\upsilon$ is the energy of the incident beam and I the ionization energy.

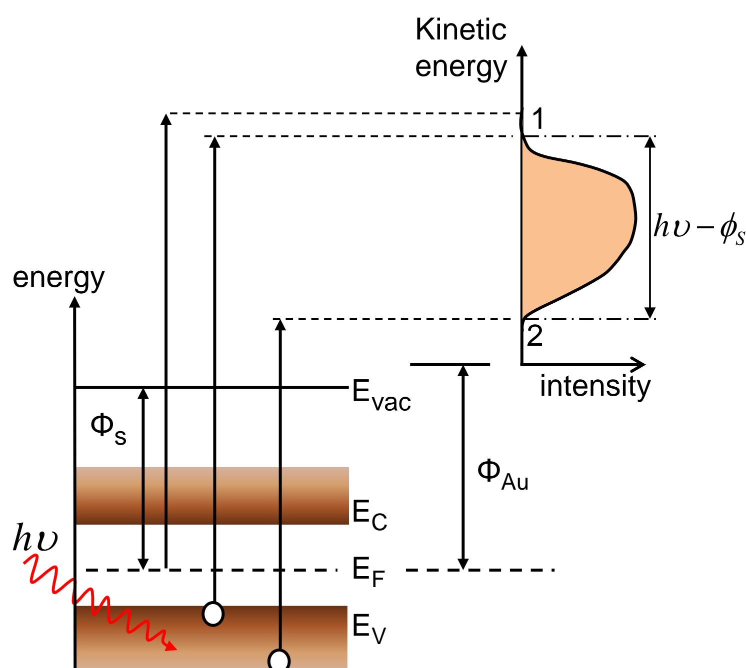

Figure 3.15: Energy excitations in ultraviolet photoelectron spectroscopy (UPS).

The work function was determined by first extrapolating the edges of the spectra at position 1 and 2 to the abscissa as shown in figure 3.15. The difference in the energy between 1 and 2 gives the width of the spectrum which is equal to the difference between the energy of the incident photon and the work function. The UPS measurements were performed in an ultra-high vacuum chamber with base pressure of 10^{-10} mbar. An incident He I radiation of energy 21.2 eV (SPECS UVS 10/35) served as an excitation source. The calibration was done by measuring first the Fermi level of a gold reference sample. The kinetic energy spectra were detected using a Combined Lens and Analyzer Module (CLAM) analyzer from Thermo VG.

3.4. Structural and optical properties of In_2S_3 layers

3.4.1. Phase analysis by X-ray diffraction

The crystal structure of thin films can be investigated by x-ray diffraction. Atoms in a crystal are arranged in a regular manner. If a beam of x-rays 1, 2, 3 is incident on a crystal at an angle θ, the rays will be scattered into 1', 2', 3' as illustrated in figure 3.16. The scattered rays will interfere depending on the phase relationship between the incident and scattered rays [127, 128].

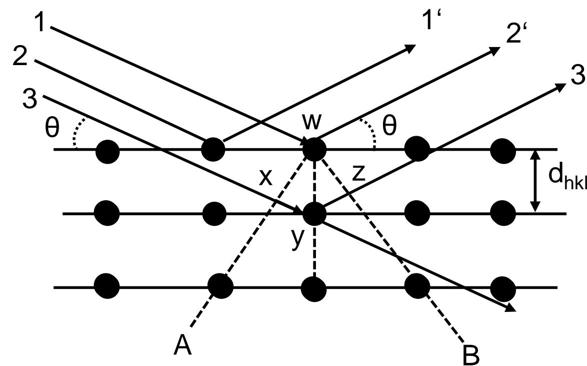

Figure 3.16: Schematic of diffraction of x-rays by a crystal

If the incident rays are in phase on a plane A and the scattered rays are in phase on a plane B, then interference will be constructive if the phase difference is an integer multiple of the wavelength (λ) of the incident x-rays. This relationship is expressed mathematically by Bragg's diffraction law as $n\lambda = 2d_{hkl}sin\theta$ where d is inter planar distance in a family of planes with miller indices hkl and θ is the Bragg angle at which constructive interference occurs. Diffraction can only occur if $d \geq \lambda/2$ [127].

By measuring the x-ray diffraction spectrum, the Miller indices can be identified using various software and inter planar spacing can be calculated. The size of crystallites (t) in a sample can be estimated from measured diffraction peak profiles using the Debye-Scherrer's equation [128].

$$t = \frac{0.9 \cdot \lambda}{\beta \cdot cos\theta} \qquad (3.21)$$

The width of the diffraction peak β is determined at full width half maximum of the peak's intensity, where λ is the wavelength of the incident radiation.

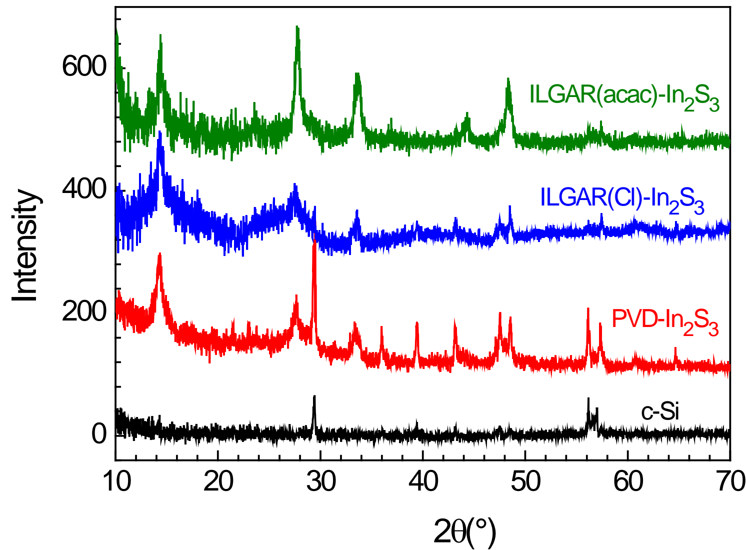

Figure 3.17: X-ray diffraction spectra for PVD-In_2S_3, ILGAR(CL) -In_2S_3 and ILGAR(acac) -In_2S_3 layers to compared to that for crystalline silicon.

Figure 3.17 shows x-ray diffraction patterns for three different In_2S_3 layers together with that of c-Si substrate. The x-ray diffraction spectra were obtained using Brucker D8 Advance diffractometer equipped with a CuKα radiation source. The measurements were performed at grazing incidence of 0.9° with incident wavelength of 0.15406 nm. The sizes of the crystallites were calculated using the Debye-Scherrer equation 3.21 and amounted to 10.0 nm, 11.0 nm and 11.6 nm for ILGAR(Cl)-In_2S_3, ILGAR(acac)-In_2S_3 and PVD-In_2S_3. The crystallite sizes for all the layers were comparable.

3.4.2. Morphology and thickness analysis of In_2S_3 layers

The morphology of semiconductor thin films and devices can be investigated by imaging with scanning electron microscopes (SEM). An electron gun generates a beam of electrons which is collimated onto a sample. The interaction of the beam with the sample results in emission of signals such as auger electrons, backscattered electrons, x-rays or secondary electrons, which can be analyzed to extract information about the

sample [129]. Low energy secondary electrons scattered from the surface of the sample are detected and analyzed to give an image of the surface.

Figure 3.18 shows the interaction of the incident electron beam with a sample. Repeated collisions between the electrons and sample atoms create an interaction volume below the sample surface. The resolution of the SEM is controlled by the size of the interaction volume. The sampling depth for SEM is 10 to 100nm. Sample imaging was performed using Zeiss LEO 1530 Gemini SEM equipped with In-Lens detector. The samples were tilted at an angle of 30° for cross sectional measurements.

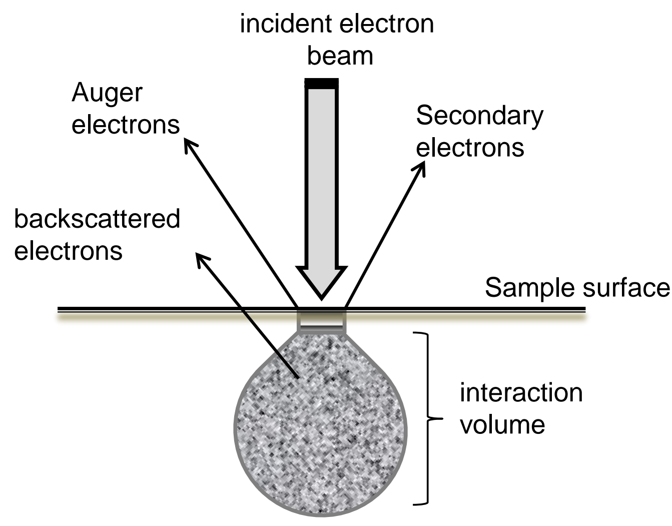

Figure 3.18: Interaction of electron beam with a sample in SEM measurements

The thickness of the samples was determined using Veeco - Dektak 8 stylus profilometer. A section of the sample was scratched on the surface up to the substrate. The stylus was scanned across the scratched region. An example of the scan profile is given in figure 3.19. The vertical distance between the substrate and the sample surface gives the thickness (d) of the sample. Information about the surface roughness was obtained by scanning some distance on the sample surface. The average roughness was calculated from the scanned profile. The Veeco Dektak profilometer takes 300 samples per second. The horizontal resolution defined as the scan length/(scan duration x 300).

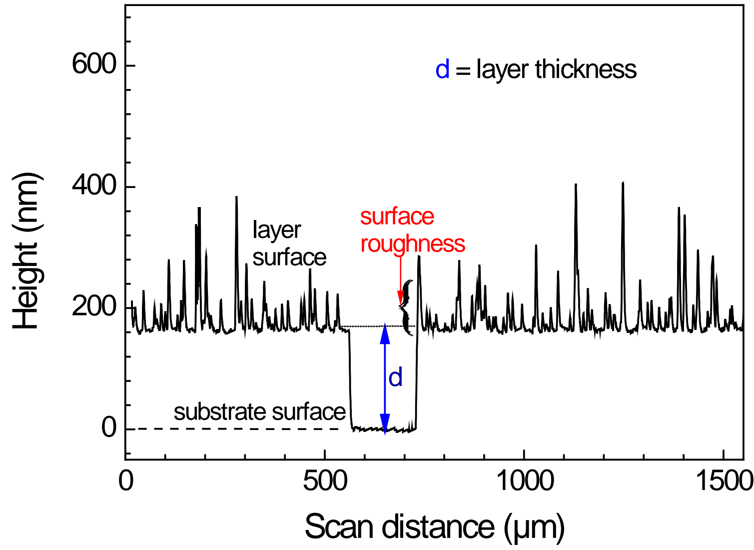

Figure 3.19: Scan plot of a rough layer taken with Dektak step profilometer to determine the thickness (*d*).

3.4.3. Optical characterization of In_2S_3 thin films

Photon-assisted electronic transitions in semiconductors can occur between different energy bands, which contain information about the band gap. When light passes through a semiconductor, some of the light is absorbed and electron-hole pairs are generated and the intensity of the light reduces with distance [130]. For a layer of thickness d, the transmitted light is expressed as

$$T = (1 - R)exp(-\alpha d) \tag{3.22}$$

R is the reflectance at the top surface at normal incidence,

$$R = \frac{(1-n)^2 + k^2}{(1+n)^2 + k^2}. \tag{3.23}$$

In the case that light scattering can be neglected, the absorption coefficient can be determined directly from measured R and T spectra using equation 3.23.

Near the absorption edge, the absorption coefficient is given by

$$\alpha \propto \left(hv - E_g\right)^m \tag{3.24}$$

where hv is photon energy and m is a constant that determines the nature of the band gap [130].

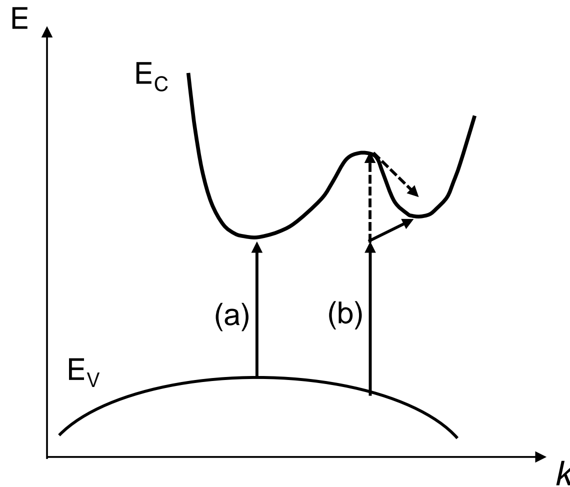

Figure 3.20: Optical transitions in a semiconductor (a) direct transition and (b) indirect transition involving phonon emission or absorption.

For allowed or forbidden direct band gap materials, $m = 1/2$ or $3/2$. Direct optical transitions are shown in figure 3.20 (a). Allowed transitions can occur at all k values but forbidden transitions can only occur at $k \neq 0$. For indirect transitions electron excitation is accompanied by absorption or release of phonons in order conserve the momentum as illustrated in figure 3.20 (b). Phonons of energy E_p are either absorbed or emitted and absorption coefficient is expressed as

$$\alpha \propto \left(hv - E_g \pm E_p\right)^m \quad (3.25)$$

m = 2 or 3 for allowed or forbidden transitions, respectively.

Transmittance and reflectance measurement were performed using Perkin Lambda 35 UV-vis spectrophotometer equipped with an integrating sphere. The absorption coefficient and hence optical band gap of In_2S_3 layers were obtained from the transmission and reflection data using the above approach.

4. Copper diffusion in In_2S_3 layers

Incorporation of Cu (I) into the structure of In_2S_3 is crucial to the properties and applications of In_2S_3 thin films. To control Cu diffusion requires knowledge of diffusion coefficients and their temperature dependence. Results of Cu diffusion from CuSCN source layers into different In_2S_3 layers are presented in this chapter. Some of the results were published in [39]. Diffusion parameters were calculated from Cu depth profiles obtained from RBS measurements. The first part of this chapter reports the distribution of diffused Cu in In_2S_3 layers. The second part contains the analysis of the results. A discussion of possible diffusion mechanisms of Cu migration in In_2S_3 with emphasis on the role of residual Cl is presented at the end of the chapter.

4.1. Copper distribution in In_2S_3 layers

4.1.1. Cu diffusion in thermally evaporated In_2S_3 layers

Figure 4.1 (a) and (b) shows SEM micrographs of as-deposited c-Si/PVD-In_2S_3/CuSCN and c-Si/PVD-In_2S_3:Cu after annealing and etching away CuSCN in pyridine solution, respectively. The CuSCN layer was relatively thick compared to PVD-In_2S_3 layer and served as an infinite source of Cu for diffusion. CuSCN was completely removed by etching in pyridine solution. The surface roughness was measured by scanning the sample surface using Dektak step profiler. The surface profiles of c-Si/PVD-In_2S_3:Cu layers after annealing and removal of CuSCN are shown in figure 4.1 (c). The surface roughness increased with increasing annealing temperature. The average roughness amounted to 2.8, 8.4, 14.7 and 22.8 nm PVD-In_2S_3:Cu without and after annealing for 5 min at temperatures of 200, 225 and 250°C and removing CuSCN, respectively. The

change in surface roughness could be associated with a change in surface morphology and / or crystallinity during annealing.

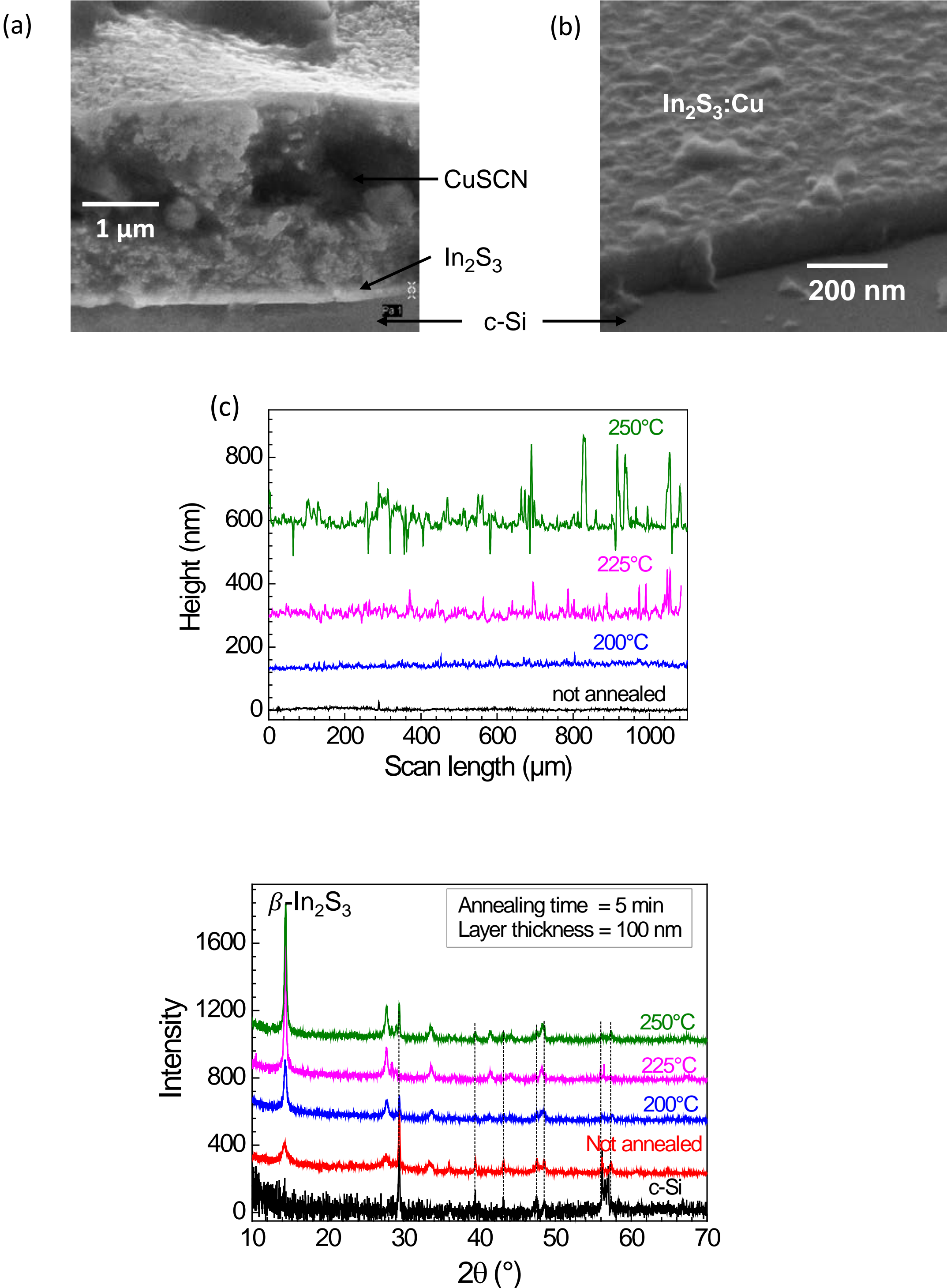

Figure 4.1: SEM micrograph (tilted at 30°) of c-Si/PVD-In_2S_3/CuSCN (a) and c-Si/PVD-In_2S_3:Cu (b) before and after etching away CuSCN, respectively. The surface scan with dektak profilometer (c) and XRD specta (d) of PVD-In_2S_3:Cu after etching away CuSCN.

The crystal structure of PVD-In_2S_3:Cu after diffusion and removal of CuSCN was investigated using x-ray diffraction (XRD). The XRD spectra are shown in figure 4.1 (d). The diffraction peaks from bare c-Si substrate are also shown in the figure for comparison. The peak at 2θ= 14.38° was assigned to β-In_2S_3 and increased in height with increasing annealing temperature. The size of the crystallites was calculated using the Debye-Scherrer equation. The average diameter of the crystallites amounted to 11.6 nm before annealing and 20.1, 28.2 and 30.2 nm after annealing at 200, 225 and 250°C, respectively. This means together with the increase of the amplitude, the crystallinity of the PVD-In_2S_3 layers improved with increasing annealing temperature. Diffusion of Cu in PVD-In_2S_3 was therefore accompanied by some structural changes in the host layer. As a remark, the strong structural changes occurred after annealing at temperatures ≥225°C.

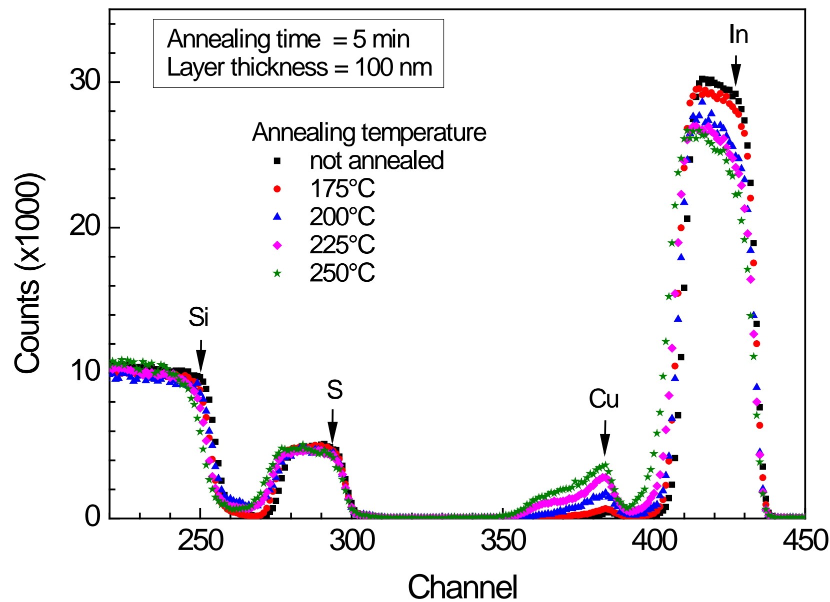

Figure 4.2: RBS spectra of c-Si/PVD-In_2S_3:Cu after diffusion without annealing and after annealing at 175, 200, 225 and 250°C and removal of CuSCN.

RBS measurements were performed on c-Si/PVD-In_2S_3:Cu samples after annealing for 5 min at temperatures between 150 and 250°C and removal of CuSCN. The measured RBS spectra are given in figure 4.2. The thickness of the PVD-In_2S_3 layer was about

100 nm. The signals corresponding to In, Cu, S and Si elements detected in the target samples are labeled. The position of each signal in the spectrum depends on the atomic mass of the detected elements. Signals from elements with relatively heavier atoms appear at larger channel numbers. The signal from In appears at highest channel numbers followed by Cu, S and then Si in the order of decreasing atomic masses. The width of the signals contains information about the thickness of the sample.

The RBS signals related to In and S tended to increase in width with increasing annealing temperature. This was a result of an increase in the effective volume of the In_2S_3 layer due to enhanced amounts of diffused Cu. The RBS signal related to Cu increased in amplitude with increasing annealing temperature. The shape of the signals related to Cu showed non-uniform distribution of Cu in PVD-In_2S_3:Cu. This denotes a concentration gradient in Cu distribution with depth.

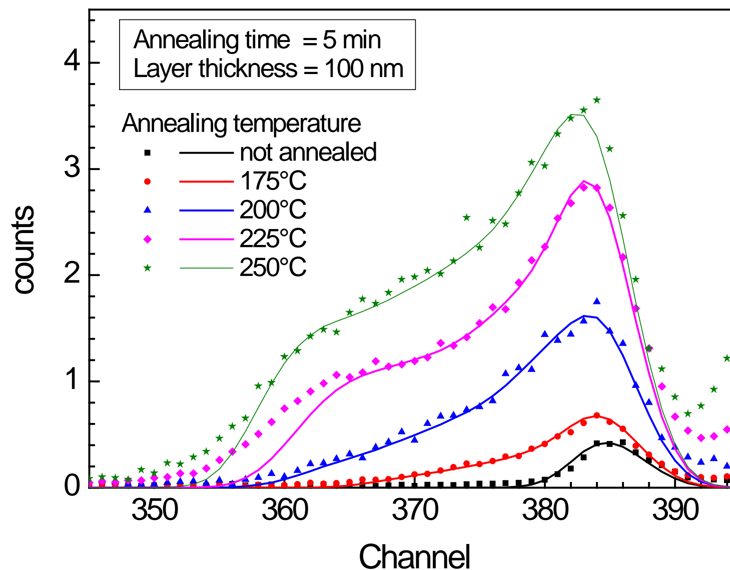

Figure 4.3: Region of the RBS spectra with signals from Cu after diffusion without annealing and after annealing at 175, 200, 225 and 250°C temperatures and removal of CuSCN.

Figure 4.3 shows the region of the RBS signals related to Cu before and after annealing at 175, 200, 225 and 250°C temperatures and removal of CuSCN. There was a systematic increase in the signal height with annealing temperature. The signals from Cu between channel numbers 380 and 390 represent a high concentration at the surface.

The decrease in the signal height with decreasing channel numbers signifies a gradient in the concentration of Cu with depth. Surface roughness leads to broadening of the RBS signal and increased yield at the lower energy or channel number part [131]. This effect can be seen as a deviation of the measured from the simulated spectra in figure 4.3 for the RBS signal related to Cu. The influence of roughness was not taken into account in the analysis of the RBS data.

Depth profiles of the Cu distribution in PVD-In_2S_3:Cu after annealing at 175, 200, 225 and 250°C temperatures and removal of CuSCN are shown in figure 4.4. There was a thin surface layer of about 10 nm whose concentration of Cu was independent of annealing temperature. For the not annealed sample (not shown in the graph), there was only the surface layer with increased Cu concentration. Copper did not penetrate through the entire PVD-In_2S_3 layer for annealing temperatures below 200°C.

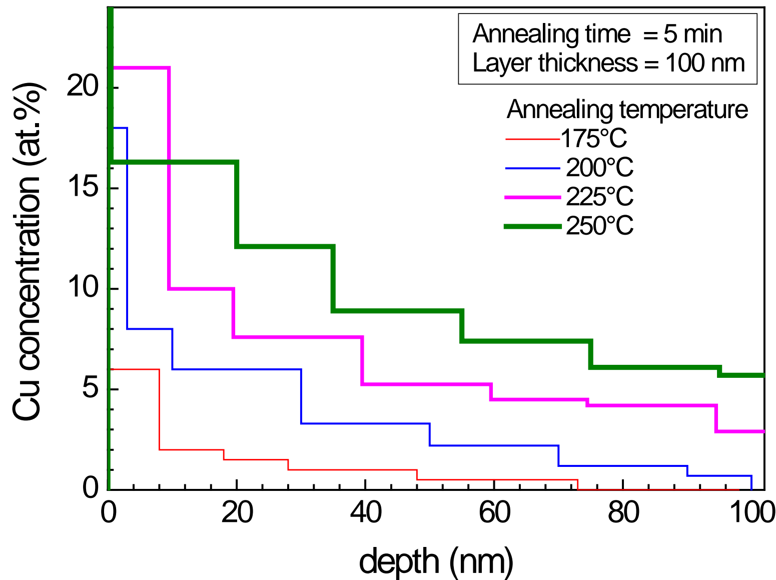

Figure 4.4: Cu depth profiles obtained by simulating RBS spectra after diffusion without annealing and after annealing for 5 min at 175, 200, 225 and 250°C and removal of CuSCN.

The integrated amounts of each detected element in the PVD-In_2S_3:Cu layers were calculated from the RBS spectra and from the depth profiles. The Cu signals from RBS spectra of PVD-In_2S_3:Cu were integrated and used to calculate the areal densities of each element as described in section 3.2.2 The areal densities (*Nt*) were divided by the

layer thickness to get the atomic densities in cm^{-3}. The atomic density of each element was divided by the atomic density of PVD-In_2S_3 to obtain the concentration of each element in at. %. The integrated concentrations of In, S and Cu in PVD-In_2S_3 are plotted in figure 4.5. The integrated amounts of In and S were almost unchanged while the amount of Cu increased with annealing temperature. There was no loss of either In or S during the diffusion experiments. The amount of Cu increased by two orders of magnitude when annealing temperature was increased from 150 °C (0.01 at.%) to 175 °C (1.0 at.%). The diffusion of Cu into In_2S_3 was limited at temperatures below 175 °C. The barrier/limiting parameter is overcome when the annealing temperature is increased to 175 °C.

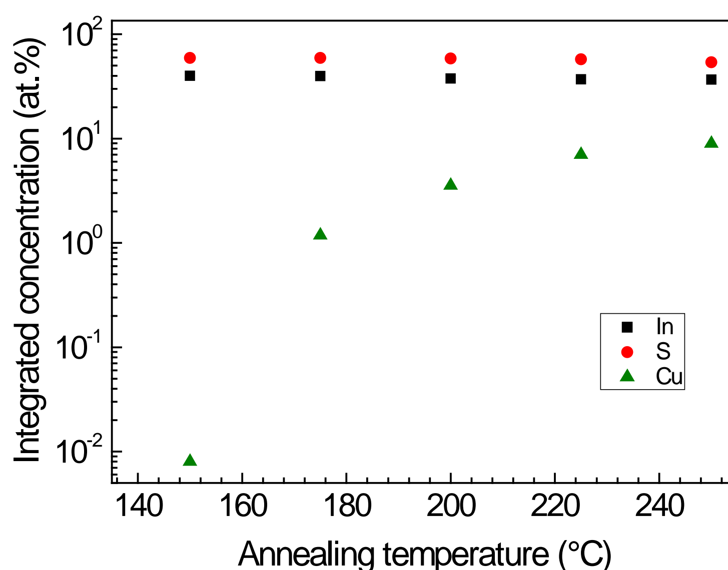

Figure 4.5: Integrated amounts of In, S and Cu in PVD-In_2S_3:Cu.

4.1.2. Cu diffusion in In_2S_3 layers deposited from $In(acac)_3$ precursor

Figure 4.6 shows a SEM micrograph of ILGAR(acac)-In_2S_3:Cu after annealing and etching away CuSCN in pyridine solution (a), surface profiles (b) and XRD spectra (c) before and after annealing at 200 and 250°C temperatures in comparison to c-Si substrate and not annealed ILGAR(acac)-In_2S_3:Cu. Figure 4.6 (a) shows that CuSCN was completely removed by pyridine during etching. The crystallites of In_2S_3:Cu could

be seen in the SEM micrograph. The step profile scans showed an increase in the surface roughness after annealing of c-Si/ILGAR(acac)-In_2S_3/CuSCN and etching away CuSCN. Furthermore, the average roughness increased from 16 nm for bare ILGAR(acac)-In_2S_3 to 19, 31 and 50 nm for ILGAR(acac)-In_2S_3:Cu before and after annealing for 5 min at 200 and 250 °C and removal of CuSCN, respectively. The average roughness for the not annealed ILGAR(acac)-In_2S_3 was larger than that of the not annealed PVD-In_2S_3 layer.

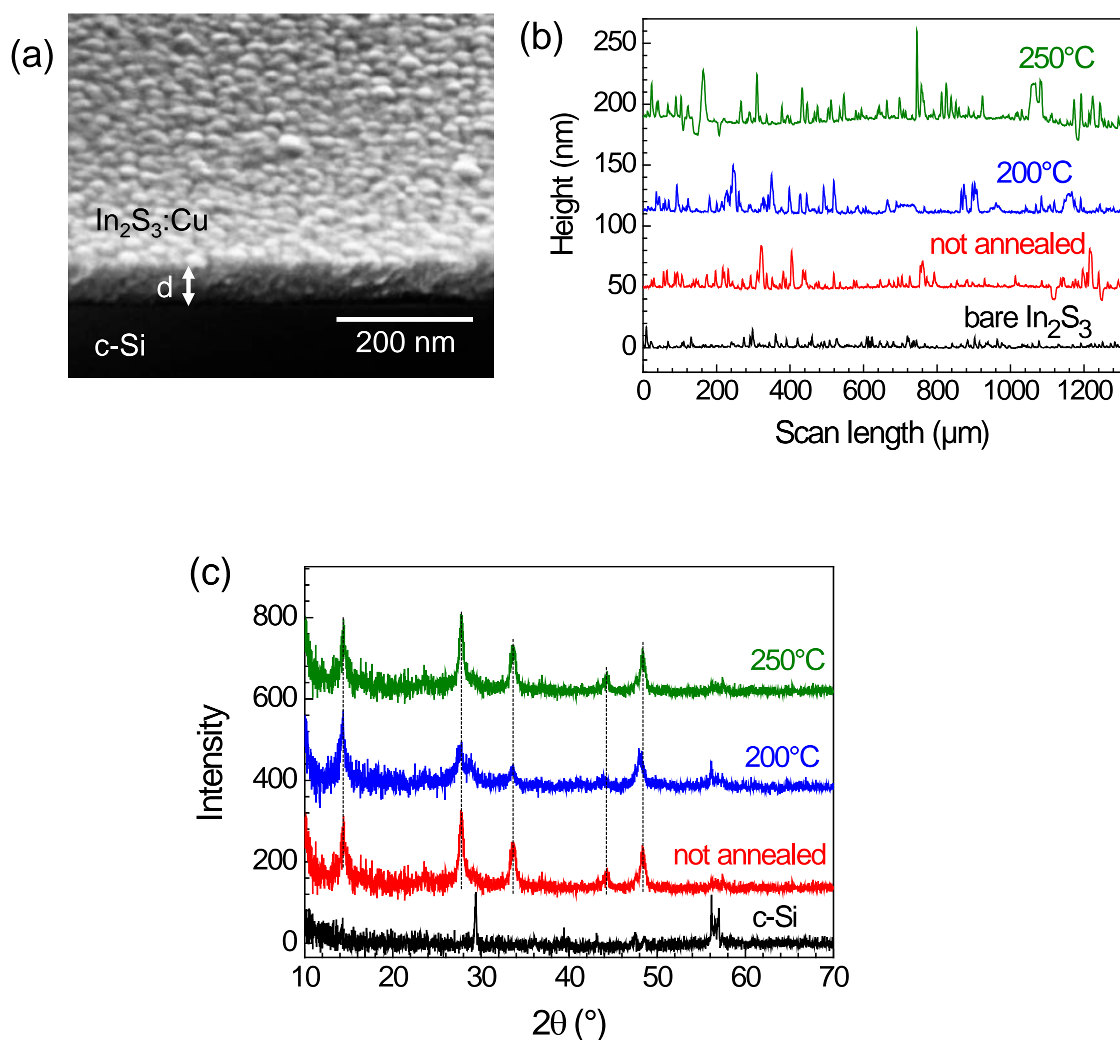

Figure 4.6: SEM micrograph of ILGAR(acac)-In_2S_3:Cu after annealing and removal of CuSCN (a), step profiles (b) and XRD spectra of ILGAR(acac)-In_2S_3:Cu after annealing at 200 and 250°C temperatures and removal of CuSCN.

The XRD spectra in figure 4.6 (c) do not show differences in the diffraction peaks and intensities. The point is that ILGAR(acac)-In_2S_3 layers were deposited at substrate

temperature of 200°C. At this temperature, the deposited layers were almost polycrystalline. The crystallite sizes were 10, 12 and 13 nm in size for as-deposited ILGAR(acac)-In_2S_3 and ILGAR(acac)-In_2S_3:Cu after annealing temperatures of 200 and 250°C, respectively. No significant change in the crystallinity was observed after annealing at temperatures up to 250°C.

RBS spectra of c-Si/ILGAR(acac)-In_2S_3:Cu after annealing and removal of CuSCN are shown in figure 4.7. The signals from In, Cu, S and Si are indicated. The In and S signals decreased in height but increased slightly in width for higher annealing temperatures. The introduction of diffused Cu into ILGAR(acac)-In_2S_3 layers increased the effective volume of the layer and hence the change in signal width. The amplitude of the signal from Cu increased with increasing annealing temperature due to enhanced diffusion.

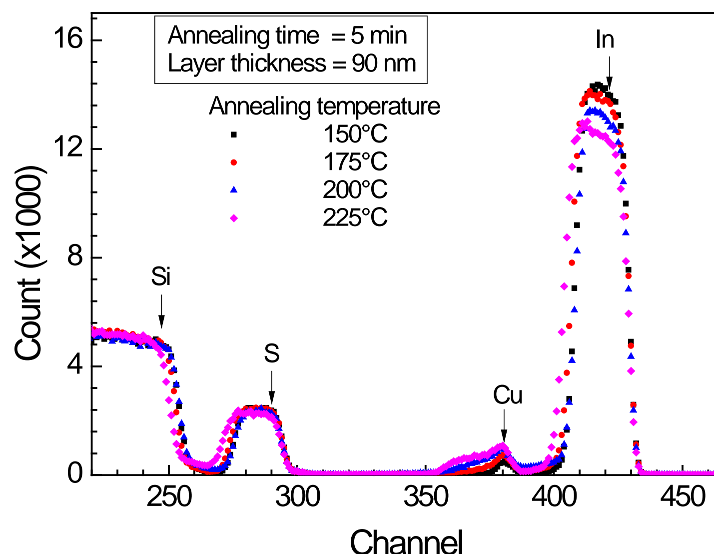

Figure 4.7: RBS spectra of c-Si / ILGAR(acac)-In_2S_3:Cu after annealing at 150, 175, 200, and 225 °C temperatures and removal of CuSCN.

The region of the RBS spectra showing the signal from Cu as detected in c-Si/ILGAR(acac)-In_2S_3:Cu is shown in figure 4.8. There was a systematic increase of the Cu signal height with increasing annealing temperature. The Cu signal between channel numbers 380 and 390 denotes a high Cu concentration at the surface of

ILGAR(acac)-In_2S_3:Cu. The decrease in the signal amplitude with decreasing channel numbers indicates a decrease of the Cu concentration in the gradients with depth.

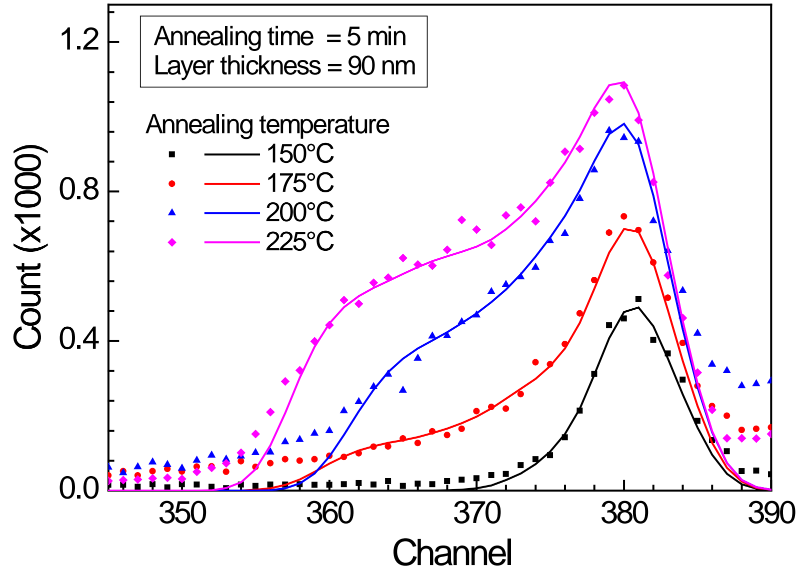

Figure 4.8: Region of RBS spectra with signals from Cu after annealing c-Si / ILGAR(acac)-In_2S_3 / CuSCN for 5 min at 150, 175, 200, and 225°C temperatures and removal of CuSCN.

The depth profiles were obtained by simulating the measured spectra and comparing simulated and measured spectra to get the best fits. Figure 4.9 shows depth profiles for Cu distribution in ILGAR(acac)-In_2S_3:Cu layers after annealing for 5 min at temperatures of 150, 175, 200 and 225°C and removal of CuSCN.

Diffused Cu did not penetrate the entire ILGAR(acac)-In_2S_3 layer upto the internal interface after annealing for 150°C. Copper reached the back of ILGAR(acac)-In_2S_3 layer after annealing at temperatures of 175°C or higher. The thin surface layer with high Cu concentration was about 10 nm thick independent of annealing temperature. This means that an interfacial layer with high Cu concentration was formed after deposition of CuSCN on to ILGAR(acac)-In_2S_3 and annealing. In different experiments, the formation of In_2S_3:Cu interfacial layer was observed by transmission electron microscopy (TEM) [23, 42] and photoelectron spectroscopy (PES) [26] for CIGSe/In_2S_3 interfaces after annealing at temperatures of 200°C or higher.

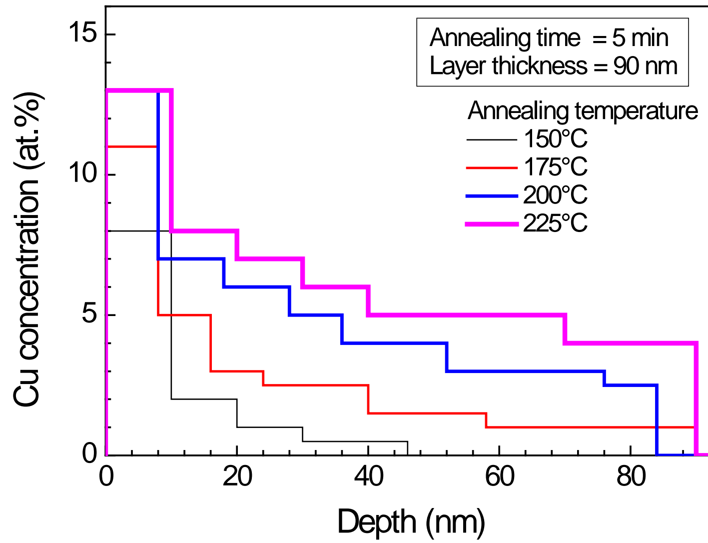

Figure 4.9: Cu depth profiles obtained by simulation of RBS spectra after annealing c-Si / ILGAR(acac)-In_2S_3 / CuSCN for 5 min at 150, 175, 200 and 225°C temperatures and removal of CuSCN

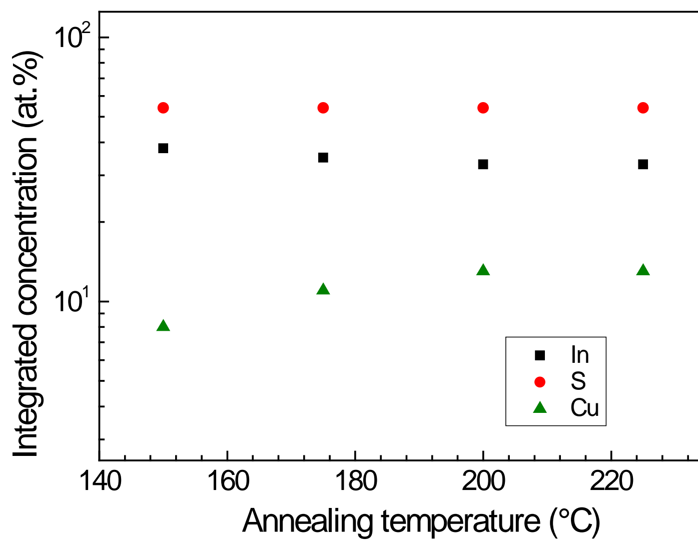

Figure 4.10: Integrated amounts of In, S, and Cu in ILGAR(acac)-In_2S_3:Cu.

The integrated amounts of In, S and diffused Cu in ILGAR(acac)-In_2S_3:Cu layers after annealing for 5 min at 150, 175, 200 and 225°C and removal of CuSCN are given in figure 4.10. The integrated amount of Cu increased with annealing temperature as expected due to enhanced diffusion at higher temperatures. As a remark, there was no

sharp increase in the amount of integrated Cu when the annealing temperature was increased from 150 to 175 °C as was observed for IILGAR(Cl)-In_2S_3 layer. The amount of In and S stayed constant. This means that diffusion of Cu was not accompanied by loss of either In or S, for example after etching of CuSCN.

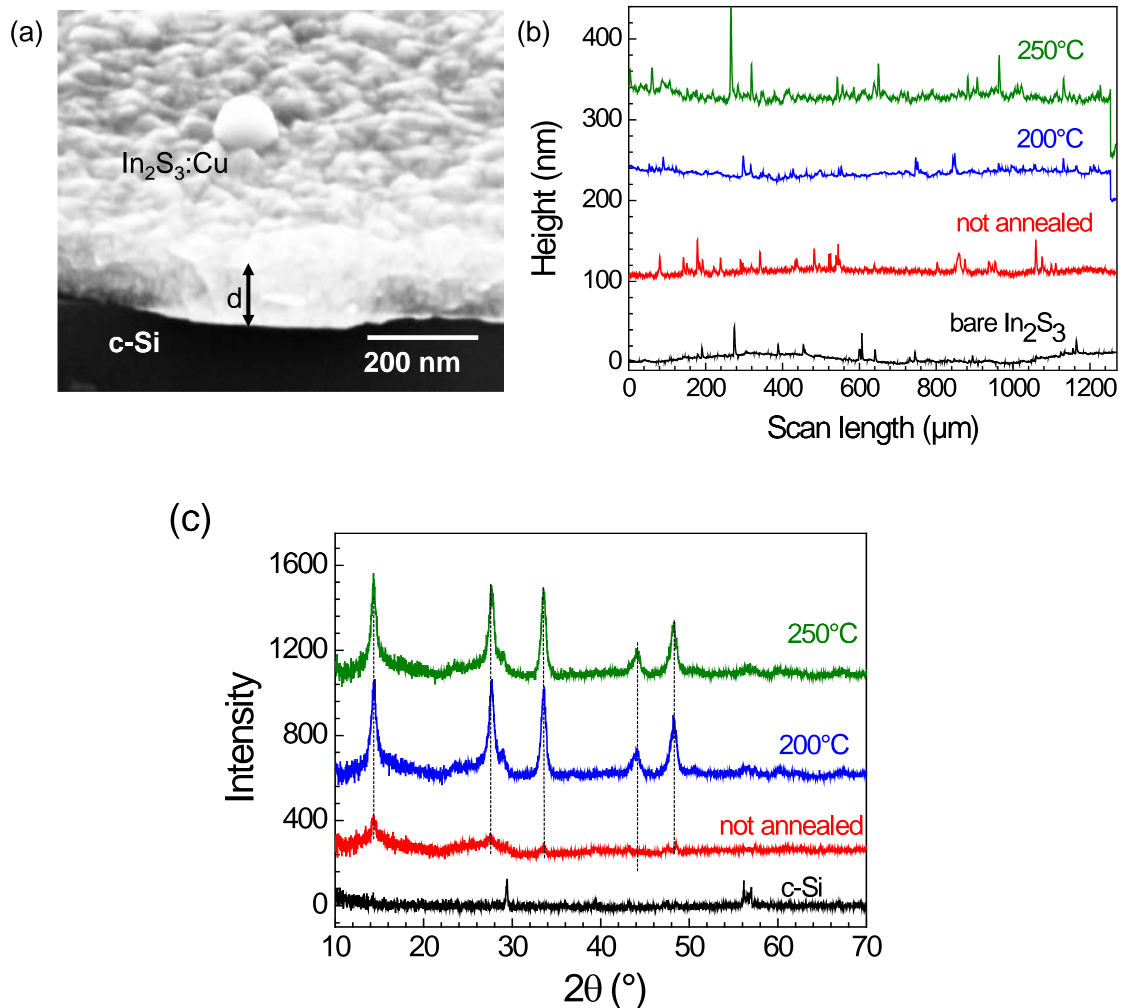

Figure 4.11: SEM micrograph of ILGAR(Cl)-In_2S_3:Cu (a), step profiles (b) and XRD spectra (c) of ILGAR(acac)-In_2S_3:Cu before and after annealing at 200 and 250 °C and removal of CuSCN.

4.1.3. Cu diffusion in In_2S_3 layers deposited from $InCl_3$ precursor

Figure 4.11 shows a SEM micrograph, step profiles and XRD spectra of ILGAR(Cl)-In_2S_3:Cu after annealing c-Si/ILGAR(Cl)-In_2S_3/CuSCN for 5 min and etching away CuSCN. CuSCN was completely removed during etching. The scan profiles showed an increase in the surface roughness with increasing annealing temperature. The average roughness was a little higher than for c-Si/ILGAR(acac)-In_2S_3 and amounted to 17, 21, 43 and 66 nm for bare ILGAR(Cl)-In_2S_3, ILGAR(Cl)-In_2S_3:Cu after removal of CuSCN without annealing and after annealing for 200 and 250°C, respectively.

The size of the crystallites was calculated using the Debye-Scherrer equation and amounted to 10, 11 and 12 nm for ILGAR(Cl)-In_2S_3:Cu after removal of CuSCN without and after annealing at 200 and 250°C, respectively. The crystallites were almost the same sizes as those for ILGAR(acac)-In_2S_3 layers. ILGAR(Cl)-In_2S_3 layers were deposited at 200°C and diffusion experiments were performed in the temperature range of 150 to 250°C. The crystallinity of ILGAR(Cl)-In_2S_3 layers barely changed after annealing up to 250°C. There were no new Cu-In-S phases observed from the XRD analysis. The amount of diffused Cu was below the solid solution limit for the formation of new phases.

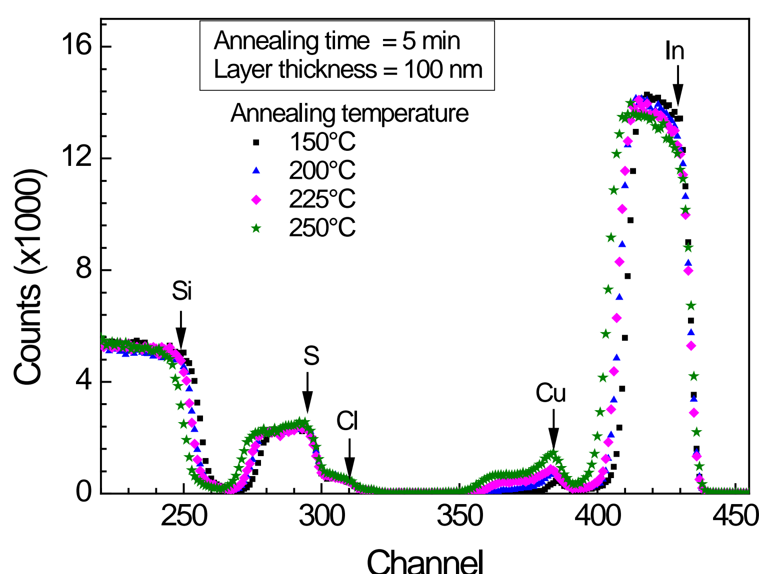

Figure 4.12: RBS spectra of ILGAR(Cl)-In_2S_3:Cu after annealing for 5 min at temperatures of 150, 200, 225 and 250°C and removal of CuSCN

The RBS spectra of ILGAR(Cl)-In_2S_3:Cu after annealing for 5 min at 150, 200, 225 and 250°C temperatures and removal of CuSCN are shown in figure 4.12. The thickness of the ILGAR(Cl)-In_2S_3 layer was about 100 nm. The signals from In, Cu, Cl, S and Si are indicated in the graph. The signal from Cu showed non-uniform distribution through ILGAR(Cl)-In_2S_3:Cu bulk. The signals from Cl and S overlapped because the difference between their atomic masses is much smaller than the mass resolution of the measurement.

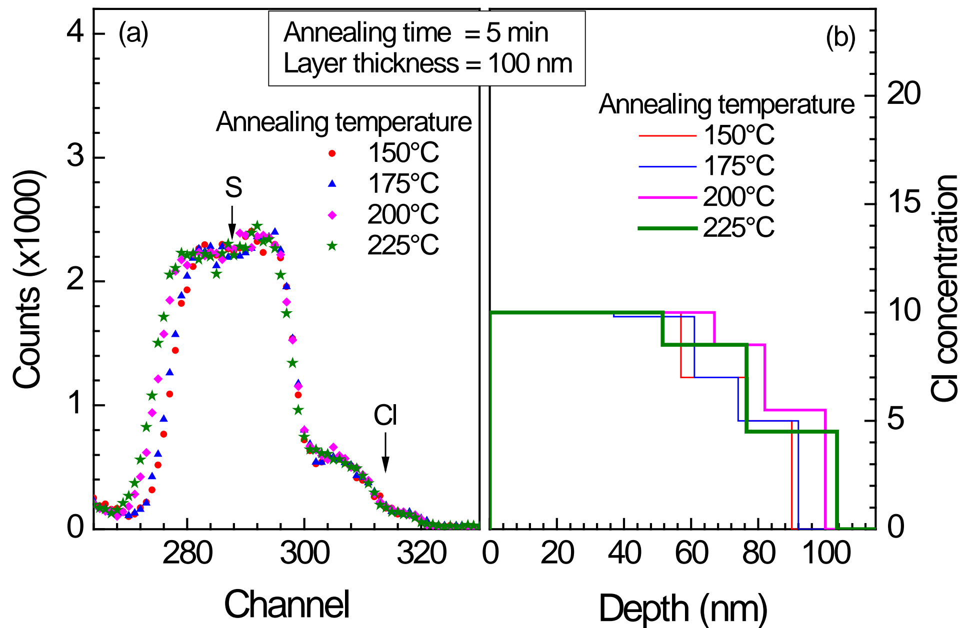

Figure 4.13: Region of RBS spectra with signals from Cl and S (a) and depth profiles of Cl in ILGAR(Cl)-In_2S_3:Cu after annealing at 150, 175, 200, and 225°C temperatures and removal of CuSCN.

Figure 4.13 shows the signals from S and Cl and depth profiles of Cl after annealing for 5 min at 175, 200 and 225°C temperatures and removal of CuSCN. It was found that the distribution of Cl in ILGAR(Cl)-In_2S_3 was not uniform but decreased with depth from the top. ILGAR is a sequential process involving spray and sulfurization steps with pauses in between. As more cycles are deposited, the already deposited layer is exposed

to repeated sulfurization cycles. This way the first layers to be deposited experience many sulfurization steps and the Cl content decreases. As more and more solution is atomized and sprayed, the remaining solution in the glass container become more concentrated. This means that additional cycles will deposit precursor layers that are more concentrated than the first layers.

The region of the RBS spectra of ILGAR(Cl)-In_2S_3:Cu with signals from Cu after annealing for 5 min at 150, 175, 200, 225 and 250°C are shown in figure 4.14. The signal in the region between channels 380 and 390 depicts the presence of a thin surface layer with relatively high Cu concentration. The change in the signal towards lower channel numbers signifies a concentration gradient with decreasing Cu content with depth.

Depth profiles were extracted after simulation of the RBS spectra for the different annealing temperatures. This was done for ILGAR(Cl)-In_2S_3 with varying Cl content. Different Cl contents were achieved by varying the deposition process parameters as shown in table 4.1. The time durations of the deposition cycles were varied as illustrated in figure 3.2.

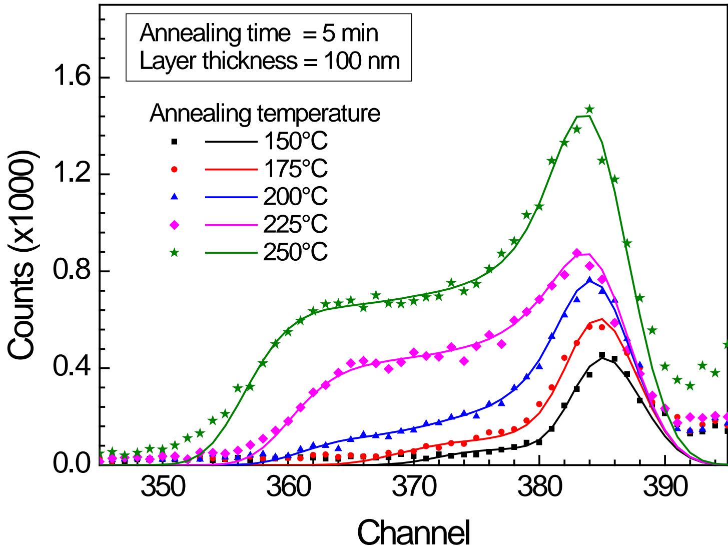

Figure 4.14: Region of RBS spectra with signals from Cu after annealing ILGAR(Cl)-In_2S_3/CuSCN for 5 min at 150, 175, 200, 225 and 250°C temperatures and removal of CuSCN.

The differences in layer thicknesses given in table 4.1 are caused by differences in the deposition rates concomitant with the changes in the deposition parameters. The flow rate of 100% H_2S was maintained at 0.0375 lpm for deposition of all the samples. For sample E, a background flow of 5% H_2S was maintained during deposition. The samples were labeled by letters A, B, C, D and E corresponding to ILGAR(acac)-In_2S_3 (A), ILGAR(Cl)-In_2S_3 with residual Cl content of 7.8, 8.5, 11.3 and 13.8 at.%, respectively.

Table 4.1: Experimental parameters for deposition of ILGAR(Cl)-In_2S_3 layers with varied Cl concentrations. The parameters Δt_i $(i = 1,2,3,4)$ correspond to precursor spray, pause, sulfurization and pause, respectively. The layer thicknesses (*d*) and Cl content as obtained from RBS analysis are shown. Sample was ILGAR(acac)-In_2S_3 while samples B, C, D and E were ILGAR(Cl)-In_2S_3.

sample	Δt_1	Δt_2	Δt_3	Δt_4	H_2S 100%	H_2S 5%	cycles	d (nm)	Cl (at.%)
A	60	10	20	10	0.0375 lpm	-	20	90	0
B	60	10	60	10	0.0375 lpm	-	20	65	7.8
C	40	10	20	10	0.0375 lpm	-	25	100	8.5
D	60	10	20	30	0.0375 lpm	-	20	150	11.3
E	60	10	20	30	0.0375 lpm	0.95 lpm	20	65	13.8

The depth profiles of Cu distribution in ILGAR(Cl)-In_2S_3:Cu with different Cl content after annealing for 5 min at 150, 200, 225 and 250°C temperatures and removal of CuSCN are given in figure 4.15. The Cl concentrations were (a) 7.8, (b) 8.5, (c) 11.3 and (d) 13.8 at. %. In all cases, there was a thin surface layer of about 10 nm thick with relatively high Cu concentration. The concentration of Cu and thickness of the surface layer was independent of Cl content and annealing temperature.

The quality of the Cu depth profiles was similar for all the Cl concentrations. Cu diffused through the entire ILGAR(Cl)-In_2S_3 layers after annealing for temperatures of

200°C or higher. After annealing for 5 min at 150°C diffused Cu did not reach the back surface of ILGAR(Cl)-In_2S_3 layers.

Figure 4.16 shows the integrated amounts of In, S, Cl and Cu in ILGAR(Cl)-In_2S_3:Cu after annealing for 5 min at 150, 175, 200, 225 and 250°C temperatures and removal of CuSCN. The concentrations [In], [S], [Cl] and [Cu] were calculated from the integral of the respective signal from the RBS spectra and from the depth profiles. The integrated amounts of In, S and Cl remained constant independent of annealing temperature and Cl concentration. The integrated amount of Cu increased with increasing annealing temperature independent of the Cl amount. This increase was due to enhanced diffusion of Cu at higher annealing temperatures.

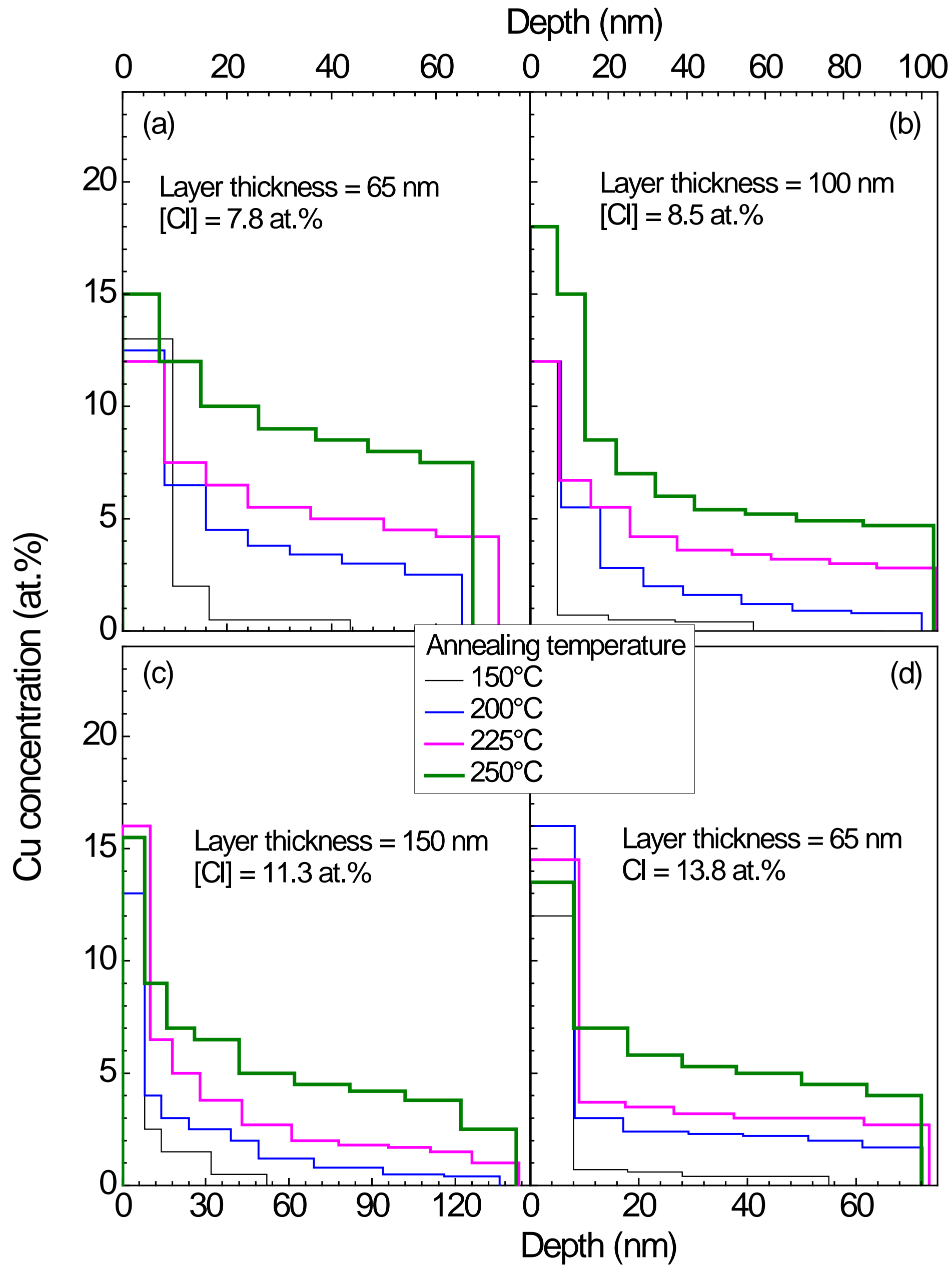

Figure 4.15: Cu depth profiles obtained by simulation of RBS spectra of ILGAR(Cl)-In_2S_3:Cu after annealing for 5 min at 150, 200, 225 and 250°C temperatures and removal of CuSCN. The values of [Cl] were 7.8 at.%, (b) 8.5 at.%, (c) 11.3at.% and 13.8 at.%. Corresponding layer thicknesses are indicated.

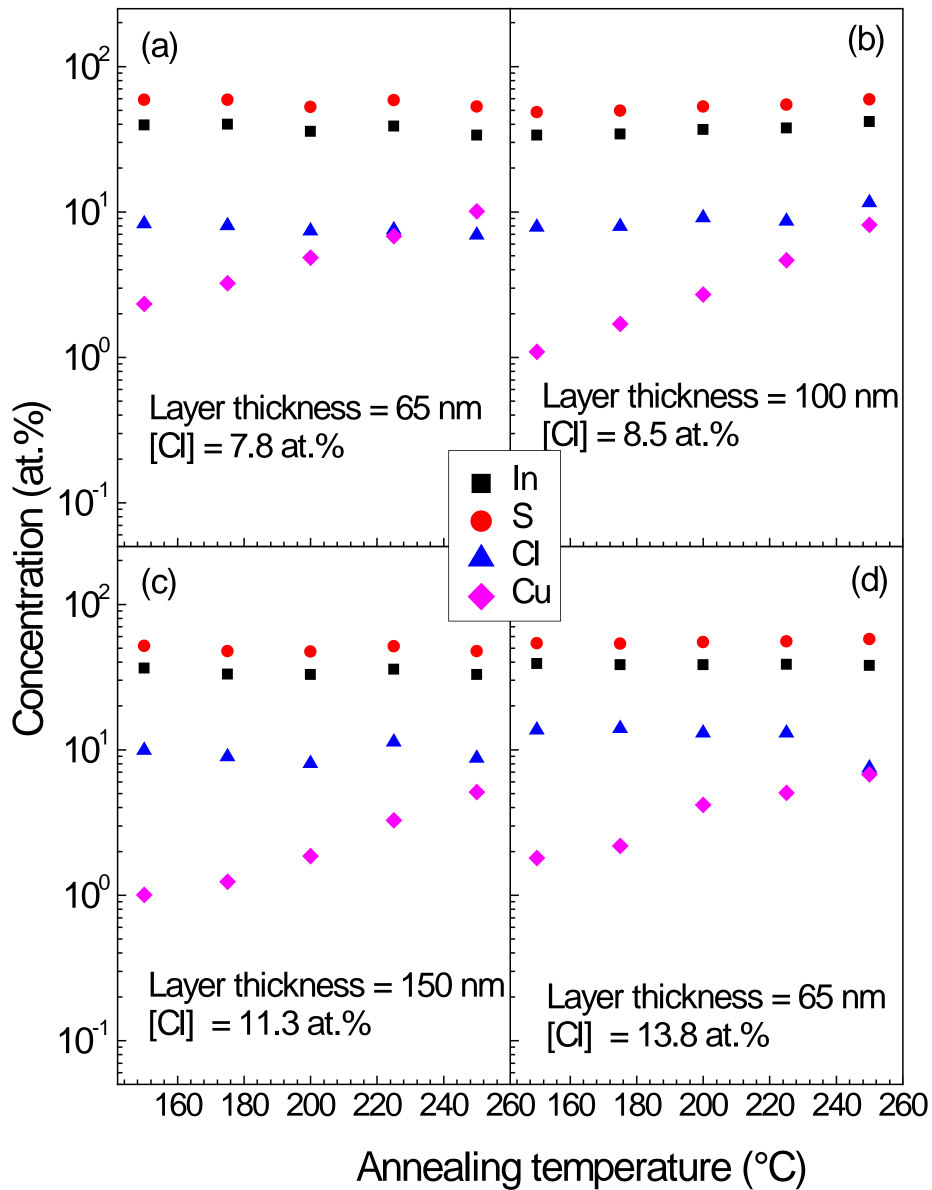

Figure 4.16: Integrated amounts of In, S, Cl and Cu in ILGAR(Cl)-In_2S_3:Cu with Cl concentrations of 7.8 at.% (a), 8.5 at.% (b), 11.3 at.% (c) and 13.8 at.% (d) after annealing for 5 min at temperatures between 150 and 250°C and removal of CuSCN. The corresponding layer thicknesses are shown.

4.2. Diffusion coefficients and mechanisms

4.2.1. One dimensional diffusion model

The Cu depth profiles were fitted with an error function to estimate the values of the diffusion coefficients. The thick CuSCN layer served as a semi-infinite Cu source. To obtain more accurate values of the diffusion coefficient, a one dimensional diffusion model was used as illustrated in figure 4.17. A recursion expression was developed from Fick's second law of diffusion with appropriate initial and boundary conditions to numerically solve the diffusion equation. Fick's second law is expressed as

$$\frac{\partial C(x,t)}{\partial t} = D \cdot \frac{\partial^2 C(x,t)}{\partial x^2} \quad (4.1)$$

where *D* is the diffusion coefficient and *C* the concentration of the diffusing species.

The recursion equation was obtained as ,

$$C_i^j = C_i^{j-1} + D \cdot \frac{\Delta t}{\Delta x^2} \cdot \left(C_{i+1}^{j-1} - 2.C_i^{j-1} + C_{i-1}^{j-1}\right) \quad (4.2)$$

Δt and Δx denotes discretization in time and space, respectively, i and j are numbers starting from 1 of a given space and time interval, respectively. The convergence condition considered was such that $\Delta t < \Delta x^2/D$. The boundary conditions were defined by a constant source C_s at the source / In_2S_3 interface $\left(B_{S/In2S3}\right)$ and a reflecting boundary at the In_2S_3 / c-Si interface $\left(B_{In2S3/c-Si}\right)$ [39] given as,

$$B_{S/In2S3}: \quad C_1^j = C_S \quad (4.3)$$

$$B_{In2S3/c-Si}: \quad C_{imax}^j = C_{max-1}^j \quad (4.4)$$

For c-Si / ILGAR(Cl)-In_2S_3 / CuSCN layer systems a limiting value of the concentration at the $B_{In2S3/c-Si}$ boundary was implemented such that;

$$B_{In2S3/c-Si}: \quad C_{imax}^j = C_{lim}^j \quad (4.5)$$

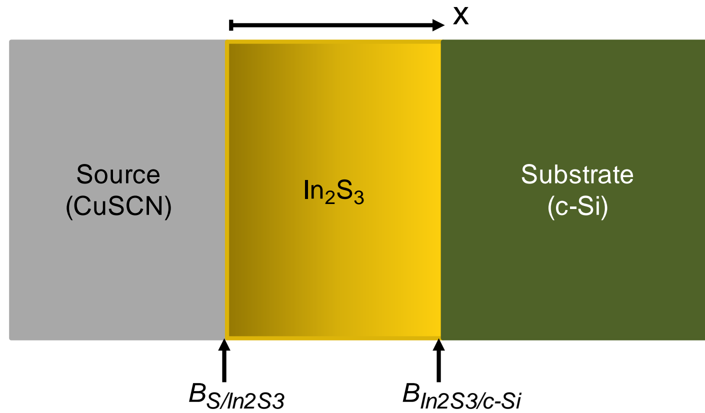

Figure 4.17: One dimensional simulation model for depth profiles.

Diffusion of Cu into c-Si starts at 300°C for mirror-polished surfaces and at 650°C for wafers with a native oxide layer on top [132, 133]. The temperature range used in this work was below 300°C where c-Si served as a reflecting boundary. The c-Si substrates were used without polishing and therefore a native oxide layer on the order of 2-3 nm was on top. Therefore c-Si was treated as a reflecting barrier for Cu diffusion in the model.

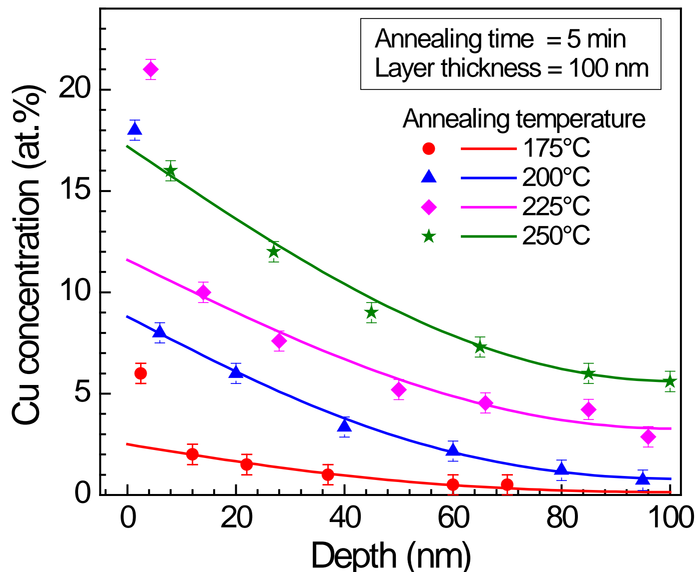

Figure 4.18: Simulated and measured Cu depth profiles for PVD-In_2S_3:Cu after annealing at 175, 200, 225 and 250°C temperatures and removal of CuSCN.

The Cu concentration profiles were simulated numerically and compared with measured data until a good agreement was reached. The simulation parameters were modified until the simulated spectra reproduced satisfactorily the measured data. The relatively high Cu concentration at the surface was independent of the host In_2S_3 layer and annealing temperature. The data points corresponding to these concentrations near the surface of In_2S_3:Cu were not included in the simulation. Diffusion coefficient values for Cu in In_2S_3 $\left(D_{Cu(In2S3)}\right)$ were obtained for the In_2S_3 layers and at each annealing temperature.

Figure 4.18 shows simulated and measured concentration profiles of Cu in PVD-In_2S_3:Cu layers after annealing for 5 min at 175, 200, 225 and 250°C temperatures and removal of CuSCN. The concentration profiles could be fitted well with one diffusion coefficient. This denotes one diffusion mechanism of Cu diffusion in PVD-In_2S_3 layers. The values of $D_{Cu(PVD)}$ amounted to $3.1 \pm 0.5 \times 10^{-14}$, $4.3 \pm 0.4 \times 10^{-14}$, $8 \pm 2 \times 10^{-14}$ and $8.8 \pm 0.3 \times 10^{-14}\ cm^2/s$ at annealing temperatures of 175, 200, 225 and 250°C, respectively. Values of $D_{Cu(PVD)}$ of the order of 10^{-15} to $10^{-16}\ cm^2/s$ were reported for Cu diffusion from Cu(InGa)Se_2 source layer [94]. The concentration profiles were measured by photoelectron spectroscopy (PES) while the values of $D_{Cu(PVD_In2S3)}$ were estimated from the integral amount of diffused Cu.

Figure 4.19 shows the simulated and measured Cu concentration profiles for ILGAR(acac)-In_2S_3:Cu after annealing at 150, 175, 200 and 250°C temperatures and removal of CuSCN. The profiles were fitted with one diffusion coefficient each, signifying one diffusion mechanism of Cu diffusion in ILGAR(acac)-In_2S_3 layers. The values of $D_{Cu(ILGAR(acac))}$ amounted to $1.04 \pm 0.05 \times 10^{-14}$, $5.5 \pm 0.3 \times 10^{-14}$, $7.4 \pm 0.4 \times 10^{-14}$, $1.0 \pm 0.5 \times 10^{-13}$ and $1.35 \pm 0.07 \times 10^{-13}\ cm^2/s$ at annealing temperatures of 150, 175, 200, 225 and 250°C, respectively. Values of $D_{Cu(PVD)}$ and $D_{Cu(ILGAR(acac))}$ are of the same order of magnitude. Similar mechanism of Cu diffusion can therefore be expected.

Simulated and measured concentration profiles for ILGAR(Cl)-In_2S_3:Cu after annealing for 5 min and removal of CuSCN are shown in figure 4.20. Profiles from four different ILGAR(Cl)-In_2S_3:Cu layers with residual Cl amounts of (a) 7.8at.%, (b) 8.5 at.%, (c) 11.3 at.% and (d) 13.8 at.% are shown. The relatively high concentration of the thin

surface layer was not taken into account during simulation of the profiles. The profiles could be fitted well with one diffusion coefficient especially for temperatures below 225°C.

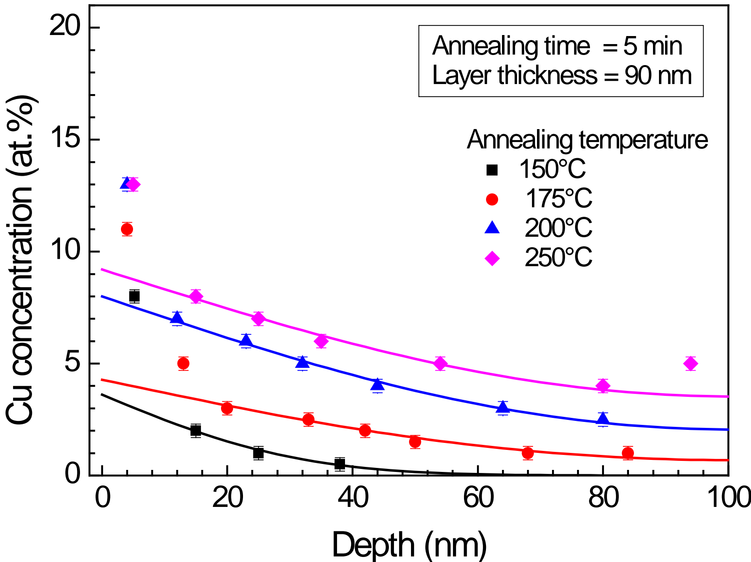

Figure 4.19: Simulated and measured Cu depth profiles for ILGAR(acac)-In_2S_3:Cu after annealing at 150, 175, 200 and 250°C temperatures and removal of CuSCN

Cu concentration profiles of ILGAR(Cl)-In_2S_3:Cu layers were less steep compared to those of ILGAR(acac)-In_2S_3:Cu and PVD-In_2S_3:Cu layers. After annealing for 5 min at temperatures of 225°C or higher, the thickness of the surface layer with high Cu content increased. Two components of the profiles consisting of an additional steeper part near the surface appeared. This feature was more enhanced for samples with Cl content of 7.8 at.% (a) and 8.6 at.% (b) and can be associated with a second diffusion process that may occur at higher temperatures.

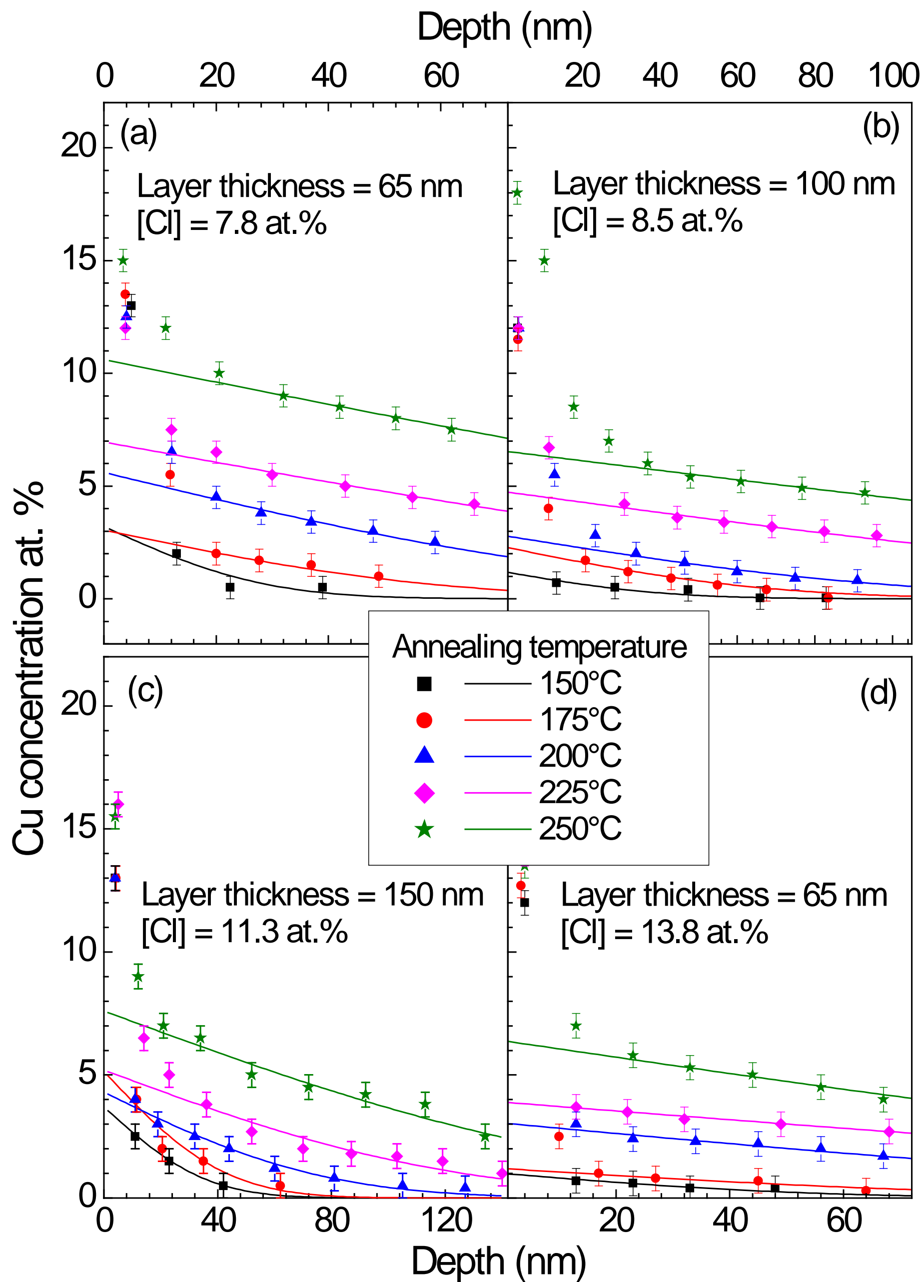

Figure 4.20: Simulated and measured Cu depth profiles of ILGAR(Cl)-In_2S_3:Cu after annealing at 150, 175, 200, 225 and 250°C temperatures and removal of CuSCN. . The values of [Cl] were 7.8 at.%, (b) 8.5 at.%, (c) 11.3at.% and 13.8 at.%. Corresponding layer thicknesses are indicated.

4.2.2. Thermal activation of Cu diffusion

The values of $D_{Cu(PVD)}$, $D_{Cu(ILGAR(acac))}$, and $D_{Cu(ILGAR(Cl))}$ were compared in an Arrhenius plot as shown in figure 4.21. Values of $D_{Cu(PVD)}$ and $D_{Cu(ILGAR(acac))}$ were plotted in one graph as shown in figure 4.21 (a). Values of $D_{Cu(ILGAR(Cl))}$ for different Cl contents were plotted in one graph as shown in figure 4.21(b). The activation energies (E_A) and diffusion prefactors (D_0), also called pre-exponential factors, were obtained from the slopes and vertical intercepts of the graphs, respectively.

The relationship between D, D_0 and E_A is given by the Arrhenius expression;

$$D(T) = D_0 exp\left(-\frac{E_A}{k_B T}\right) \qquad (4.4.)$$

where $k_B = 8.617 \times 10^{-5}\ eV/K$ is the Botzmann constant and T the temperature in kelvin scale.

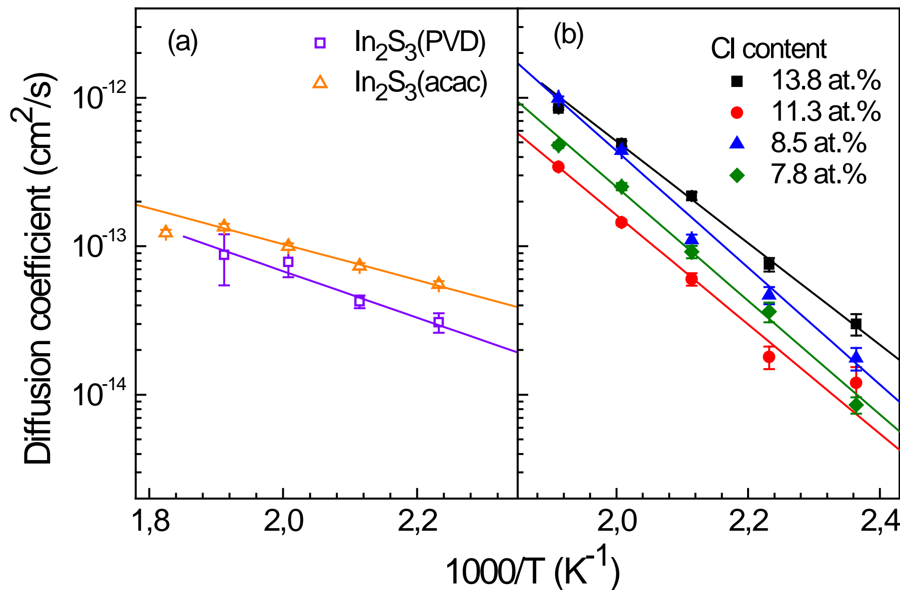

Figure 4.21: Arrhenius plot for diffusion coefficient of Cu against temperature in PVD-In_2S_3 and ILGAR(acac)-In_2S_3 (a) and ILGAR(Cl)-In_2S_3 layers (b) with varying Cl contents.

The values of E_A, $D_{Cu(PVD)}$ and $D_{Cu(ILGAR(acac))}$ were comparable. The slopes of $D_{Cu(ILGAR(Cl))}$ for the four Cl concentrations are similar. Values of E_A for Cu diffusion

in PVD-In_2S_3 and ILGAR(acac)-In_2S_3 amounted to 0.30 and 0.24 eV, respectively. The Values of D_0 for Cu diffusion in PVD-In_2S_3 and ILGAR(acac)-In_2S_3 layers were 9.0×10^{-11} and $2.7 \times 10^{-11}\ cm^2/s$, respectively. The diffusion barrier for Cu migration in PVD-In_2S_3 and ILGAR(acac)-In_2S_3 layers was of the same order. Similar values of D_0 and E_A point to a similar diffusion mechanism of Cu diffusion in PVD-In_2S_3 and ILGAR(acac)-In_2S_3 layers. Values of E_A and D_0 for Cu diffusion in PVD-In_2S_3, ILGAR(acac)-In_2S_3 and ILGAR(Cl)-In_2S_3 are given in table 4.2.

Both PVD-In_2S_3 and ILGAR(acac)-In_2S_3 layers are stoichiometric although ILGAR(acac)-In_2S_3 may contain very small amounts of carbon from the solvent. Diffusion of Cu in PVD-In_2S_3 layers was accompanied by structural changes. On the other hand, ILGAR(acac)-In_2S_3 layers were deposited at 200°C but no significant structural changes were observed from XRD analysis.

Table 4.2: Activation energies and diffusion prefactor for Cu diffusion in In_2S_3 layers

	In_2S_3:Cl 13.8at.%	In_2S_3:Cl 11.3at.%	In_2S_3:Cl 8.5at.%	In_2S_3:Cl 7.8at.%	In_2S_3: acac	In_2S_3: PVD
E_A (eV)	0.70	0.72	0.78	0.76	0.24	0.30
D_0 (cm^2/s)	6.0×10^{-6}	3.0×10^{-6}	3.2×10^{-5}	1.2×10^{-5}	2.7×10^{-11}	9.0×10^{-11}

Values of D_0 and E_A for Cu diffusion in ILGAR(Cl)-In_2S_3 layers were on the same order despite changing the Cl concentration by a factor of two. There was no systematic change of either D_0 or E_A with corresponding change in Cl concentration. The values of D_0 for ILGAR(Cl)-In_2S_3 layers were about 5 orders of magnitude higher than values for both PVD-In_2S_3 and ILGAR(acac)-In_2S_3 layers while the values of E_A for ILGAR(Cl)-In_2S_3 layers were more than twice those for PVD-In_2S_3 and ILGAR(acac)-In_2S_3 layers. The diffusion process was faster in the Cl-containing than in Cl-free In_2S_3 layers.

The presence of Cl in In_2S_3 layers leads to a broadening of the band gap, to an increased photosensitivity [134] and to a decrease in the work function [135]. The average crystallite sizes for as-deposited ILGAR(acac)-In_2S_3 and ILGAR(Cl)-In_2S_3 layers were 9.7 and 10.1 nm, respectively as reported in section 3.4.1. The change in the crystallite sizes after annealing during diffusion experiments was similar. The effect of

grain boundary diffusion cannot therefore account for the difference in the diffusion parameters between Cl-free and Cl-containing In_2S layers. The difference in electronic properties could be the reason for the different diffusion mechanism.

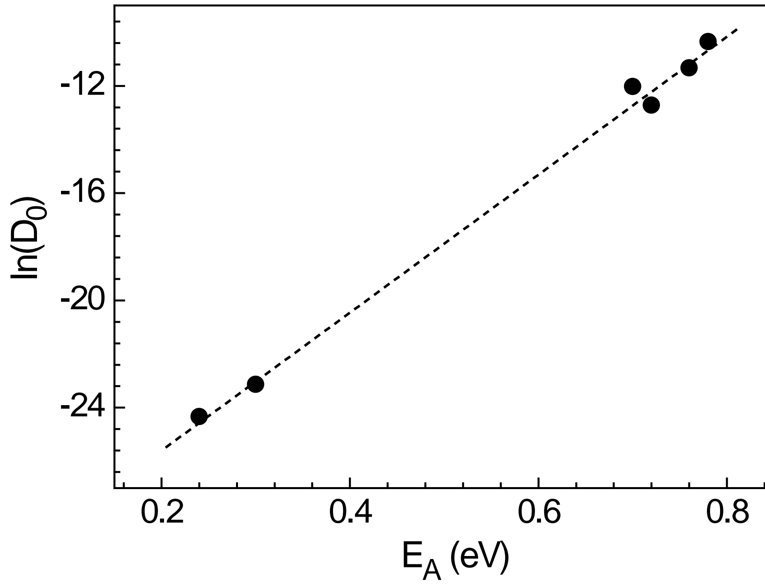

Figure 4.22: Relationship between natural logarithm of diffusion prefactor and activation energy.

Figure 4.22 shows a plot of $ln(D_0)$ against E_A for Cu diffusion in different In_2S_3 layers obtained in this work. The relationship between D_0 and E_A can be described by the MNR with $E_{MN} = 40\, meV$ and a diffusion coefficient at the activated state of $D_{00} = 5 \times 10^{-14}\, cm^2/s$. The values of E_{MN} in atomic diffusion processes have been reported to be in the range of 25 – 200 meV [58]. The value of D_{00} is the same order as $D_{Cu(In2S3)}$. The isokinetic temperature $T_0 = E_{MN}/k_B = 464\, K$. The temperature range for the diffusion experiment was between 150 and 250°C, whose average temperature (T_A) is 473 K, which is close to the value of $T_0 = 464\, K$. The MN energy can be associated with the average temperature for the experimental range covered in this work as discussed in literature [54, 56, 55]. As a remark, a survey of literature values of E_{MN} or T_0 shows a close relationship between T_0 and T_A.

4.2.3. The role of Cl on Cu diffusion in In_2S_3 layers

Stoichiometry and local bond configuration

The stoichiometry of the In_2S_3 layers was obtained from the ratios of the concentrations of the constituent elements as determined from RBS analysis. The concentrations (in at.%) [In], [S] and [Cl] together with the ratio [S]/[In] are given in table 4.3. The ratio [S]/[In] for stoichiometric In_2S_3 is 1.5. The PVD-In_2S_3 layer (not shown in table 4.3) had a ratio [S]/[In] = 60.5/39.5 = 1.53. Sample A corresponds to a ILGAR(acac)-In_2S_3 layer and a ratio of [S]/[In] = 1.56, which is close to the stoichiometry of In_2S_3. Therefore deviations from stoichiometry caused by incorporation of some carbon from the solvent can be neglected. Samples B, C, D and E correspond to ILGAR(Cl)-In_2S_3 layers with different [Cl] contents. The deviation from stoichiometry increased with increasing Cl amount. The ratio [S]/[In] amounted to 1.44, 1.43, 1.39 and 1.32 corresponding to Cl concentrations of 7.8, 8.5, 11.3 and 13.8 at.%, respectively.

Table 4.3: Stoichiometry of In_2S_3 layers.

Sample	[In]	[S]	[Cl]	[S]/[In]	Formula
A	39	61	0	1.56	In_2S_3
B	37.8	54.4	7.8	1.44	$In_4S_{5.76}Cl_{0.83}$
C	37.6	53.9	8.5	1.43	$In_4S_{5.73}Cl_{0.91}$
D	37.5	52.2	11.3	1.39	$In_4S_{5.57}Cl_{1.21}$
E	37.1	49.1	13.8	1.32	$In_4S_{5.29}Cl_{1.49}$

Different bond configurations between In-S-Cl that may exist in ILGAR(Cl)-In_2S_3 were proposed as illustrated by the schematic in figure 4.23. Figure 4.23 (a) represents the local bond configuration of stoichiometric In_2S_3. There are three S atoms for each two In atoms giving stoichiometric ratio [S]/[In] = 1.5. If the place of S was occupied by two Cl atoms, the local bond configuration would be as in figure 4.23 (b). The chemical formula becomes $In_2S_{3-x}Cl_{2x}$.

Another case, which may be equivalent to an intermediate stage in the sulfurization process, is given in figure 4.23 (c). An excess of Cl bonded to either S or In or sitting in

an antisite position may exist in the intermediate stages with incomplete sulfurization. The corresponding chemical formula is $In_2S_3Cl_{2y}$. A more complex case with excess of both Cl and / or In may exist in the intermediate stages. This is illustrated in figure 4.23 (d). The chemical formula becomes $In_{2+w}S_3Cl_{2y}$.

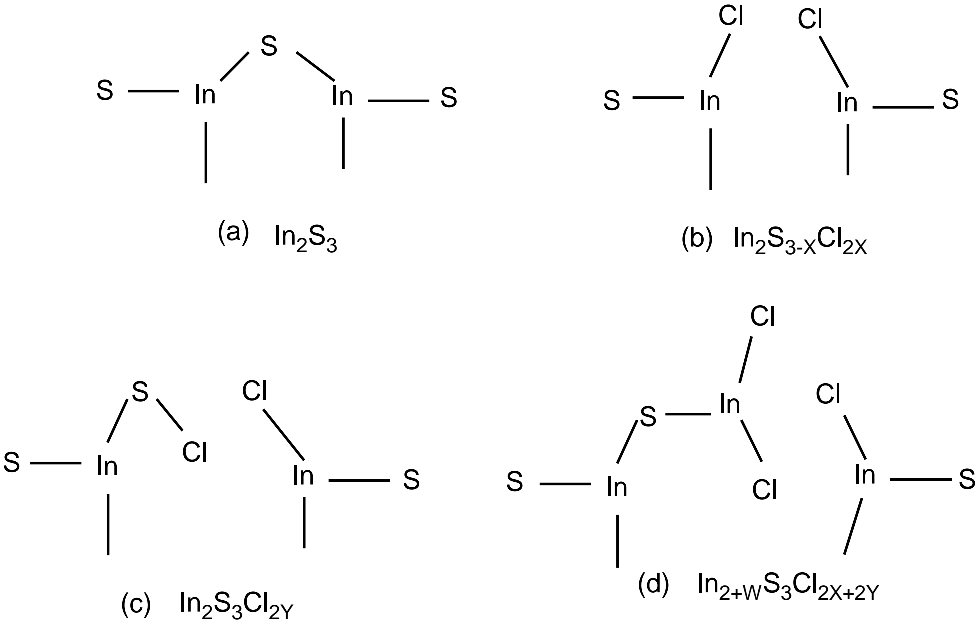

Figure 4.23: Local bond configuration for ILGAR(Cl)-In_2S_3

The general chemical formula for ILGAR(Cl)-In_2S_3 was obtained as $In_4S_{6\text{-}x}Cl_{2x+2y}$. The subscript X characterizes the Cl not substituted during sulfurization and which occupies S places in In_2S_3. The subscript Y characterizes excess Cl found in In_2S_3. The excess Cl may be bonded to either In or S. For stoichiometric In_2S_3 both X and Y are each equal to zero. The relationship between X and Y is given in figure 4.24. There was a drop in the value of Y with an increase in X when Cl content was increase from 8.5 to 11.3 to 13.8 at.%. Direct dependence of Y on X with change in Cl content was not clear. The amount of excess Cl does not depend on the amount of unreacted or overall residual Cl.

Figure 4.25 shows the dependence of activation energy (E_A) on X and Y. There was an exponential decrease of the E_A with increase in X. The value of E_A decreased from 0.78 to 0.70 eV while X increased from 0.22 to 0.71. An increase in the Cl content within the range investigated in this work resulted in a decrease in the energy barrier (E_A) for

Cu diffusion in ILGAR(Cl)-In_2S_3. There was no dependence of E_A on Y. Only the Cl sitting in S places had an influence on the diffusion barrier. This could be related to the strong ionic In-Cl bond. The amount of excess Cl had no influence on the energy barrier for Cu diffusion in ILGAR(Cl)-In_2S_3 layers.

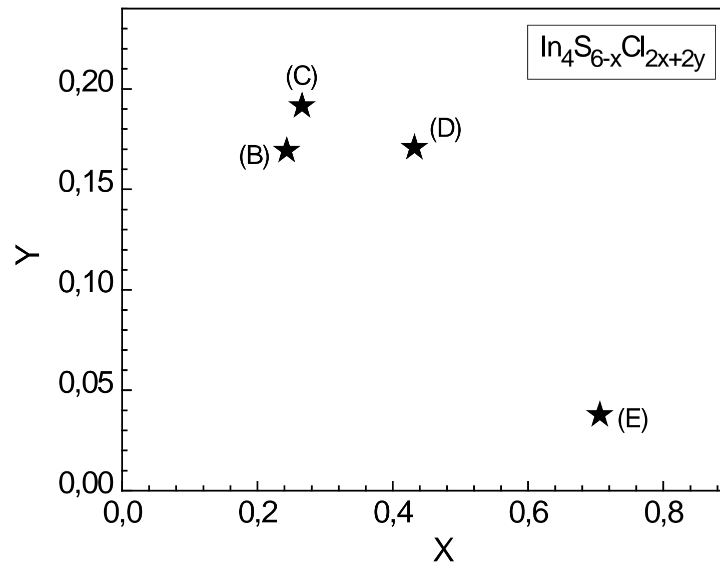

Figure 4.24: Y as a function of X. (B), (C), (D) and (E) corresponds to Cl amounts of 7.8, 8.5, 11.3 and 13.8 at.%, respectively

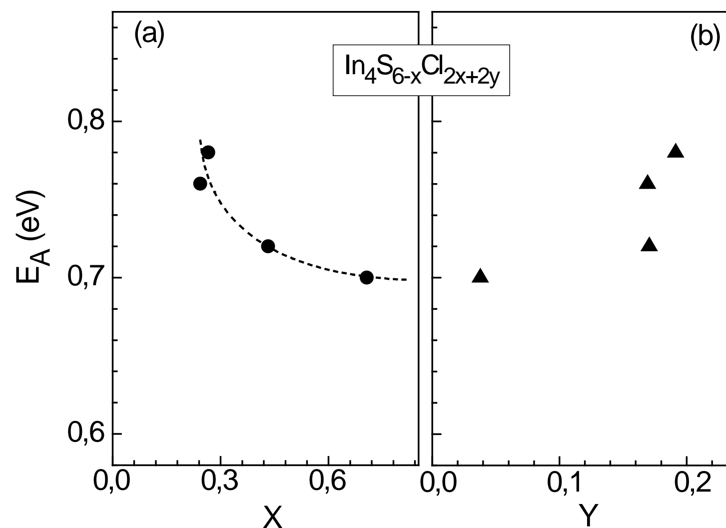

Figure 4.25: Activation energy as a function of X (a) and Y (b)

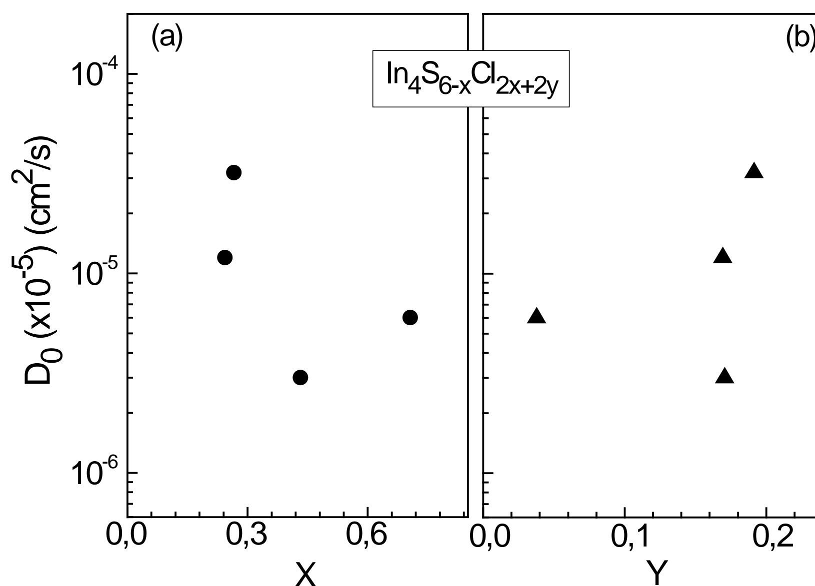

Figure 4.26: Diffusion prefactor as a function of X (a) and Y (b)

The diffusion prefactor D_0 was plotted against X and Y as shown in figure 4.26. The values of D_0 were scattered about 10^{-5} cm^2/s and showed no particular dependence on either X or Y values. D_0 for Cu diffusion in ILGAR(Cl)-In_2S_3 was 5 or 6 orders of magnitude higher than in ILGAR(acac)-In_2S_3 and PVD-In_2S_3. The presence of Cl in ILGAR(Cl)-In_2S_3 raised the value of D_0 independent of the Cl amount.

Cl ions have a radius of 181 pm and may enlarge the interstitial spaces in In_2S_3. This allows faster diffusion of Cu by percolation through the spaces. The diffusion prefactor (D_0) depends on geometrical parameters of the host matrix characterizing the jump frequency, number of available sites for diffusion and entropy. The different bond configurations can change the distance between jump sites for diffusion. This accounts for the large value of $D_{0(ILGAR(Cl))}$ compared to $D_{0(ILGAR(acac))}$ and $D_{0(PVD)}$.

Diffusion mechanisms of Cu migration in In_2S_3

To understand the role of Cl on diffusion of Cu in In_2S_3, a model was proposed that helped describe the movement of diffusing Cu in Cl-free and Cl-containing In_2S_3 host matrix as shown in figure 4.28. Cu diffuses by vacancy [40] or substitution and insertion mechanisms [30] as illustrated in figure 4.28 (a).

Cu occupies some of the cationic vacancies on tetrahedral sites by process 1 and also substitutes for In on tetrahedral sites by process 2 in figure 4.27 (a). In process 1, Cu moves to occupy a nearby In vacancy. The activation energy of Cu diffusion by the vacancy mechanism must be lower than In self-diffusion by the vacancy mechanism for this to occur. In process 2, Cu diffuses by substituting for In in lattice positions. In stoichiometric In_2S_3 such as PVD-In_2S_3 and ILGAR-In_2S_3(acac) process 1 and 2 take place simultaneously [40]. In the presence of Cl, the volume of space in In_2S_3 structure increases due to the size of Cl ionic radius. Cu diffuses by process 3 involving percolation through the partially open spaces. Substitution of In by Cu was limited by the Cl bonded onto In and/or S.

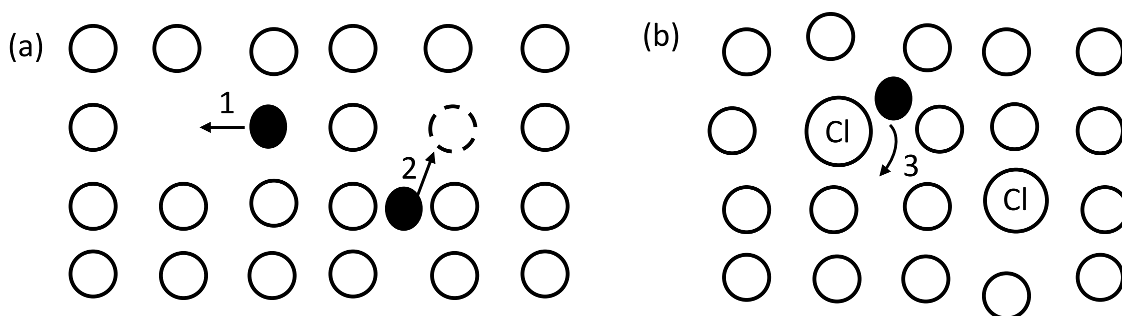

Figure 4.27: Model for diffusion of Cu in In_2S_3

The activation energy of atomic diffusion is influenced by the nature of bonding [136]. Residual Cl can be bonded to either In or S, as discussed earlier. The bond dissociation energies of In-Cl, In-S, Cu-Cl, Cu-S, S-Cl and In-Cu are 436, 288, 378, 275, 242 and 187 KJ/mol, respectively [137]. The In-Cl bond is the strongest in the In_2S_3(Cl):Cu matrix. In general, the activation energy is the energy needed for a migrating atom to overcome and break surrounding bonds and move to an activated state.

The stronger In-Cl bond can explain the increase in activation energy for diffusion of Cu in ILGAR(Cl)-In_2S_3 compared to Cl-free ILGAR(acac)-In_2S_3 and PVD-In_2S_3. The presence of Cl reduces the density of vacancies in In_2S_3. Some Cl may also occupy cationic vacancies as anti-site defects and limit diffusion of Cu by vacancy mechanism. Substitution of In by Cu is limited by the relatively strong In-Cl bond compared to Cu-S bonds.

Table 4.4 summarizes the dominating diffusion processes for Cu in the different In_2S_3 layers. Cu diffuses in stoichiometric In_2S_3 by vacancy or substitution and insertion. In the presence of Cl, these mechanisms are limited and Cu diffuses by a more complex mechanism described by process 3 in figure 4.28 (b). Cl was found to play a crucial role for diffusion of Cu in In_2S_3 layers.

Table 4.4: Summary of dominating diffusion processes in In_2S_3 layers. process 1 denotes vacancy diffusion, process 2 is diffusion by substitution and process 3 is percolation.

	Process 1	**Process 2**	**Process 3**
PVD-In_2S_3	X	X	
ILGAR(acac)_In_2S_3	X	X	
ILGAR(Cl)-In_2S_3			X

In summary, diffusion of Cu in Cl-free In_2S_3 layers showed comparable values of the diffusion prefactor and activation energies. The presence of Cl in the range of 7.8 to 13.8 at.% raised the value of the activation by more than twice from 0.3 to over 0.7 eV. The ionic bonds between In and residual Cl as well as Cl occupying S and/or vacant sites in the lattice were responsible for the increased value of the activation energy. Ionic radius of Cl is large than that of In, S and Cu ions and hence additional (interstitial) spaces resulting from the presence of Cl increases the diffusion rate. The diffusion mechanism in the presence of Cl will be different from the Cl-free case and may require theoretical calculations to verify that, because no significant structural or morphological differences were observed.

5. Charge separation at In_2S_3/CuSCN interfaces

Charge separation in semiconductor materials can be investigated using surface photovoltage (SPV) techniques. A SPV signal is generated when absorption of incident illumination is followed by separation of photogenerated charge carriers in space. In this chapter, results of charge separations across In_2S_3/CuSCN interfaces are presented. Charge separation across In_2S_3/CuSCN interfaces was measured as modulated/spectral dependent SPV or time dependent relaxation of separated charge carriers in the fixed parallel plate capacitor configuration as a function of In_2S_3 layer thickness and annealing time.

5.1. Spectral dependent charge separation at In_2S_3/CuSCN interfaces

5.1.1. Role of layer thickness for charge separation in In_2S_3 layers

In_2S_3 layers of thicknesses 5, 10, 20, 40 and 80 nm were deposited onto SnO_2:F substrates by PVD. Modulated charge separation in PVD-In_2S_3 layers was measured for the different thicknesses with incident light modulated at 8 Hz. The SPV amplitude, normalized SPV amplitude and normalized amplitude divided by the photon flux are given in figure 5.1. The spectrum of the incident photon flux is shown in figure 5.1 (a).

As shown in figure 5.1 (a), the magnitude of the SPV amplitude increased with increasing thickness of the PVD-In_2S_3 layer. The SPV signal increased in amplitude with increasing layer thickness, the lowest signal coming from the 5 nm sample and the largest from the 80 nm sample. The increase in SPV amplitude between 20 and 40 nm

thickness was small. The maximum of the SPV amplitude was 0.03, 0.16, 0.25, 0.30 and 2.17 mV at photon energy of 2.5 eV for PVD-In_2S_3 layer thicknesses of 5, 10, 20, 40 and 80 nm, respectively. By increasing the layer thickness, light absorption was increased resulting in an increase in photo-generated charge carriers. In the thinner layers, the separation length of the photo-induced charges was limited by the layer thickness. The SPV signal in the near infrared region at energies below 2 eV, is due to charge separation involving defects below the band gap on In_2S_3.

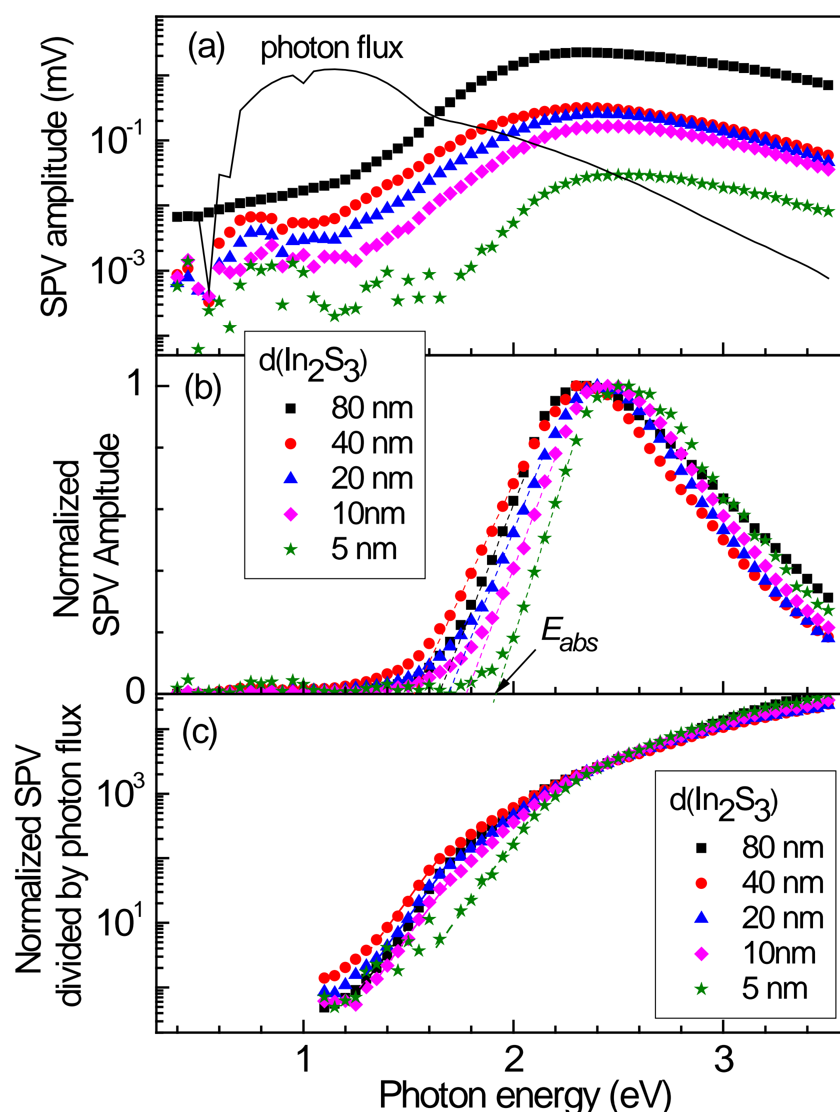

Figure 5.1: Modulated SPV amplitude (a), normalized SPV amplitude (b) and normalized SPV divided by photon flux (c) for PVD-In_2S_3 layers of thickness 5 (stars), 10 (diamonds), 20 (triangles), 40 (circles) and 80 nm (squares).

The onset of the SPV signal (E_{abs}) corresponds to the mobility gap above which there was a strong increase in the magnitude of the signal. The SPV signal in the near infrared region comes from contributions from defects below the band gap participating in charge separation. The values of E_{abs} were obtained by first normalizing the SPV amplitude and extrapolating the leading edge of the SPV signal to the photon energy scale and reading out the energy at the intersection point as shown in figure 5.1 (b). The values of E_{abs} amounted to 1.93, 1.78, 1.68, 1.52 and 1.64 eV corresponding PVD-In_2S_3 layer thickness of 5, 10, 20, 40 and 80 nm, respectively. The onset of the SPV absorption shifted towards lower photon energies with increasing thickness. The shift in the SPV onset energy is concomitant with a shift in the band gap with increasing layer thickness.

The mismatch in the thermal expansion coefficients between the layers and the substrate results in strain which can affect electronic properties of the layers. The decrease in the optical band gap with increasing layer thickness was reported for evaporated In_2S_3 layers [138]. The strain in In_2S_3 layers below 200 nm thick was tensile and decreased with increasing thickness. It can be concluded that the nature of strain in PVD-In_2S_3 layers of thickness between 5 and 80 nm was tensile and it reduced with increasing layer thickness.

Dividing the normalized SPV amplitude by the photon energy allows for investigation of exponential tail states below the band gap. The SPV signals are not directly proportional to the photon flux because the formation of SPV signals may involve more than one process; some processes may even be in the opposite direction. SPV signals are only proportional to the photon flux in the low signal regime if dominating mechanisms of charge separation and relaxation do not change. The values of the energy parameter of the exponential tail states (E_t) were obtained for PVD-In_2S_3 layers by fitting the normalized SPV spectra divided by photon flux graph with an exponential function in the region below the band gap as shown in figure 5.1 (c).

Disorder in materials leads to defect states in the band gap close to the band edge and results in an exponential drop in the SPV signal towards lower photon energies [139]. The values of E_t amounted to 98, 98, 99, 101 and 103 meV for PVD-In_2S_3 layers of thickness 5, 10, 20, 40 and 80 nm, respectively. E_t is a characteristic of the degree of disorder in a semiconductor. It is different from the Urbach tail energy in the sense that

the Urbach energy is characteristic of exponential defect states absorbing light below the band gap while E_t describes the defect states below the band gap that participate in charge separation.

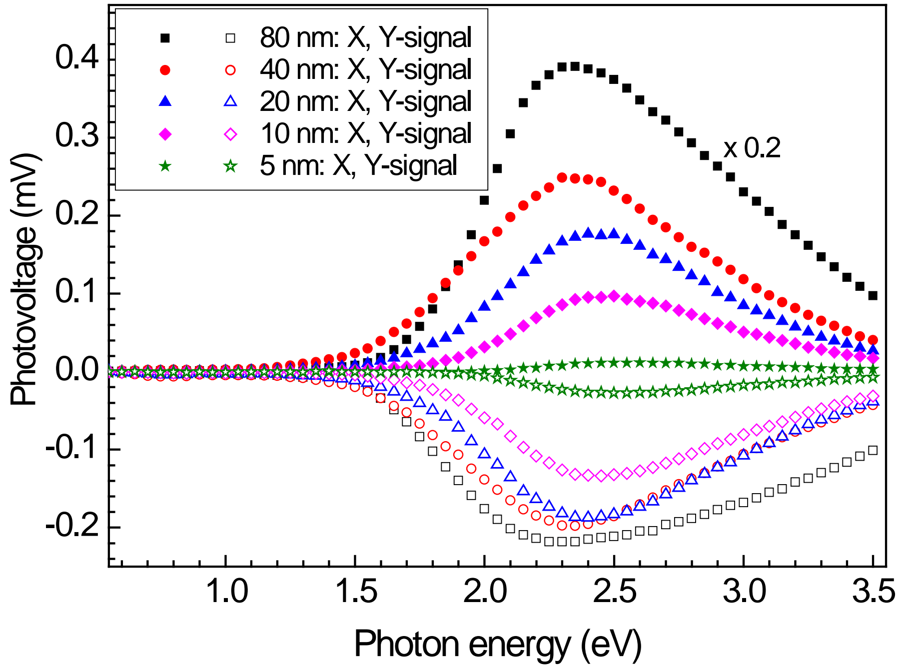

Figure 5.2: In phase (X) and phase shifted by 90° (Y) signals for PVD-In_2S_3 layers of thickness 5 (stars), 10 (diamonds), 20 (triangles), 40 (circles) and 80 nm (squares). The signal from the 80 nm layer was divided by 0.2.

Figure 5.2 shows X and Y signals for PVD-In_2S_3 layers of thickness 5, 10, 20, 40 and 80 nm. The sign of the X signal gives information about the direction of separation of photo-generated charge carriers [76]. All the X and Y signals from PVD-In_2S_3 layers were positive and negative, respectively. Positive values of X signal are characteristic for charge separation with electrons separated preferentially towards the internal interface. The amplitude of both X and Y signals increased with increasing layer thickness, hence the increase in the SPV amplitude signals.

Figure 5.3 shows the phase angles plotted as a function of photon energy and SPV amplitude. The phase angles were between -20° and -90° for all the PVD-In_2S_3 layers of thickness 5, 10, 20, 40 and 80 nm as shown in figure 5.3 (a). This means that in all the samples, photo-generated electrons were separated preferentially towards the

internal interface. The phase spectra shifted towards 0° with increasing absorption in the region near the band edge. When scanning from low to high photon energies, the onset of band-to-band optical transitions leads to faster SPV formation processes signified by a strong amplitude and a shift in the phase towards 0° or ±180° for n-type or p-type semiconductors, respectively [140]. The shift of the phase angles at the band edge towards 0° confirmed that PVD-In_2S_3 behaves as an n-type semiconductor. This is in agreement with what is found in literature [141].

The phase angle below photon energies of 1.6 eV for the 80 nm sample was constant at -65° but increased strongly towards 0° above 1.6 eV photon energies due to increased optical absorption near the band edge. This corresponds to the onset energy (E_{abs}) of 1.64 eV discussed earlier. For PVD-In_2S_3 layers of thickness 20 and 40 nm, the phase angles below 1.8 eV photon energies were -55° and -42°, respectively, showing contribution to SPV formation from defect states below the band gap.

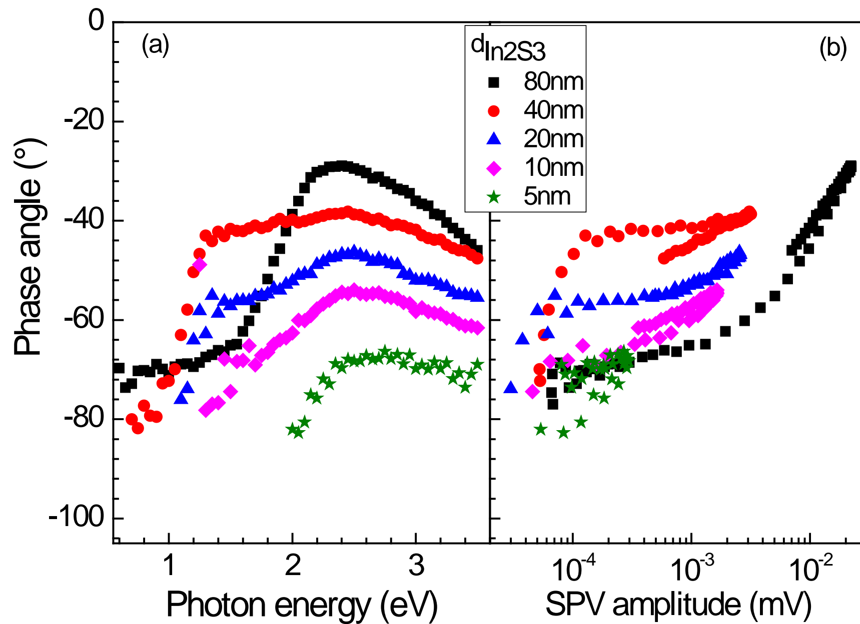

Figure 5.3: phase angle as a function of photon energy (a) and SPV amplitude (b) for PVD-In_2S_3 layers of thicknesses 5 (stars), 10 (diamonds), 20 (triangles), 40 (circles) and 80 nm (squares).

Figure 5.3 (b) shows the dependence of the phase angle on the SPV amplitude. For all the samples, the phase was independent of the SPV amplitude at lower photon energies.

Constant phase angles and hence similar charge separation, transfer and recombination mechanisms can occur for example if the unmodulated quasi Fermi levels do not change [139]. The phase angles for the 5 nm thick samples were scattered around -70° due to a small SPV signal. The phase angle changed towards 0° as the SPV amplitude increased near the absorption edge for 10, 20, 40 and 80 nm samples. The intensity of the halogen lamp used for illumination reduced at shorter wavelengths and the SPV signal went down. This is the reason for the small hysteresis at higher photon energies. Hysteresis is caused by a difference in charge separation and mechanisms at low and high photon energies.

5.1.2. Role of annealing temperature for charge separation at In_2S_3/CuSCN interfaces

Figure 5.4 shows X and Y signals from PVD-In_2S_3/CuSCN before and after annealing at 200°C for 2 and 9 min. The thicknesses of the PVD-In_2S_3 layers were 80, 20 and 10 nm. For the sample of 80 nm thickness, the X signal was positive and the Y signal was negative before and after annealing at 200°C for 2 and 9 min as shown in figure 5.4 (a), (b) and (c). This means that photo-generated electrons were separated preferentially towards the internal interface. The amplitude of both X and Y signals increased after annealing at 200°C for 2 min compared to as-deposited signals. After annealing up to 9 min the X and Y signals decreased strongly by almost half the magnitude.

For the 20 nm thick PVD-In_2S_3/CuSCN sample, the X signal was positive and the Y signal was negative before and after annealing at 200°C for 2 min. The amplitudes of X and Y signals reduced by more than one order of magnitude after annealing at 200°C for 2 min. They reduced even further by one order of magnitude after annealing for 9 min. A new signal was observed in the defects region below the band gap after annealing for 19 min. For the 10 nm thick PVD-In_2S_3/CuSCN sample, the X signal was positive and the Y signal was negative only for the as deposited case. After annealing at 200°C for 2 min or 9 min, the Y signal changed to positive. After annealing for 2 min or longer the X and the Y signals were smaller by two orders of magnitude compared to the signals of the as-deposited sample.

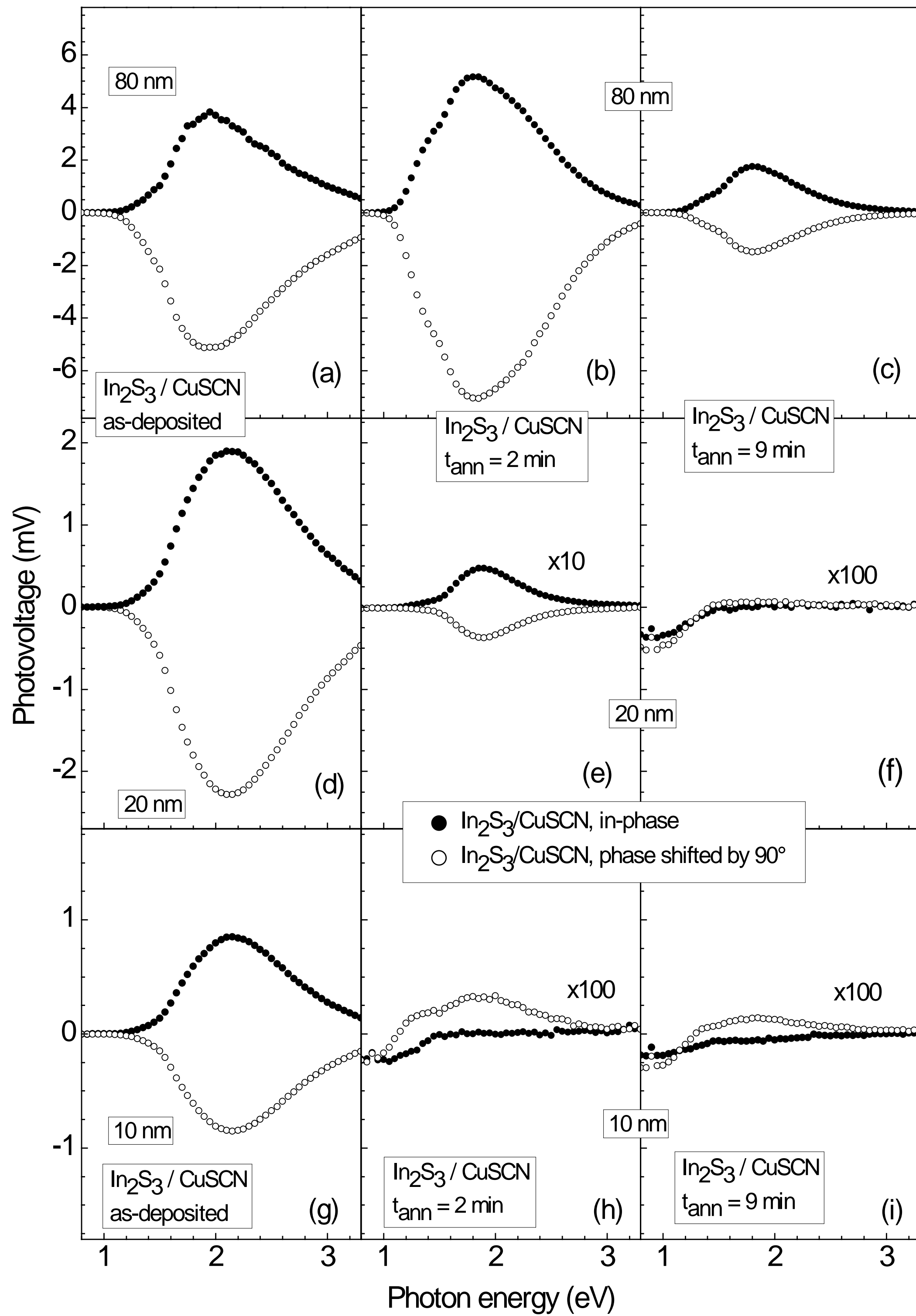

Figure 5.4: In-phase (filled symbols) and phase shifted by 90° signals (open symbols) for 80 (a, b, c), 20 (d, e, f) and 10 nm (g,h,i) In_2S_3/CuSCN samples before (a, d, g) and after annealing at 200°C for 2 min (b, e, h) and 9 min (c, f, i).

The amplitudes of the SPV signals for bare PVD-In_2S_3, PVD-In_2S_3/CuSCN before and after annealing for 2, 4, 9, and 19 min are shown in figure 5.5 for PVD-In_2S_3 thickness of 80, 40, 20 and 10 nm. The spectrum for the photon flux is also included in each graph. For the 80 nm sample, the SPV amplitude increased and shifted towards lower photon energies after deposition of CuSCN. After annealing at 200°C for 2 min, the amplitude increased further but started to drop after annealing for longer times. The amplitude of the PV signals were 2.17 mV for PVD-In_2S_3, 6.40, 8.74, 1.74, 2.28 and 3.88 mV for PVD-In_2S_3/CuSCN before and after annealing at 200°C for 2, 4, 9 and 19 min, respectively.

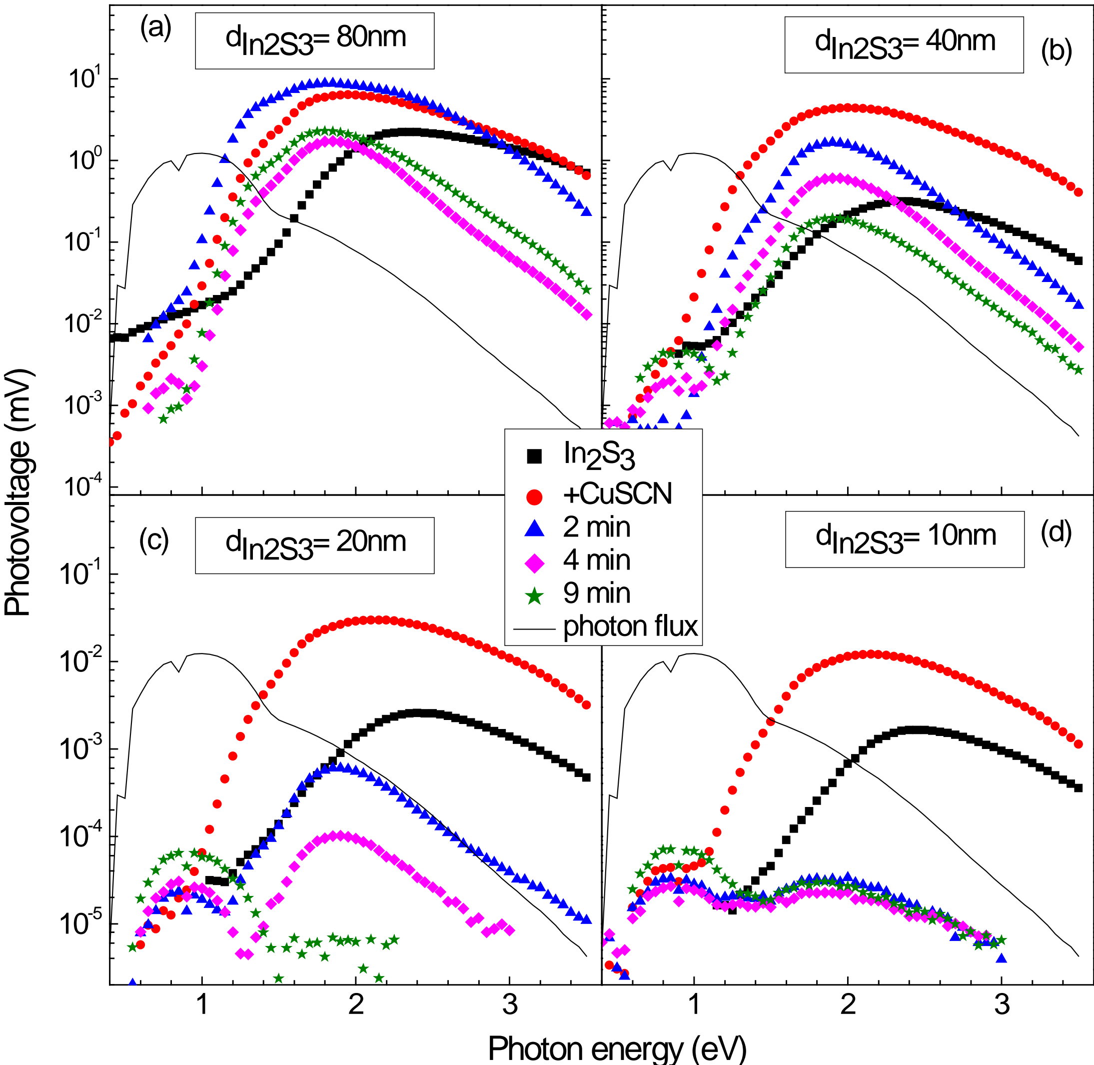

Figure 5.5: SPV amplitude for PVD-In_2S_3 /CuSCN layers before (squares) and after deposition of CuSCN (circles) and annealing at 200°C for 2 (triangles), 4 (diamonds) and 9 min (stars). Thicknesses of the In_2S_3 layers were 80 (a), 40 (b), 20 (c) and 10 nm (d).

The onset of the SPV absorption (E_{abs}) for the sample with layer thickness of 80 nm was 1.64 eV for bare PVD-In_2S_3 but shifted to 1.32 eV after deposition of CuSCN. The value of E_{abs} decreased further to 1.04, 1.35, 1.16 and 1.05 eV after annealing at 200°C for 2, 4, 9 and 19 min, respectively. The energy parameter of exponential tails (E_t) was 103 meV for bare PVD-In_2S_3 and 105 meV for as-deposited PVD-In_2S_3/CuSCN layers. The values of E_t amounted to 136, 110, 125 and 140 meV after annealing at 200°C. The degree of disorder increased with increasing annealing time.

For the sample of 40 nm thickness, the SPV amplitude signal increased strongly after deposition of CuSCN from 0.30 mV for bare PVD-In_2S_3 to 4.4 mV for as-deposited PVD-In_2S_3/CuSCN. After annealing at 200°C for 2 min, the amplitude decreased to 0.61 mV and further to 0.20, 0.72 and 0.72 mV after annealing for 4, 9 and 19 min, respectively. The SPV amplitude decreased strongly after annealing at 200°C for times longer than 2 min.

The onset of SPV absorption for the 40 nm thick sample shifted from 1.52 eV for bare PVD-In_2S_3 to 1.29 eV for as-deposited PVD-In_2S_3/CuSCN layer system. After annealing at 200°C for 2, 4, 9 and 19 min the value of E_{abs} changed to 1.44, 1.46, 1.35 and 1.39 eV, respectively. The change in E_{abs} with annealing time was not systematic. The value of E_t for bare PVD-In_2S_3 was 101 meV but increased slightly to 104 meV after deposition of CuSCN. E_t reduced to 99, 80, 88 and 98 meV after annealing at 200°C for 2, 4, 9 and 19 min, respectively.

For the 20 nm sample, the SPV amplitude increased strongly after deposition of CuSCN onto PVD-In_2S_3 layer but decreased sharply after annealing at 200°C for 2 min. a new SPV signal was observed below photon energies of 1.4 eV after annealing PVD-In_2S_3/CuSCN for 2 min or longer. It increased in amplitude while the signal above 1.4 eV diminished with increasing annealing time. The signal below 1.4 eV was due to charge separation involving a defect band that was formed during annealing. The signal from the defect band dominated especially after annealing for 4 min. The values of E_{abs} and E_t could only be obtained reliably for up to 4 min of annealing time. E_{abs} amounted to 1.69, 1.37, 1.43 and 1.43 eV for bare PVD-In_2S_3, as-deposited PVD-In_2S_3/CuSCN and after annealing at 200°C for 2 and 4 min, respectively. The onset of SPV absorption shifted to lower photon energies and remained almost constant independent of annealing duration. The value of E_t was 99 meV for bare PVD-In_2S_3 but reduced to 98, meV after

deposition of CuSCN before and after annealing at 200°C for 2 min and to 80 meV after annealing for 4 min, respectively.

For the 10 nm sample, the SPV amplitude increased strongly after deposition of CuSCN onto PVD-In_2S_3 but diminished after annealing at 200°C for short times of 2 min. the SPV signal caused by absorption in the defect band was observed immediately after deposition of CuSCN even before heat treatment and increased with increasing annealing temperature. The value of E_t decreased from 98 meV for bare PVD-In_2S_3 to 89 meV after deposition of CuSCN. The values of E_t after annealing were not reliable because the signal from the defect band was dominant in the SPV spectra.

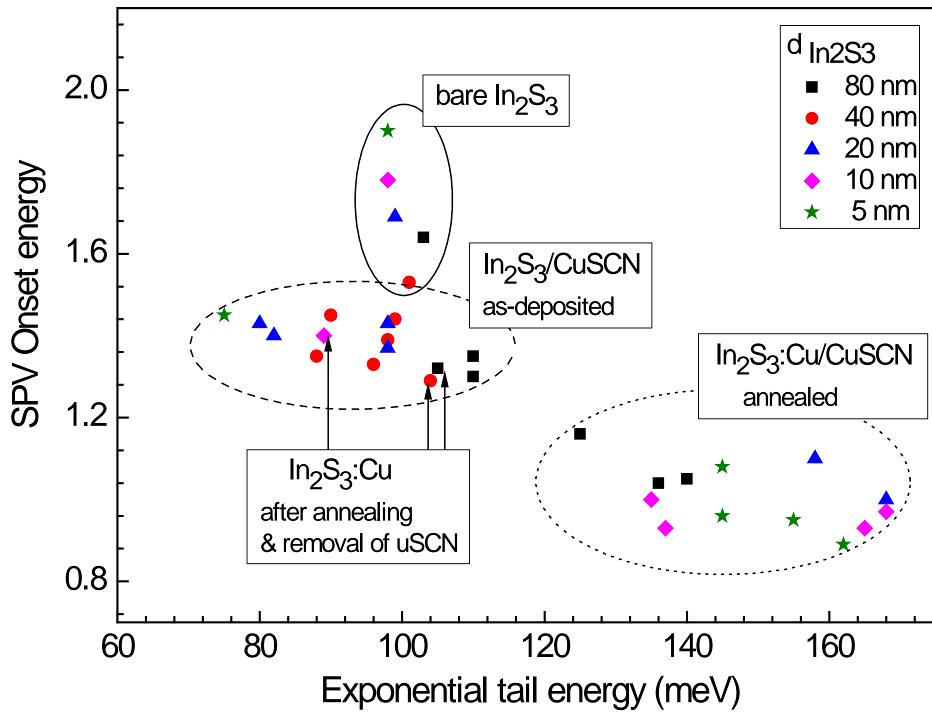

Figure 5.6: Onset of SPV absorption (E_{abs}) for all samples and annealing times (at 200°C annealing temperature) as a function of the exponential tail energy (E_t) for bare PVD-In_2S_3, PVD-In_2S_3/CuSCN before and after annealing and PVD-In_2S_3:Cu after removal of CuSCN in pyridine. The thicknesses of the PVD-In_2S_3 layers were 5 (stars), 10 (diamonds), 20 (triangles), 40 (circles) and 80 nm (squares). Four groups for (i) bare PVD-In_2S_3, (ii) as-deposited PVD-In_2S_3/CuSCN together with PVD-In_2S_3:Cu after etching away CuSCN in pyridine and (iii) PVD-In_2S_3:Cu/CuSCN after annealing at 200°C were obtained.

Figure 5.6 shows the relationship between E_{abs} and E_t for bare PVD-In_2S_3 layers, as-deposited PVD-In_2S_3/CuSCN layers, PVD-In_2S_3:Cu/CuSCN layers after annealing at

200°C for 2, 4, 9 and 19 min and PVD-In_2S_3:Cu layers after removal of CuSCN by etching in pyridine solution. The relationship shows four groups of values depending on the treatment of the PVD-In_2S_3/CuSCN layer system namely (i) PVD-In_2S_3, (ii) PVD-In_2S_3/CuSCN, (iii) PVD-In_2S_3:Cu/CuSCN. PVD-In_2S_3:Cu belongs to group (ii) with regard to figure 5.6.

Group (i) shows that E_{abs} for bare PVD-In_2S_3 layers decreased with increasing layer thickness against a very small increase in E_t. The 40 nm thick layer had the lowest value of E_{abs}. According to group (ii) E_{abs} decreased compared to bare In_2S_3 and ranged between 1.2 and 1.5 eV while the E_t varied between 70 and 115 meV whereas higher values of E_t correlated with lower values of E_{abs}. Group (iii) shows a further decrease in E_{abs} with an increase in disorder parameter. Increased diffusion of Cu into PVD-In_2S_3 led to a further shift in E_{abs} to lower photon energies but increased the defect distribution below the band gap. After removal of CuSCN, the degree of disorder in PVD-In_2S_3:Cu layer systems decreased and the onset energy increased. Removal of CuSCN reduced the defect band below the band edge of PVD-In_2S_3:Cu and therefore group (iv) went to the same range as group (ii).

Figure 5.7 shows the dependence of the SPV amplitude and of the tail energy on the density of diffused Cu at the internal interface. The diffusion coefficient of Cu in PVD-In_2S_3 layers at 200°C temperature was calculated in section 4.2.1 to be $4.3 \times 10^{-14} cm^2/s$. The concentration of Cu at the internal interface was obtained using the one dimensional simulation model in section 4.2.1 for the different annealing times and PVD-In_2S_3 layer thicknesses of 5, 10, 20, 40 and 80 nm.

For the 5 and 10 nm thick layers, the density of diffused Cu at the internal interface after annealing at 200°C for 2 min was close to the concentration at the outer surface. It was discussed earlier that the amplitude of the SPV signal from the 10 nm sample dropped strongly after annealing for 2 min. This means that the amount of Cu at the internal interface was above an optimal amount that may give maximum photovoltage. The density of Cu at the internal interface for the 20 nm sample was close to the solubility limit on the order of 8 at.% after annealing for more than 4 min.

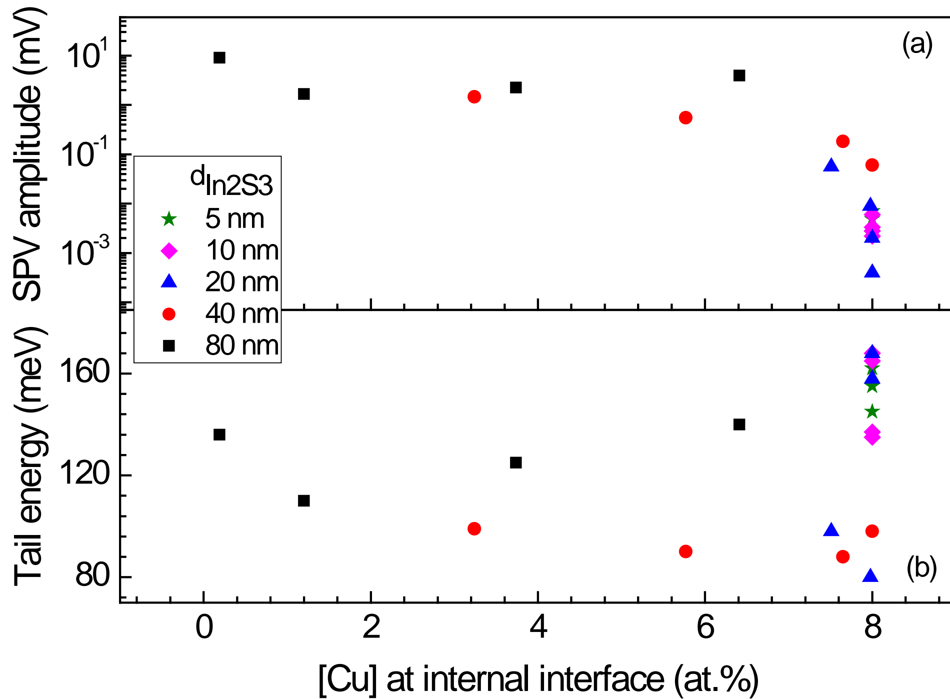

Figure 5.7: SPV amplitude and energy of exponential tail states as a function of Cu concentration at the internal interface for PVD-In_2S_3/CuSCN after annealing at 200°C for 2, 4, 9 and 19 min. The thickness of PVD-In_2S_3 layers was 5 (stars), 10 (diamonds), 20 (triangles), 40 (circles) and 80 nm (squares).

The SPV amplitude for the 40 nm sample decreased with increasing Cu density at the internal interface. The tail energy also decreased with increasing Cu amount at the internal interface until [C] = 7.7 at.% and then increased. For the 80 nm sample, both the SPV amplitude and tail energy decreased for [Cu] < 2 at.% and then increased with increasing Cu amount. For PVD-In_2S_3 layers of 40 nm or less, the highest SPV amplitude was reached without annealing while for the 80 nm it was reached after annealing for 2 min. From RBS experiments reported in chapter 4, the top layer with high Cu concentration formed at the PVD-In_2S_3/CuSCN interface was of the order of 10 nm thick. To obtain a high photovoltage in solar cells, an optimal amount of Cu needed at the internal interface has to be determined.

The phase angles of bare PVD-In_2S_3 and PVD-In_2S_3/CuSCN layer system before and after annealing at 200°C for 2, 4, 9 and 19 min for PVD-In_2S_3 thicknesses of 80, 40, 20 and 10 nm are shown in figure 5.8. For bare PVD-In_2S_3 with 80 nm layer thickness, the phase angle below the band edge was constant at -70° but changed towards 0° to -33° above the band gap due to increased absorption. The change in the phase angle towards

0° means that charge separation, transfer and recombination processes became faster with increasing number of separated charge carriers. After annealing for 2 min, the phase angle was similar to that before annealing except in the defect range.

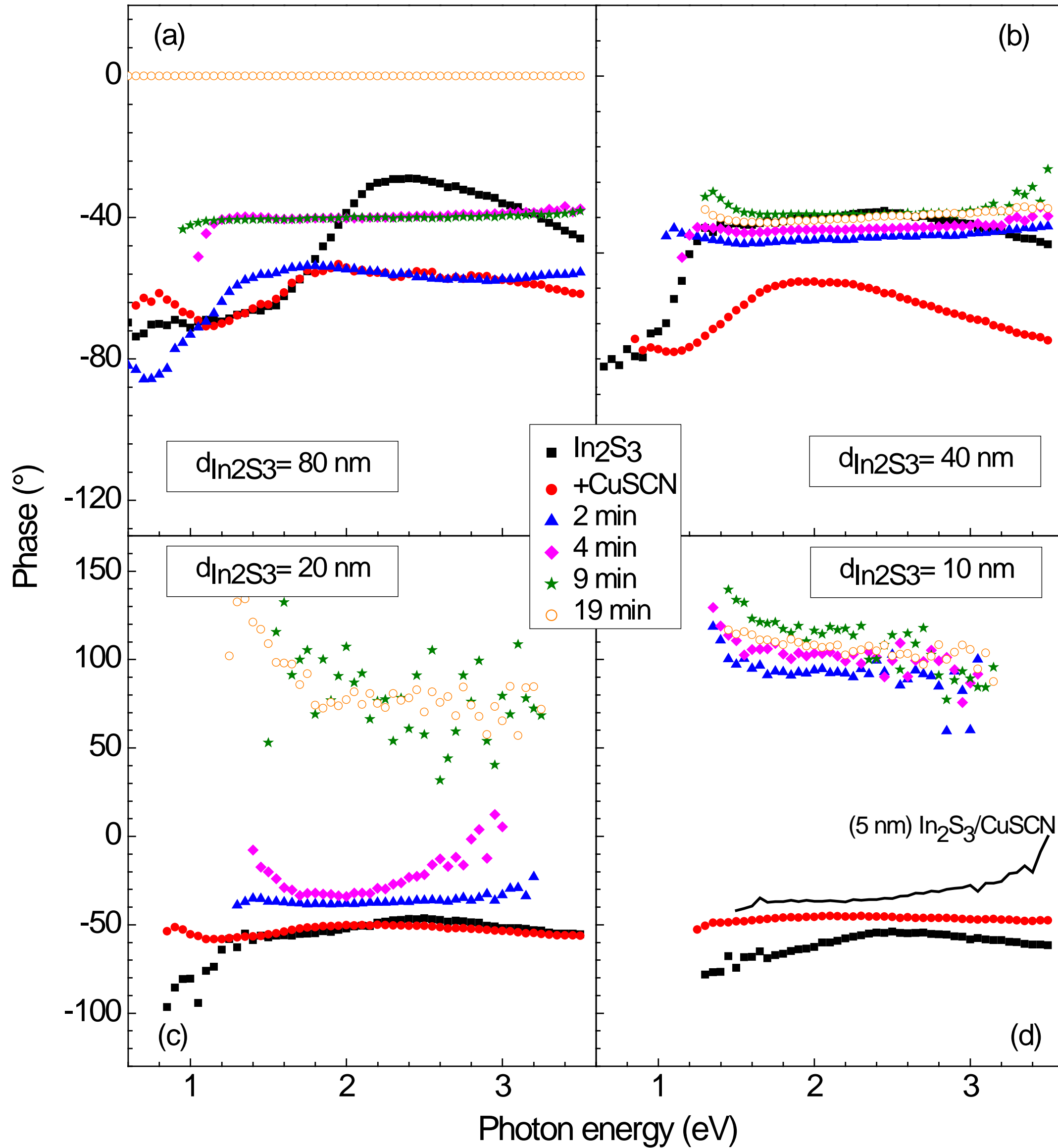

Figure 5.8: Phase angles for PVD-In_2S_3 (squares) and PVD-In_2S_3/CuSCN after deposition of CuSCN (circles) and annealing at 200°C for 2 (triangles), 4 (diamonds), 9 (stars) and 19 min (open circles). The thickness of PVD-In_2S_3 layers was 80 (a), 40 (b), 20 (a) and 10 nm (d). The phase angle for 5 nm thick as-deposited PVD-In_2S_3/CuSCN sample is also sown in (d).

The phase angle shifted to -40° after annealing for 4 and 9 min and was constant throughout the investigated spectral range. After annealing for 19 min, the phase angle

was constant at 0°. A phase angle of 0° is characteristic of fast spectral response that follows the modulation of the reference signal. For the sample with layer thickness of 40 nm, the phase spectrum shifted away from -40° to -60° after deposition of CuSCN. After annealing for 2 min or longer, the phase spectra shifted to values between -50° and -40° and were constant independent of the photon energy throughout the spectral range.

For the 20 nm sample, the phase angle for the bare PVD-In_2S_3 layer and for the as-deposited PVD-In_2S_3/CuSCN layer was -50°. Below photon energies of 1.4 eV, the phase for the bare PVD-In_2S_3 layer changed from -100 to -50°. After annealing for 2 and 4 min the phase angle shifted from -50° to -35° and to -31°, respectively. The sign of the phase angles changed to positive after annealing for 9 min or longer. The phase angles were scattered between +50° and +100° because the SPV signal was small. Phase angles closer to 90° indicate that the absolute value of the Y signal is closer to maximum and the X value close to zero.

The phase angle for the bare PVD-In_2S_3 of layer thickness 10 nm was -55° and shifted to -45° after deposition of CuSCN. The values of the phase angle changed to be between 90 and 115° after annealing for 2 min or longer and the values were more positive for longer annealing times. The phase spectrum for the as-deposited PVD-In_2S_3/CuSCN with In_2S_3 layer thickness of 5 nm is shown in figure 5.8 (d). The phase angle is almost constant at -35° but becomes less negative for higher photon energies.

5.1.3. Modulated charge separation in In_2S_3:Cu layers

Figure 5.9 shows X and Y signal for PVD-In_2S_3/CuSCN layers after annealing at 200°C for 19 min and for In_2S_3:Cu after removal of CuSCN. For the 80 nm sample, the X signal was positive and the Y signal negative after annealing at 200°C for 19 min and after removal of CuSCN but the signals decreased in amplitude after removal of CuSCN. For the 40 nm sample, the X and Y signals increased in amplitude after removal of CuSCN. For the 20 nm sample, the X and Y signals were very small after annealing for 19 min but increased strongly after removal of CuSCN. The signal from the defect band did not change much.

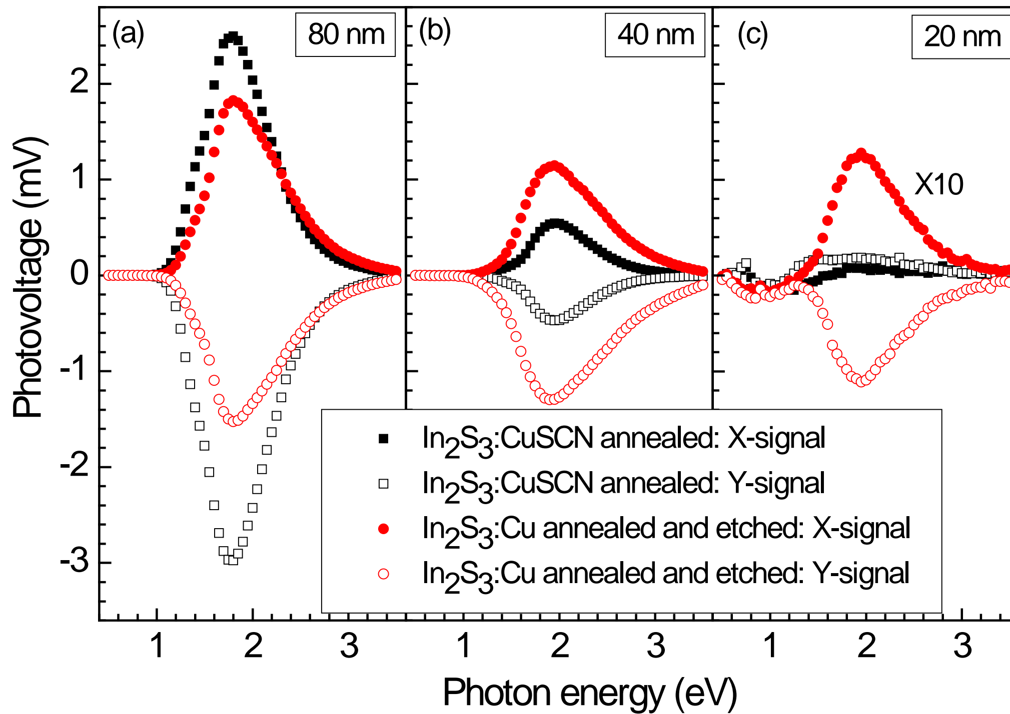

Figure 5.9: In-phase (X) (closed symbols) and phse-shifted by 90° (Y) signals (open symbols) for PVD-In_2S_3/CuSCN and PVD-In_2S_3:Cu after annealing at 200°C for 19 min before and after removal of CuSCN, respectively. Thicknesses of PVD-In_2S_3 layers were 80 (a), 40 (b) and 20 nm (c).

Figure 5.10 shows the phase angles as a function of SPV amplitude for PVD-In_2S_3:Cu layer system after annealing for 19 min and removal of removal of CuSCN. The phase angles for the 20 nm sample ranged about -40° independent of the SPV amplitude. For the PVD-In_2S_3:Cu with layer thicknesses of 40 and 80 nm, the phase angles increased with SPV amplitude. An increase in the phase angle with corresponding increase in SPV amplitude can be related to the trap filling effect. As the number of photo-excited charge carriers increase, more and more deeper traps get filled. Because their release time is longer than that for electrons trapped in shallow traps, they do not contribute any more to the SPV. The faster spectral response of the shallow traps to the modulated light results in a shift of the phase angle to less negative value with increasing SPV amplitude.

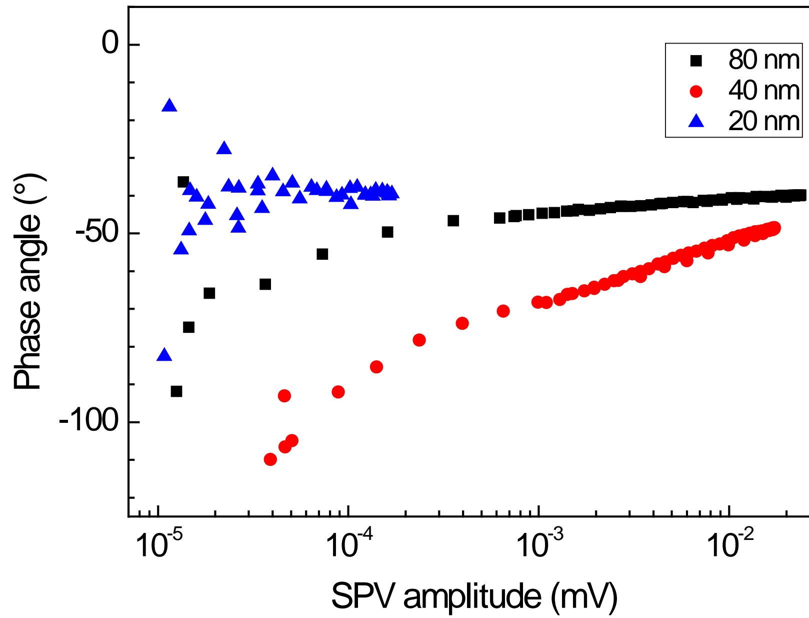

Figure 5.10: Change in phase angles with SPV amplitude for PVD- In_2S_3:Cu after deposition of CuSCN, annealing at 200°C for 19 min and removal of CuSCN. Thickness of In_2S_3 layers was 20 (triangles), 40 (circles) and 80 nm (squares).

5.2. Time dependent relaxation of separated charge carriers at In_2S_3/CuSCN interfaces

5.2.1. Relaxation of photo-generated charge carriers in In_2S_3 layers

Dynamic properties of transport processes of photo-generated charge carriers were investigated using SPV transients. The PVD- In_2S_3 layers with varying thicknesses were photo-excited below and above the band gap using laser pulses of wavelength 700 and 420 nm, respectively. Figure 5.11 shows SPV transients from PVD- In_2S_3 layers of thicknesses of 5, 10, 20, 40 and 80 nm. Positive transients mean that photo-generated electrons (hole) were separated preferentially towards the internal (external) interface [106, 124].

The 80 nm thick layer gave the transient with the highest amplitude (230 mV) after excitation above the band gap with a 420 nm laser pulse as shown in figure 5.11 (a).

The amplitudes of the SPV transients from the 5, 10 and 20 nm thick layers were the same value of 137 mV while the 40 nm thick layer gave the lowest amplitude of 50 mV. No thickness dependence of the amplitude of SPV transients was observed for PVD-In_2S_3 layers when photo-excited above the band gap.

For excitation of PVD- In_2S_3 layers below the band gap, there was a clear thickness dependence of the SPV transient amplitude on the layer thickness. The amplitudes of the SPV transients increased with increasing layer thickness and amounted to 7, 26, 36, 80 and 124 mV for PVD- In_2S_3 layers of 5, 10, 20, 40 and 80 nm thicknesses, respectively. The distribution of exponential tails states increased with PVD- In_2S_3 layer thickness as discussed in section 5.1.1. The increase in the amplitude of SPV transient with layer thickness was due to an increase in the states below the band gap that contributed to the formation of SPV signal.

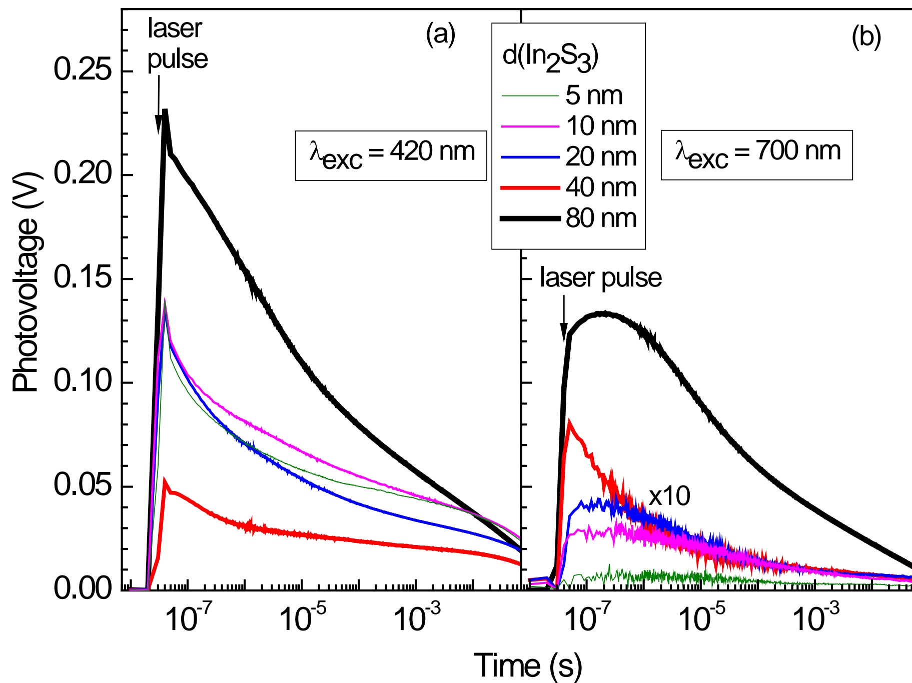

Figure 5.11: SPV transients for PVD-In_2S_3 after excitation with a laser pulse of wavelength 420 nm (a) and 700 nm (b).

The time it took a transient to decay to half the amplitude value was taken as a halftime $(\tau_{1/2})$ for that transient. The halftime of SPV transients after excitation of PVD- In_2S_3 layers above the band gap did not correlate with the layer thickness. The values of $\tau_{1/2}$

were 1.4, 7, 1.4, 24 and 7 µs for PVD- In_2S_3 layers of 5, 10, 20, 40 and 80 nm thicknesses, respectively. For excitation below the band gap, the values of $\tau_{1/2}$ decreased from 400, 110, 30 to 0.6 µs with increasing thickness from 5, 10, 20 to 40 nm, respectively. This means the SPV transients became faster with increasing layer thickness. The relaxation half time for the 80 nm thick layer was 80 µs.

5.2.2. Role of annealing temperature for relaxation of separated charge carriers at In_2S_3/CuSCN interfaces

Figure 5.12 shows SPV transients for PVD-In_2S_3/CuSCN layer systems with a 495 nm laser pulse before and after annealing at 200°C for 2 and 9 min are shown in figure 5.12. The PVD-In_2S_3 layer thicknesses were 5, 10, 20, 40 and 80 nm. The amplitudes of the SPV transients for the as-deposited PVD-In_2S_3/CuSCN layers increased with increasing PVD-In_2S_3 thickness as shown in figure 5.12 (a). The maximum of the SPV transient for the 80 nm thick sample was reached sometime after the laser pulse was switched off.

The amplitudes of the SPV transients from as-deposited PVD-In_2S_3/CuSCN amounted to 16, 39, 72, 86 and 40 mV for PVD-In_2S_3 layers of thickness 5, 10, 20, 40 and 80 nm, respectively. The half time for the SPV transient was 0.17 ms for the sample of 5 nm thicknesses but increased to 0.85, 1.1, 1.2 and 0.88 ms for layer thicknesses of 10, 20, 40 and 80 nm, respectively. After annealing for 2 min, the quality of the SPV transients changed as shown in figure 5.12 (b). A second component of the same transient was observed for the thin samples after annealing for 2 min. The amplitudes of the transients were larger than those from as-deposited PVD-In_2S_3/CuSCN layers. The SPV transient amplitudes were 138, 173, 365, 291 and 365 mV for PVD-In_2S_3 layer thicknesses of 5, 10, 20, 40 and 80 nm, respectively. Except for the 40 nm layer, the amplitudes of the transients increased with increasing layer thickness.

The values of $\tau_{1/2}$ amounted to 0,047, 0.047, 0.083, 0.088 and 1.6 µs for the transients from PVD-In_2S_3/CuSCN of layer thicknesses of 5, 10, 20, 40 and 80 nm, respectively. The relaxation times were much shorter than for the corresponding as-deposited PVD-In_2S_3/CuSCN. A negative component of the SPV transients was observed for layers of 20 nm thicknesses. The negative part was larger for the thinner layers.

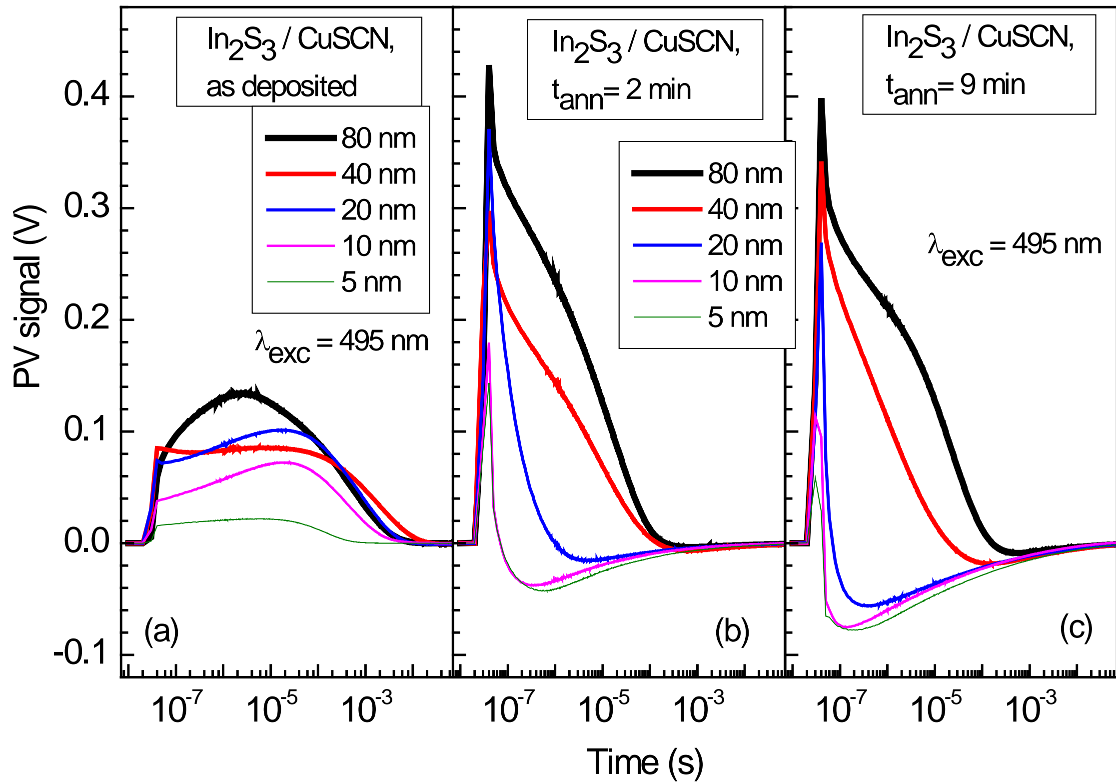

Figure 5.12: SPV transients for PVD-In_2S_3/CuSCN before (a) and after annealing for 2 (b) and 9 (c) min. Excitation was done with a laser pulse of wavelength 495 nm.

After annealing PVD-In_2S_3/CuSCN for 9 min, the amplitude of the negative component of the SPV transients increased further. The amplitude of the positive component of the transients decreased except for the 40 nm sample. The amplitudes increased with layer thickness and amounted to 54, 111, 167, 336 and 394 mV for PVD-In_2S_3 layers of thicknesses 5, 10, 20, 40 and 80 nm, respectively. The values of $\tau_{1/2}$ were 0.039, 0.040, 0.047, 0.19 and 1.6 µs for PVD-In_2S_3 layer thicknesses of 5, 10, 20, 40 and 80 nm respectively. The values of $\tau_{1/2}$ increased with increasing layer thickness but were relatively lower than those obtained after annealing PVD-In_2S_3/CuSCN for 2 min.

The positive component of the SPV transients decayed faster with annealing time while the amplitude of the negative component of the same transients increased. A SPV transient with positive (negative) amplitude characterizes preferential separation of photo-excited electrons towards the internal interface (surface). Annealing the PVD-In_2S_3/CuSCN layer system for 2 min or longer, leads to a fast relaxation of photo-

generated charges in one direction and a relatively slower relaxation in the opposite direction.

The amplitudes of the SPV transients after excitation of PVD-In_2S_3/CuSCN with laser pulses of 495 and 700 nm are given in figure 5.13 as a function of the density of Cu at the internal interface. As a remark, after annealing the PVD-In_2S_3/CuSCN layer system for 2 min or longer, the onset of SPV absorption corresponding to mobility band gap shifted to energies below 1.45 eV as discussed in section 5.1.2. Using a laser pulse of 700 nm, PVD-In_2S_3/CuSCN samples were excited above the band gap of In_2S_3:Cu.

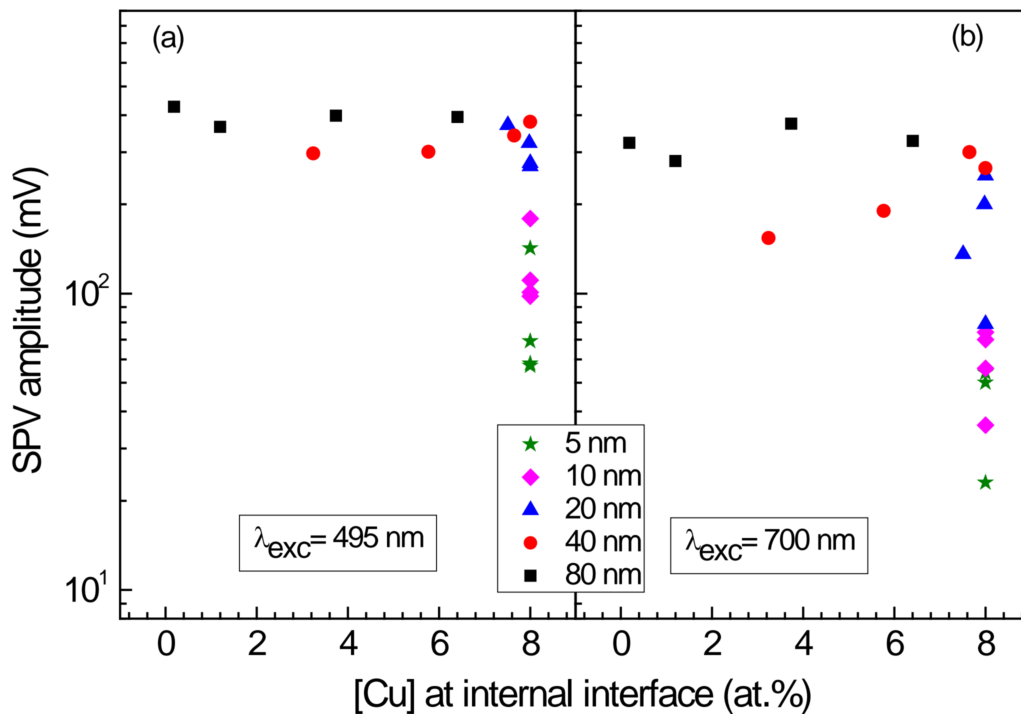

Figure 5.13. Amplitude of SPV transients for PVD-In_2S_3/CuSCN after excitation with laser pulses of wavelength of 495 nm (a) and 700 nm (b). Thickness of In_2S_3 layers was 5 (stars), 10 (diamonds), 20 (triangles), 40 (circles) and 80 nm squares. The PVD-In_2S_3/CuSCN layer system was annealed at 200°C for 2, 4, 9 and 19 min.

For PVD-In_2S_3/CuSCN with layer thicknesses of 20 nm or less, the concentration of Cu at the internal interface was close to the solubility limit on the order of 8 at.% after annealing for 2 min. The SPV amplitude dropped with increasing annealing time. For the 40 nm thick samples, the SPV amplitude after excitation with a laser pulse of 420 nm was constant, but it increased after excitation with the 700 nm laser pulse with

higher density of Cu at the internal interface. The SPV amplitude was almost constant for the PVD-In_2S_3/CuSCN with layer thickness of 80 nm independent of the concentration of Cu at the internal interface.

5.2.3. Surface photovoltage transients for PVD-In_2S_3:Cu

SPV transients for PVD-In_2S_3/CuSCN after annealing at 200°C for 19 min and for PVD-In_2S_3:Cu after annealing for 19 min and removal of CuSCN are shown in figure 5.14 for PVD-In_2S_3 layer thicknesses of 10, 20, 40 and 80 nm. The wavelength of excitation was 495 nm. The negative component of the transients disappeared from all the layers thicker than 10 nm after removal of the CuSCN layer.

For the 80 nm thick sample shown in figure 5.14 (a), the amplitude of the transient decreased slightly from 387 mV before to 367 mV after removal of CuSCN. The value of $\tau_{1/2}$ increased from 0.5 µs before to 1.3 µs after removal of CuSCN. For the 40 nm thick sample shown in figure 5.14 (b), the amplitude of the transient decreased from 380 mV before to 262 mV after removal of CuSCN while the value of $\tau_{1/2}$ increased from 0.12 µs before to 0.5 µs after removal of CuSCN layer. On the other hand, the amplitudes of the SPV transients increased from 264 and 107 mV before to 300 and 141 mV after removal of CuSCN from samples of 20 and 10 nm thicknesses shown in figure 5.14 (c) and (d), respectively. For the 20 and 10 nm thick samples, the values of $\tau_{1/2}$ increased from 0.044 and 0.037 µs before to 0.050 and 0.044 µs after removal of CuSCN layers, respectively.

In figure 5.15 the SPV transients for PVD-In_2S_3/CuSCN after annealing at 200°C for 19 min and for PVD-In_2S_3:Cu after removal of CuSCN for excitation wavelength of 700 nm are presented. The negative component of SPV transients disappeared after removal of CuSCN. The amplitudes of SPV transient decreased after removal of CuSCN from all the samples illuminated with laser pulses with a wavelength of 700 nm. The value of the SPV amplitudes were 323, 263, 78 and 36 mV for PVD-In_2S_3/CuSCN of thicknesses and 80, 40 , 20 and 10 nm, respectively. After annealing at 200°C for 19 min, the amplitudes decreased strongly to 214, 70, 50 and 15 mV for PVD-In_2S_3 layer thicknesses of 80, 40 , 20 and 10 nm, respectively. The values of $\tau_{1/2}$ amounted to 3.00, 0.76, 0.06 and 0.04 µs for PVD-In_2S_3/CuSCN after annealing at 200°C for 19 min but

increased to 12, 18, 0.24 and 0.06 μs after removal of CuSCN for layer thicknesses of 80, 40 , 20 and 10 nm, respectively.

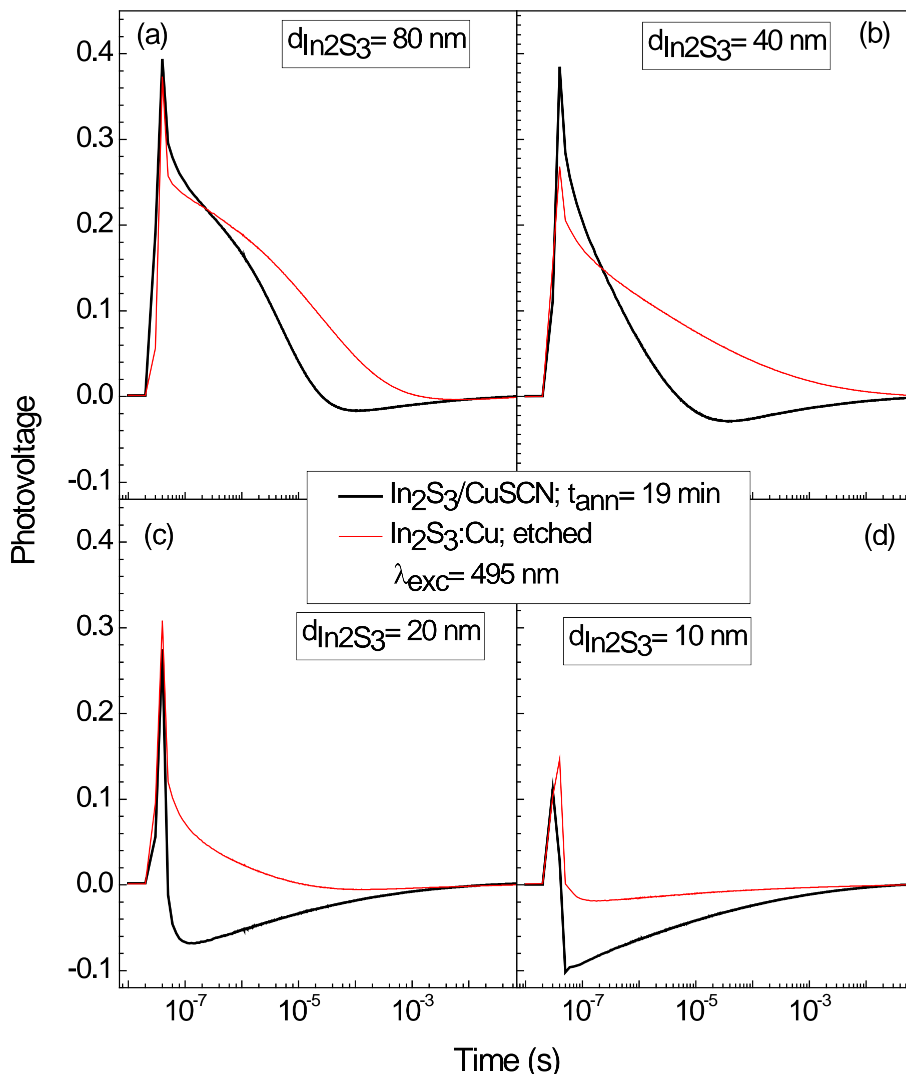

Figure 5.14: SPV transients for PVD-In_2S_3/CuSCN after annealing at 200°C for 19 min and for PVD-In_2S_3:Cu after removal of CuSCN. The laser excitation wavelength was 495 nm.

After removal of CuSCN, the SPV transients became relatively slow with charge separation only in one direction – electrons (holes) preferentially towards the internal (external) interface. It was concluded that the competing charge separation and relaxation process initiated after annealing PVD-In_2S_3/CuSCN layer system at 200°C for 2 min was eliminated or minimized after removal of CuSCN.

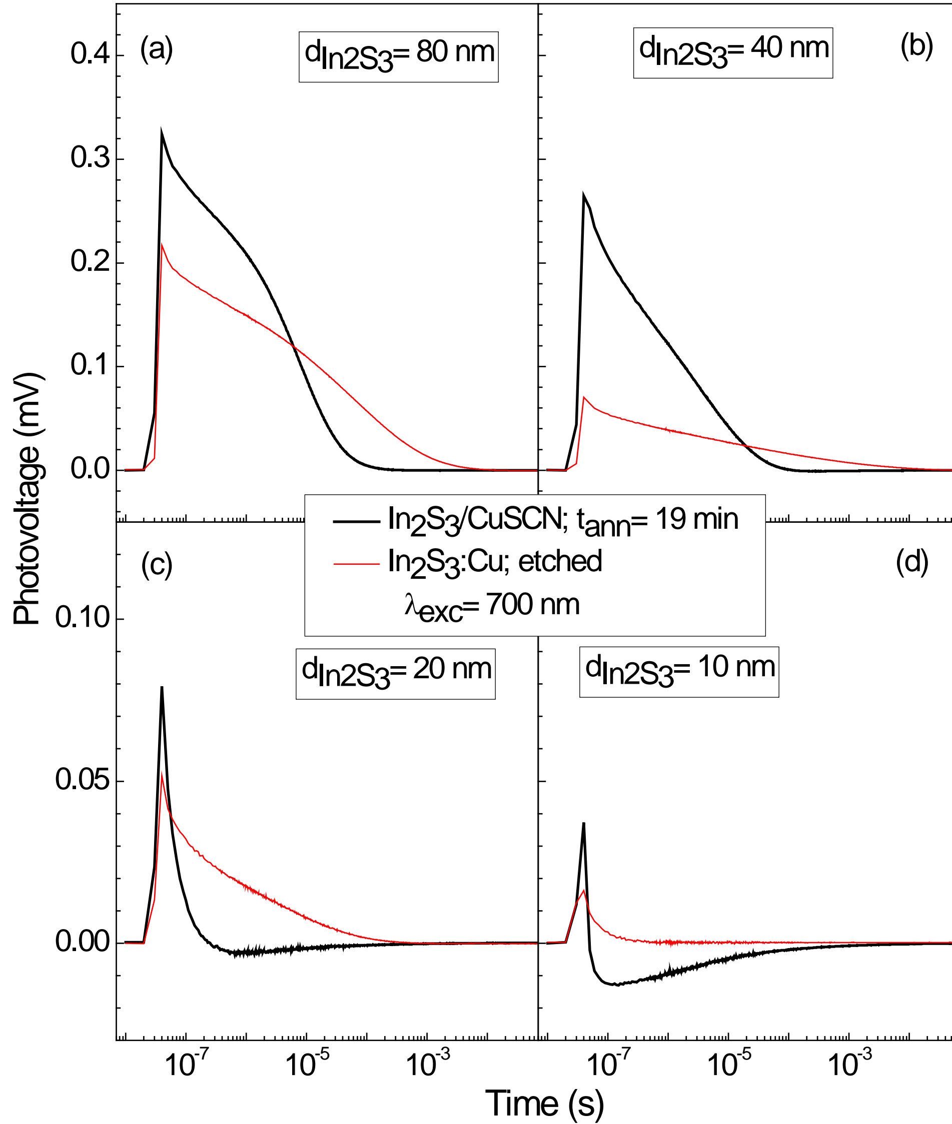

Figure 5.15: SPV transients for PVD-In_2S_3/CuSCN after annealing at 200°C for 19 min and for PVD-In_2S_3:Cu after removal of CuSCN. Laser excitation wavelength was 700 nm.

5.3. Correlation of the density of Cu at ZnO-nanorod/In_2S_3 interfaces with ZnO-nr/In_2S_3/CuSCN solar cells

According to literature, the maximum value of the open circuit voltage (V_{OC}) for ZnO-nr/In_2S_3/CuSCN solar cells based on the concept of extremely thin absorber (eta) was achieved after annealing at a temperature around 200°C for about 2 min [29]. In these solar cells, slight intermixing of In_2S_3 with Cu was beneficial for increasing the photocurrent while the nature of the In_2S_3/CuSCN heterojunction allowed for high

values of V_{OC} to be reached in the solar cells [47, 29, 13]. Diffusion of Cu to the ZnO/In_2S_3 interface was considered to be critical and was therefore not encouraged.

The values of V_{OC} obtained from reference [29] for ZnO-nr/In_2S_3/CuSCN eta solar cells annealed at different temperatures and times are plotted as a function of the concentration of diffused Cu at the ZnO/In_2S_3 interface as shown in figure 5.16. The concentrations of Cu at the ZnO/In_2S_3 interface were calculated using the diffusion constants obtained in section 4.2.1 with a CuSCN source layer and a reflecting boundary at the ZnO/In_2S_3 interface.

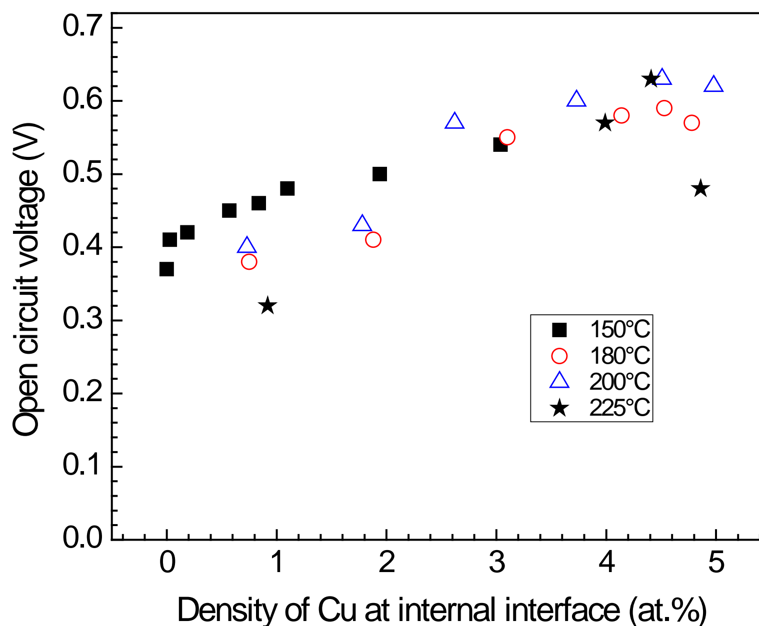

Figure 5.16: Correlation between the open circuit voltage from ZnO-nr/In_2S_3/CuSCN eta solar cell after annealing at 150°C (squares), 180°C (open circles) 200°C (open triangles) and 225°C (stars) and density of Cu at In_2S_3/ZnO interface. Values of V_{OC} were obtained from [29] and the densities of Cu at the In_2S_3/ZnO interface were calculated using diffusion constants obtained in section 4.2.1.

The highest values of V_{OC} were reached for Cu concentrations of about 4.5 at.% at the ZnO/In_2S_3 interface independent of the annealing temperature. This result confirms that an amount of Cu on the order of 4.5 at.% is required at the ZnO/In_2S_3 interface for optimal performance of ZnO-nr/In_2S_3/CuSCN eta solar cells, contrary to the suggestion by Belaidi and colleagues in [29]. The amplitudes of spectral dependent SPV signals

decreased after annealing PVD-In_2S_3/CuSCN at 200°C for 2 min or longer for layer thicknesses of 20 nm or less. The densities of Cu at the internal interface after annealing for 2 min were close the solubility limit as discussed in section 5.1.2. For layer thicknesses of 40 and 80 nm, the SPV amplitude corresponding to a Cu concentration of 4.5 at.% was close to the maximum. The energy of the tail states was lower for the 40 nm thick compared to the 80 nm thick sample. An absorber of thickness close to 40 nm can be considered suitable for the eta solar cells because of the lower disorder and higher photovoltage.

As a recommendation for improving the efficiency of ZnO-nr/In_2S_3/CuSCN eta solar cells, the CuSCN layer should be removed after annealing for short times to diffuse Cu to the ZnO-nr/In_2S_3 interface. A Cu-free hole conductor, for example an organic hole conductor, can then be deposited on top of the ZnO-nr/In_2S_3:Cu layer system to complete the solar cell.

In summary, it has been shown that the SPV amplitudes increased and the onset of the SPV absorption shifted to lower photon energies with increasing PVD-In_2S_3 layer thickness. By annealing PVD-In_2S_3/CuSCN heterojunction at 200°C for longer times, a defect band was formed near the interface which trapped positive charge and resulted in a drop in the SPV amplitude, a change in the Y signal in the modulated SPV measurements and a negative component in the SPV transients. The signal from the defect band dominated the SPV transient for thinner layers. The signal disappeared after removal of CuSCN in pyridine. The SPV results have been correlated with open circuit voltage of ZnO-nr/In_2S_3/CuSCN solar cells from literature. Contrary to what was reported in literature, we have shown that a Cu density of about 4 at.% is needed at the internal ZnO-nr/In_2S_3 interface to attain maximum V_{oc} and efficiency.

6. Charge separation across np-TiO_2/In_2S_3 interfaces

In_2S_3 layers discussed in this chapter were prepared by ILGAR from $InCl_3$ or In(acac)$_3$ precursor salts. The nature of interfaces formed between two materials depends on the deposition parameters and composition of the materials. The interface between np-TiO_2 and ILGAR-In_2S_3 was therefore investigated using modulated SPV technique to understand the role of residual Cl in ILGAR(Cl)-In_2S_3 compared to ILGAR(acac)-In_2S_3 on band alignment with np-TiO_2 substrate. The ILGAR-In_2S_3 layers were deposited at temperatures of 150, 175 and 200°C.

In this chapter, the work functions and optical band gaps of ILGAR-In_2S_3 layers are first reported followed by results from modulated SPV measurements. SPV signals from bare ILGAR-In_2S_3 and np-TiO_2/ILGAR-In_2S_3 on SnO_2:F substrates were compared to extract information about conduction band offsets at the interface. The chapter will be concluded with a model of the band diagram for the np-TiO_2/ILGAR-In_2S_3 nanocomposite. Part of the results discussed here was published in [135].

6.1. Work function analysis and optical band gap

The work functions of ILGAR(Cl)-In_2S_3 and ILGAR(acac)-In_2S_3 were obtained from the UPS spectra plotted as shown in figure 6.1. The width of the UPS spectrum is related to the work function as the difference in energy between the incident UV energy and the work function. The UV source energy is usually known from the experiment and the width of the spectrum can be obtained from the data.

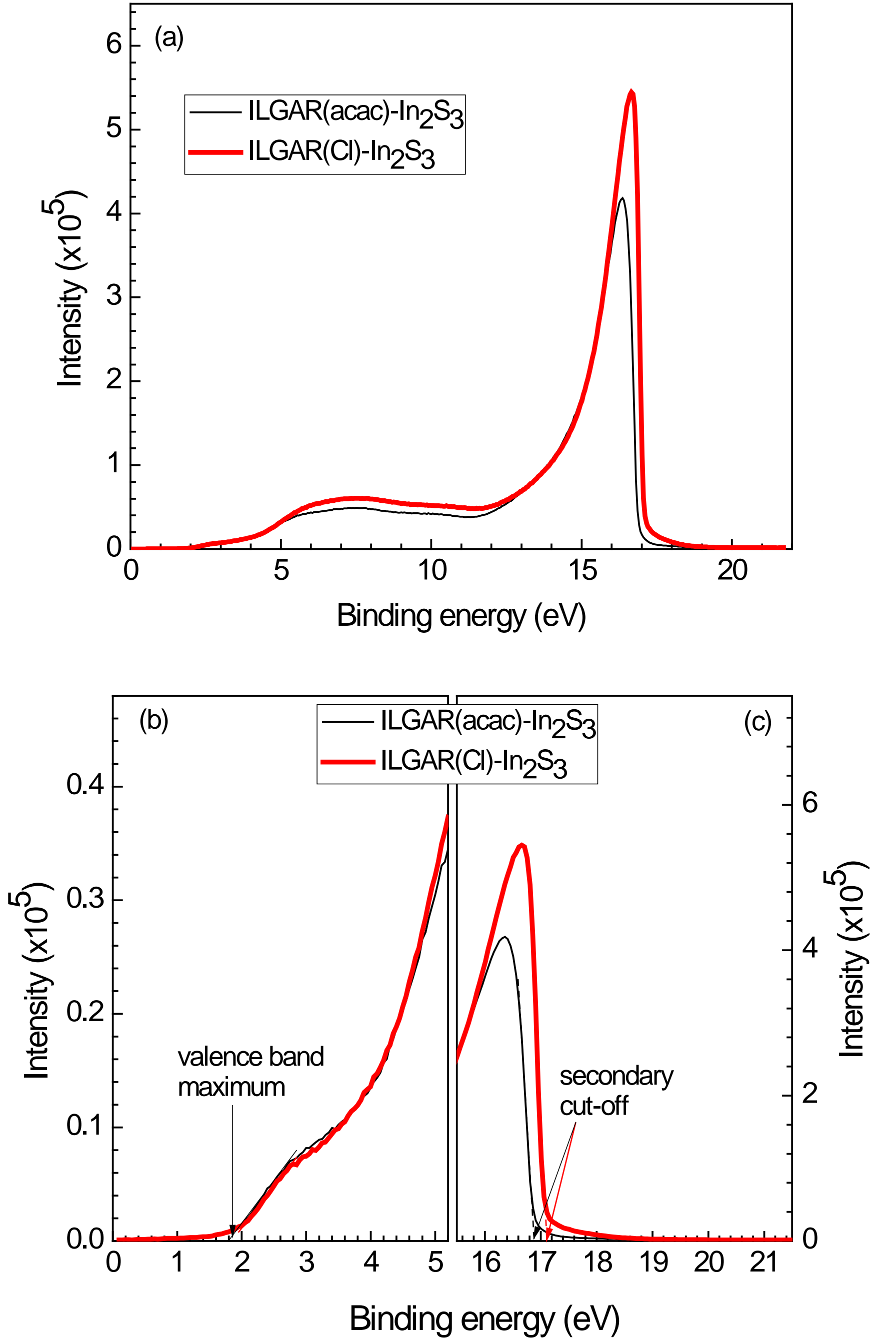

Figure 6.1: UPS spectra (a), valence band maximum (b) and secondary cut-off for ILGAR(acac)-In_2S_3 and ILGAR(Cl)-In_2S_3 layers on Mo substrates.

Figure 6.1 (a) shows how the valence band maximum was obtained as the intersection between the binding energy axis and tangent to the leading edge of the UPS spectra. The valence band maximum in relation to the Fermi level (the reference) was 1.8±0.1 and 1.9±0.1 eV for ILGAR(acac)-In_2S_3 and ILGAR(Cl)-In_2S_3, respectively. An error margin of ±0.1eV was assumed due to non-linearity of the extrapolated edges and background signal.

The work functions were obtained as the difference between the UV incident energy and the secondary cut-off shown in figure 6.1 (c). The values of the secondary cut-offs were 16.9±0.1 and 17.1±0.1 eV for ILGAR(acac)-In_2S_3 and ILGAR(Cl)-In_2S_3, respectively. Subtracting these values from the UV incident energy (22.1eV) gave work function values of 4.34±0.1 and 4.14±0.1 eV for ILGAR(acac)-In_2S_3 and ILGAR(Cl)-In_2S_3, respectively. The difference in the work functions was 0.2 eV.

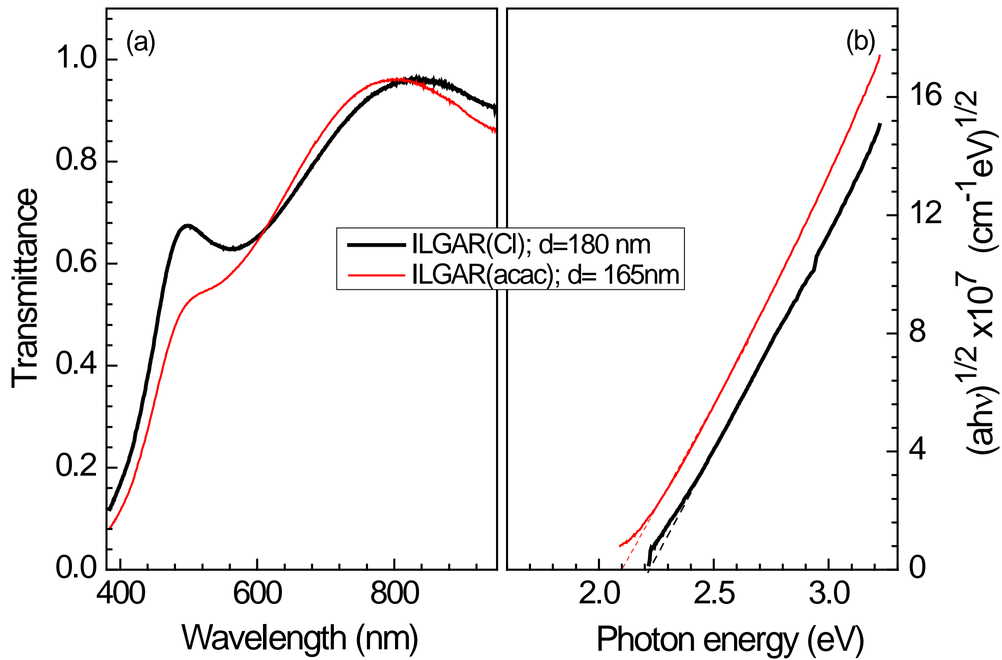

Figure 6.2: Optical transmittance and band gap for ILGAR(acac)-In_2S_3 (165 nm thick) and ILGAR(Cl)-In_2S_3 (180 nm thick) layers.

The optical band gaps of ILGAR(acac)-In_2S_3 and ILGAR(Cl)-In_2S_3 were determined from transmittance and reflectance data measured using Parkin Elmer Lambda 35 UV/vis spectrophotometer with integrating sphere. ILGAR(acac)-In_2S_3 and ILGAR(Cl)-In_2S_3 layers were found to be indirect semiconductors in agreement with literature [30]. The transmittance spectra for ILGAR(acac)-In_2S_3 and ILGAR(Cl)-In_2S_3 layers are shown in figure 6.2 (a). There was a difference in the position of the absorption edge. The band gaps (E_g) were obtained from Tauc plot of $\sqrt{\alpha.h\nu}$ against photon energy ($h\nu$), where α is the absorption coefficient, as shown in figure 6.2 (b). values of E_g amounted to 2.09 and 2.22 eV for ILGAR(acac)-In_2S_3 and ILGAR(Cl)-In_2S_3 layers, respectively.

6.2. Charge transfer across np-TiO_2/ILGAR(Cl)-In_2S_3 interface

Charge transport across semiconductor interface depends on the band alignment which in turn depends on the chemistry and composition of the interface. Twelve ILGAR cycles of ILGAR(Cl)-In_2S_3 were deposited onto screen printed np-TiO_2 at substrate temperatures of 150, 175 and 200°C. Modulated SPV amplitudes measured at a modulation frequency of 8Hz for bare ILGAR(Cl)-In_2S_3 and np-TiO_2/In_2S_3 nanocomposite are shown in figure 6.3. The spectrum of the incident photon flux from a halogen lamp is also included.

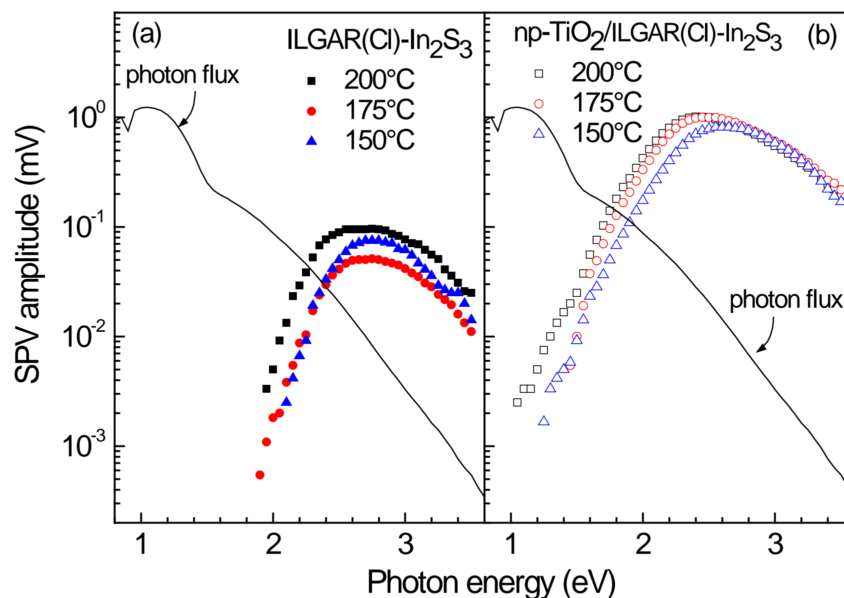

Figure 6.3: Modulated SPV amplitudes for ILGAR(Cl)-In_2S_3 (a) and np-TiO_2/ILGAR(Cl)-In_2S_3 (b). ILGAR(Cl)-In_2S_3 was deposited at temperatures of 150 (triangles), 175 (circles) and 200°C (squares).

From figure 6.3 (a) there was no dependence of the SPV amplitude on substrate temperature. The highest amplitude for bare ILGAR(Cl)-In_2S_3 on SnO_2:F was obtained for 200°C and the lowest for 175°C substrate temperatures. The magnitudes of the SPV amplitude maxima were 0.074, 0.050 and 0.096 mV for substrate temperatures of 150, 175 and 200°C, respectively. There was apparently no SPV signal detected below photon energy of 2 eV, an indication of lower defect distribution below the band gap.

Figure 6.3 (b) shows SPV amplitude for np-TiO_2/ILGAR(Cl)-In_2S_3. The SPV amplitude signal was larger compared to corresponding signals for bare ILGAR(Cl)-In_2S_3 layers. The values of the SPV amplitude maxima were 0.82, 1.00 and 1.00 mV for substrate temperatures of 150, 175 and 200°C, respectively. The SPV signal below 2 eV indicates a shift of the SPV onset energy to lower photon energies.

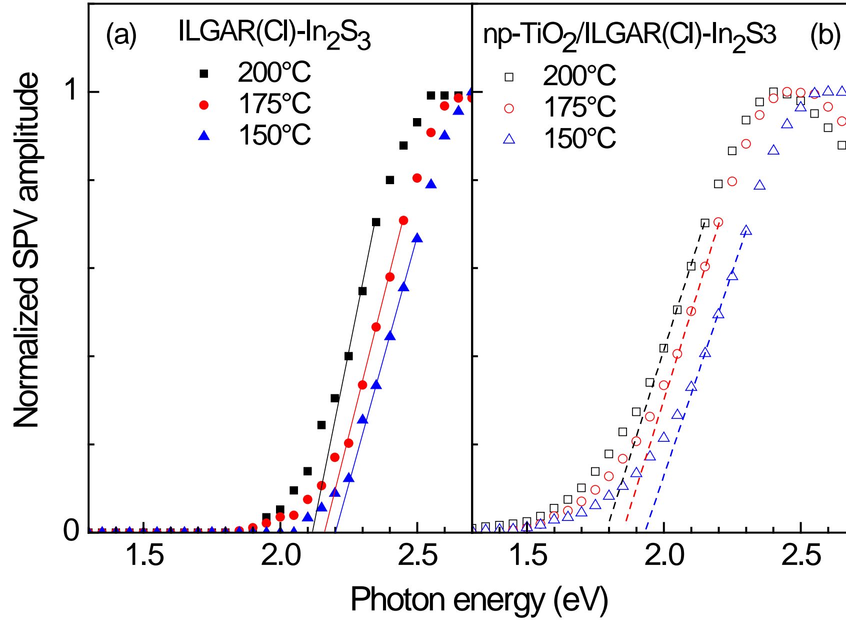

Figure 6.4: Normalized SPV amplitudes for ILGAR(Cl)-In_2S_3 (a) and np-TiO_2/ILGAR(Cl)-In_2S_3 (b). ILGAR(Cl)-In_2S_3 was deposited at temperatures of 150 (triangles), 175 (circles) and 200°C (squares).

Values of the SPV onset energies for bare ILGAR(Cl)-In_2S_3 layers and for np-TiO_2/ILGAR(Cl)-In_2S_3 nanocomposite were determined by extrapolating the leading edge of the normalized SPV signal to the photon energy axis as shown in figure 6.4. The photon energy at the intersection point gave the values of the SPV onset energy for bare ILGAR(Cl)-In_2S_3 deposited at 150, 175 and 200 °C substrate temperatures as 2.22. 2.17 and 2.11eV, respectively. These values compare well with the optical band gap of 2.21 eV obtained in section 6.1. The SPV onset energies for np-TiO_2/ILGAR(Cl)-In_2S_3 nanocomposite deposited at 150, 175 and 200°C were 1.92, 1.84 and 1.78 eV, respectively. There was a clear shift of the SPV onset energy to lower photon energies for np-TiO_2/ILGAR(Cl)-In_2S_3 compared to ILGAR(Cl)-In_2S_3 nanocomposite.

The energy parameter (E_t) of the exponential tail states describes the degree of disorder. The values of E_t were obtained from the slopes of the normalized SPV divided by the photon flux in the defect range as shown in figure 6.5. E_t values for bare ILGAR(Cl)-In_2S_3 were obtained from figure 6.5 (a) and amounted to 90, 80 and 80 meV for substrate temperatures of 150, 175 and 200°c, respectively. The degree of disorder decreased when ILGAR(Cl)-In_2S_3 was deposited at 175 or 200°C compared to 150°C.

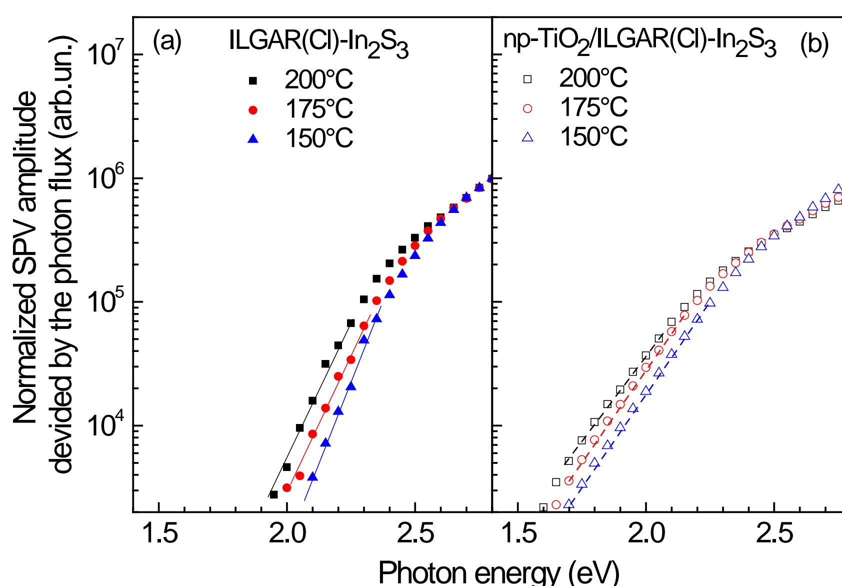

Figure 6.5: Normalized SPV amplitude divided by photon flux for ILGAR(Cl)-In_2S_3 (a) and np-TiO_2/ILGAR(Cl)-In_2S_3 (b). ILGAR(Cl)-In_2S_3 was deposited at temperatures of 150 (triangles), 175 (circles) and 200°C (squares).

Values of E_t were obtained for np-TiO_2/ILGAR(Cl)-In_2S_3 from figure 6.5 (b) as 150 meV independent of the substrate temperature. The degree of disorder increased independent of substrate temperature when ILGAR(Cl)-In_2S_3 was deposited on np-TiO_2. This can be understood by considering charge transport across np-TiO_2/ILGAR(Cl)-In_2S_3 interface. It is known that photo-generated electrons are injected from In_2S_3 into np-TiO_2 [13] therefore defect states in np-TiO_2 contributed strongly to charge separation and transport in np-TiO_2/ILGAR(Cl)-In_2S_3 nanocomposites.

Figure 6.6 shows the variation of the onset of SPV absorption and energy parameter of tail states for bare ILGAR(Cl)-In_2S_3 and np-TiO_2/ILGAR(Cl)-In_2S_3 nanocomposite as

a function of substrate temperature. There was a decrease of the SPV onset energy with increasing substrate temperature for both bare ILGAR(Cl)-In_2S_3 and np-TiO_2/ILGAR(Cl)-In_2S_3 nanocomposite. Furthermore, there was a shift of the SPV onset energy of 0.30 to 0.33 eV to lower photon energies for np-TiO_2/ILGAR(Cl)-In_2S_3 compared to bare ILGAR(Cl)-In_2S_3.

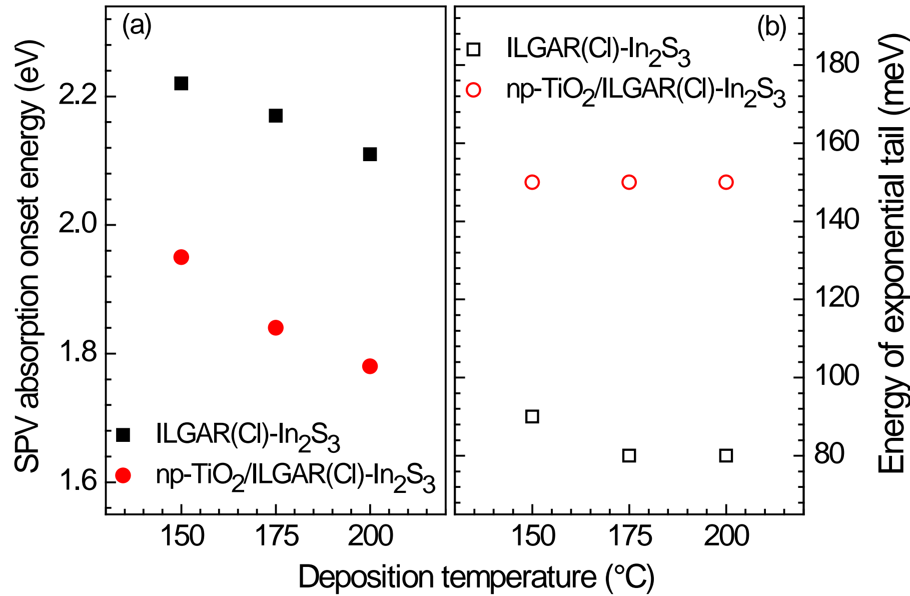

Figure 6.6: SPV absorption onset energy and energy of exponential tails for ILGAR(Cl)-In_2S_3 and np-TiO_2/ILGAR(Cl)-In_2S_3. ILGAR(Cl)-In_2S_3 was deposited at temperatures of 150 (triangles), 175 (circles) and 200°C (squares).

The difference in the onset energy between np-TiO_2 and ILGAR(Cl)-In_2S_3 was considered as the difference in the conduction band edges and not as a change in the stoichiometry of ILGAR(Cl)-In_2S_3 because the concentration of Cl remained constant in the temperature range investigated [135, 99]. A photon energy on the order of 0.33 eV less that the band gap of ILGAR(Cl)-In_2S_3 was enough to excite electrons from the valence band of ILGAR(Cl)-In_2S_3 into the conduction band or defect states below the band gap of np-TiO_2.

Figure 6.6 (b) shows the energy of tail states below the band gap for bare ILGAR(Cl)-In_2S_3 and np-TiO_2/ILGAR(Cl)-In_2S_3 nanocomposite as a function of substrate temperatures. Values of E_t decreased slightly with increasing substrate temperature for bare ILGAR(Cl)-In_2S_3 but were constant at 150 meV independent of substrate

temperature. The strong increase of E_t in np-TiO_2/ILGAR(Cl)-In_2S_3 nanocomposite compared to bare ILGAR(Cl)-In_2S_3 can be explained by the fact the distribution of defect states below the conduction band of np-TiO_2 was larger than for ILGAR(Cl)-In_2S_3 [135]. Photo-generated electrons from the valence band of ILGAR(Cl)-In_2S_3 into defect states in np-TiO_2 contributed to SPV signal at lower photon energies.

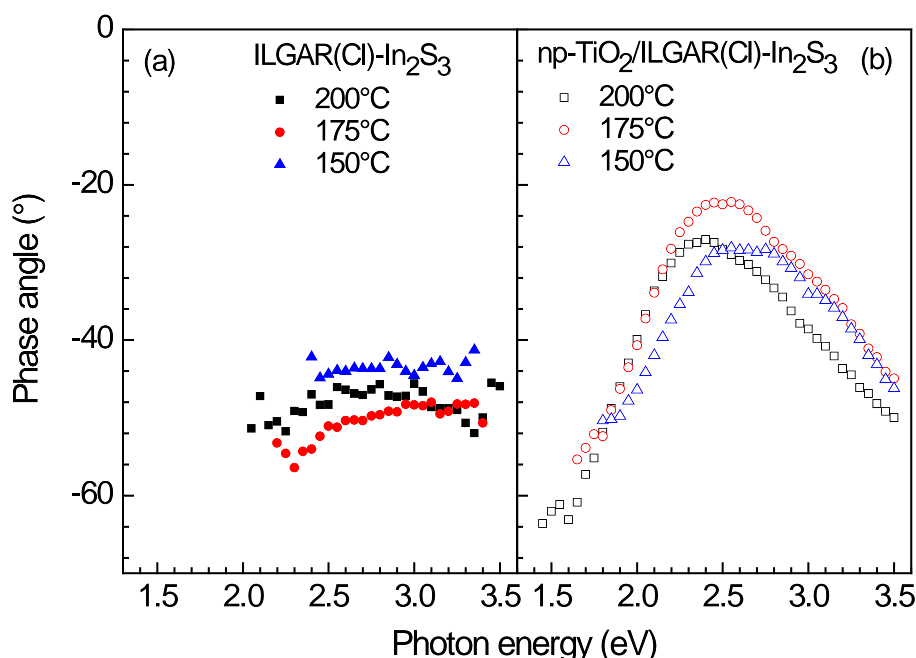

Figure 6.7: Phase angles for ILGAR(Cl)-In_2S_3 (a) and np-TiO_2/ILGAR(Cl)-In_2S_3 (b) systems. ILGAR(Cl)-In_2S_3 was deposited at temperatures of 150 (triangles), 175 (circles) and 200°C (squares).

Information about the direction of charge separation and time response of bare ILGAR(Cl)-In_2S_3 and np-TiO_2/ILGAR(Cl)-In_2S_3 nanocomposite in relation of the modulation of the incident light was obtained by analysis of the spectra of the phase angles. Figure 6.7 shows the spectra of the phase angles for bare ILGAR(Cl)-In_2S_3 and np-TiO_2/ILGAR(Cl)-In_2S_3 nanocomposite deposited at 150, 175 and 200°C substrate temperatures.

The spectra of the phase angles for bare ILGAR(Cl)-In_2S_3 were between -60° and -40 ° and did not show a significant temperature dependence. The phase angles were almost constant at -43, -50 and -46° for substrate temperatures 150, 175 and 200°C, respectively, independent of photon energy. In figure 6.7 (b), the phase angles for np-

TiO_2/ILGAR(Cl)-In_2S_3 changed from -60° to -27° for annealing temperatures of 150 and 200°C and to -22° for annealing temperature of 175°C. The change in the phase angle corroborates a change in the mechanism of charge separation and relaxation in np-TiO_2/ILGAR(Cl)-In_2S_3nanocomposite.

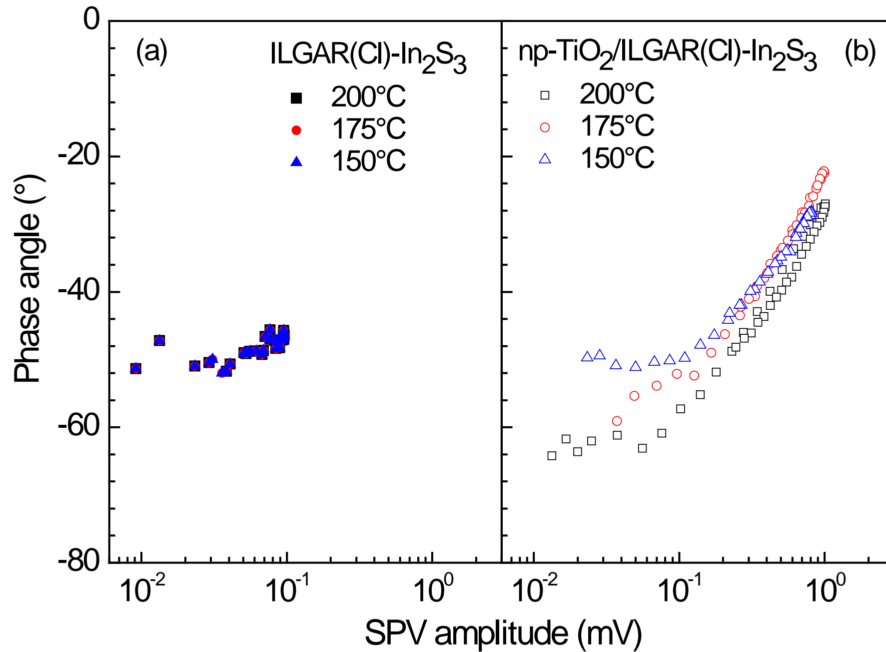

Figure 6.8: Phase angles as a function of the SPV amplitude for ILGAR(Cl)-In_2S_3 (a) and np-TiO_2/ILGAR(Cl)-In_2S_3 nanocomposite (b). ILGAR(Cl)-In_2S_3 was deposited at temperatures of 150 (triangles), 175 (circles) and 200°C (squares).

The relationship between the phase angle and the SPV amplitude is shown in figure 6.8. The phase angle was constant at -50° for bare ILGAR(Cl)-In_2S_3 independent of substrate temperature and SPV amplitude a signature of constant mechanism of charge separation and transport. Accumulation of photo-generated of electrons at the internal interface and holes at the surface caused by build-in electric field was the dominant process in ILGAR(Cl)-In_2S_3 layers.

The phase angles were almost constant for lower SPV amplitudes associated with charge separation in the defect region of np-TiO_2/ILGAR(Cl)-In_2S_3 nanocomposite. As the absorption increased above the band gap, the number of photo-generated charges increased strongly leading to an increase in the amplitude of the SPV signal. This is characteristic of trap limited transport as reported for charge transport in np-TiO_2.

Photo-generated electrons are injected from In_2S_3 into np-TiO_2, and therefore transport in np-TiO_2 dominated charge separation and relaxation in np-TiO_2/ILGAR(Cl)-In_2S_3 nanocomposite.

6.3. Charge transfer across np-TiO_2/ILGAR(acac)-In_2S_3 interface

SPV amplitudes for bare ILGAR(acac)-In_2S_3 and np-TiO_2/ILGAR(acac)-In_2S_3 nanocomposites for 150, 175 and 200°C substrate temperatures are shown in figure 6.9. Figure 6.9 (a) shows that the SPV amplitude for bare ILGAR(acac)-In_2S_3 increased from 0.10 to 0.42 to 0.78 mV with increasing substrate temperature from 150 to 175 to 200°C, respectively. There were SPV signals up to photon energies close to 1 eV due to charge separation involving defect states below the band gap of ILGAR(acac)-In_2S_3. ILGAR(acac)-In_2S_3 showed increased defect distribution below the band gap compared to ILGAR(Cl)-In_2S_3 [135].

The SPV amplitude signal increased with substrate temperature as shown in figure 6.9 and amounted to 0.53, 1.22 and 2.07 mV for substrate temperatures of 150, 175 and 200°C. The increase in the SPV amplitude signal for np-TiO_2/ILGAR(acac)-In_2S_3 nanocomposite was almost three times that from bare ILGAR(acac)-In_2S_3. There was a small change in the SPV amplitude signal at photon energy of 3.2 eV related to absorption in the np-TiO_2 layer whose band gap according to literature is 3.3 eV [142].

The SPV onset energies were determined by extrapolating the leading edge of the graph of the normalized SPV signal as shown in figure 6.10. The onset energy of the SPV signal from bare ILGAR(acac)-In_2S_3 was at 1.87 eV photon energy independent of the substrate temperature as shown in figure 6.10 (a). For comparison, the optical band for ILGAR(acac)-In_2S_3 was obtained in section 6.1 as 2.09 eV. The difference was due to the broader distribution of defects states below the band that contributed to SPV signal.

For the np-TiO_2/ILGAR(acac)-In_2S_3 nanocomposite, values the onset of SPV absorption were 1.89, 1.81 and 1.71 eV for substrate temperatures of 150, 175 and 200°C, respectively. The onset energy shifted to lower photon energies with increasing substrate temperature. As a remark, the difference in the behavior of np-

TiO_2/ILGAR(acac)-In_2S_3 and np-TiO_2/ILGAR(Cl)-In_2S_3 nanocomposites lie in the difference in chemical composition and the nature of interfaces formed.

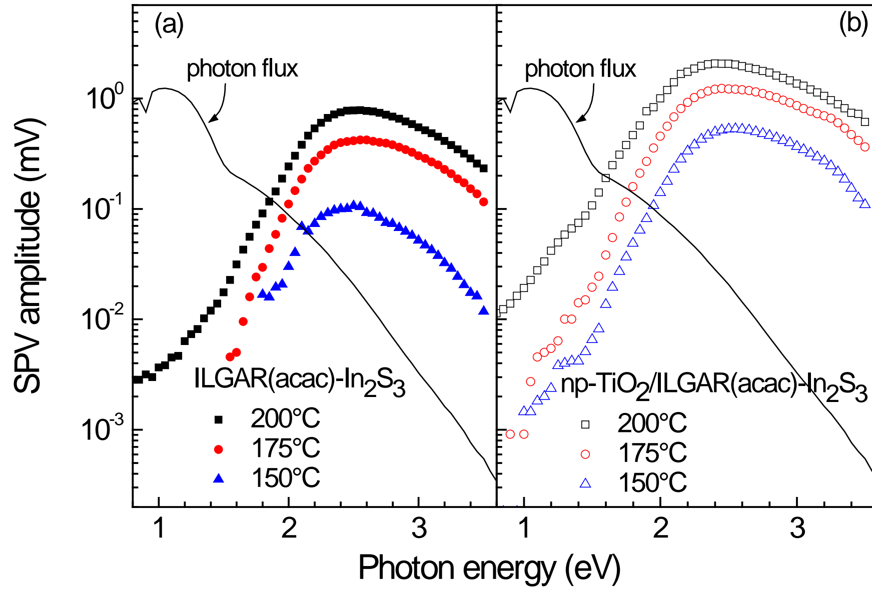

Figure 6.9: Modulated SPV amplitudes for ILGAR(acac)-In_2S_3 (a) and np-TiO_2/ILGAR(acac)-In_2S_3 (b). ILGAR(acac)-In_2S_3 was deposited at temperatures of 150 (triangles), 175 (circles) and 200°C (squares).

The energy parameters of exponential tail states were determined from the slopes of graphs of normalized SPV signals divided by the photon flux as shown in figure 6.11. The values of E_t for bare ILGAR(acac)-In_2S_3 were obtained as 120 meV for substrate temperatures of 120 and 175°C and 143 meV for substrate temperature of 200°C. This means that disorder increased for higher substrate temperatures. ILGAR(acac)-In_2S_3 showed a broader distribution of defect states below the band gap than did ILGAR(Cl)-In_2S_3. The lowest disorder, characterized by E_t, of 80 meV was realized for ILGAR(Cl)-In_2S_3. For np-TiO_2/ILGAR(acac)-In_2S_3 nanocomposite values of E_t were 135 meV after deposition at 150 and 175°C and increased to 170 meV after deposition at 200°C. The values of E_t increased for np-TiO_2/ILGAR(acac)-In_2S_3 nanocomposite compared to bare ILGAR as well as after deposition at higher temperature of 200°C [135].

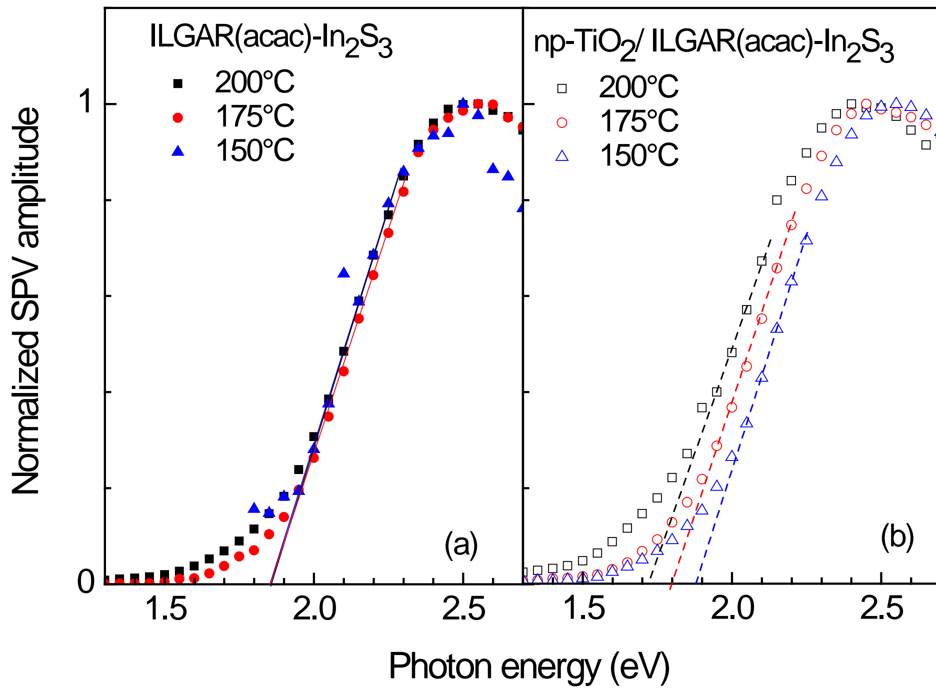

Figure 6.10: Normalized SPV amplitudes for ILGAR(acac)-In_2S_3 (a) and np-TiO_2/ILGAR(acac)-In_2S_3 (b). ILGAR(acac)-In_2S_3 was deposited at temperatures of 150 (triangles), 175 (circles) and 200°C (squares).

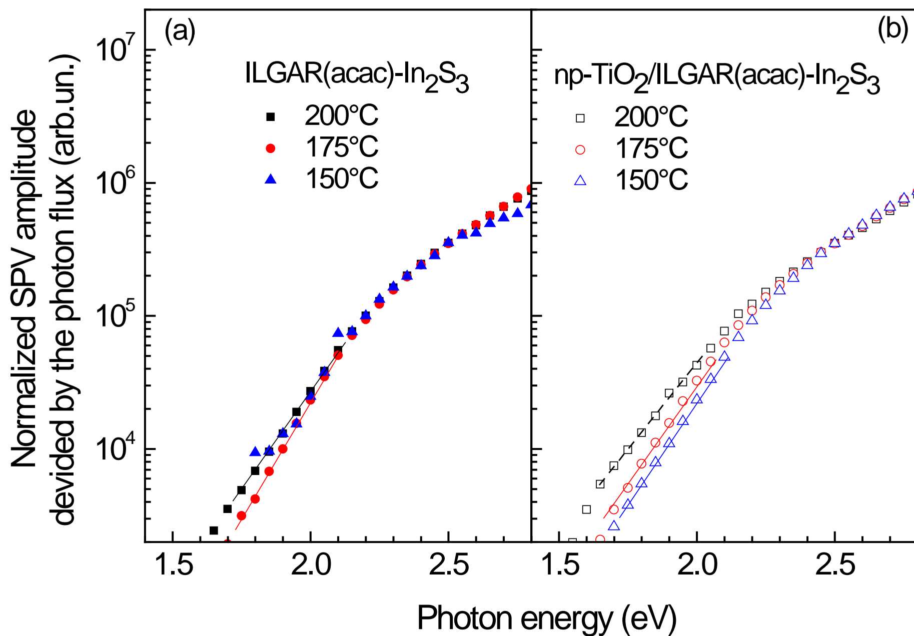

Figure 6.11: Normalized SPV amplitude divided by photon flux for ILGAR(acac)-In_2S_3 (a) and np-TiO_2/ILGAR(acac)-In_2S_3 (b). ILGAR(acac)-In_2S_3 was deposited at temperatures of 150 (triangles), 175 (circles) and 200°C (squares).

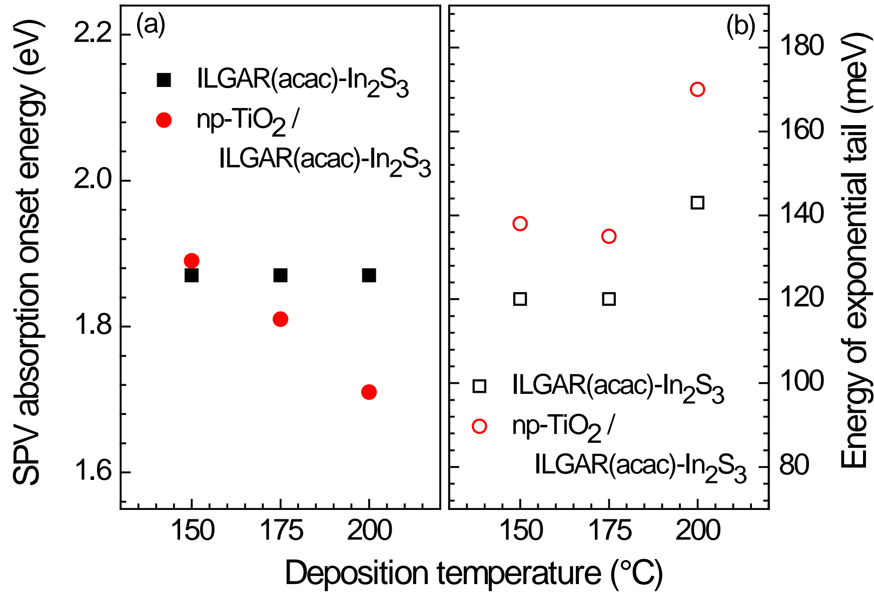

Figure 6.12: SPV absorption onset energy and energy of exponential tails for ILGAR(acac)-In_2S_3 and np-TiO_2/ILGAR(acac)-In_2S_3. ILGAR(acac)-In_2S_3 was deposited at temperatures of 150 (triangles), 175 (circles) and 200°C (squares).

Values of the SPV onset energy and E_t are shown as a function substrate temperature in figure 6.12. SPV onset energy was constant for bare ILGAR(acac)-In_2S_3 but decreased with increasing substrate temperature for np-TiO_2/ILGAR(acac)-In_2S_3 nanocomposite. On the other hand, E_t was constant for 150 and 175°C substrate temperatures but increased after deposition at 200°C. Et increased for np-TiO_2/ILGAR(acac)-In_2S_3 nanocomposite compared to bare ILGAR(acac)-In_2S_3.

Figure 6.13 shows the spectra of phase angles for bare ILGAR(acac)-In_2S_3 and for np-TiO_2/ILGAR(acac)-In_2S_3 nanocomposite, after deposition at 150, 175 and 200°C substrate temperatures. The spectra of the phase angles for bare ILGAR(acac)-In_2S_3 showed no dependence on substrate temperature as shown in figure 6.13 (a). The phase angles increased towards -0° with increasing photon energy above the band gap due to increasing absorption and generation of electron-hole pairs. The phase angles were in the range between -70° and -20° an indication that photo-generated electrons were separated preferentially towards the internal interface.

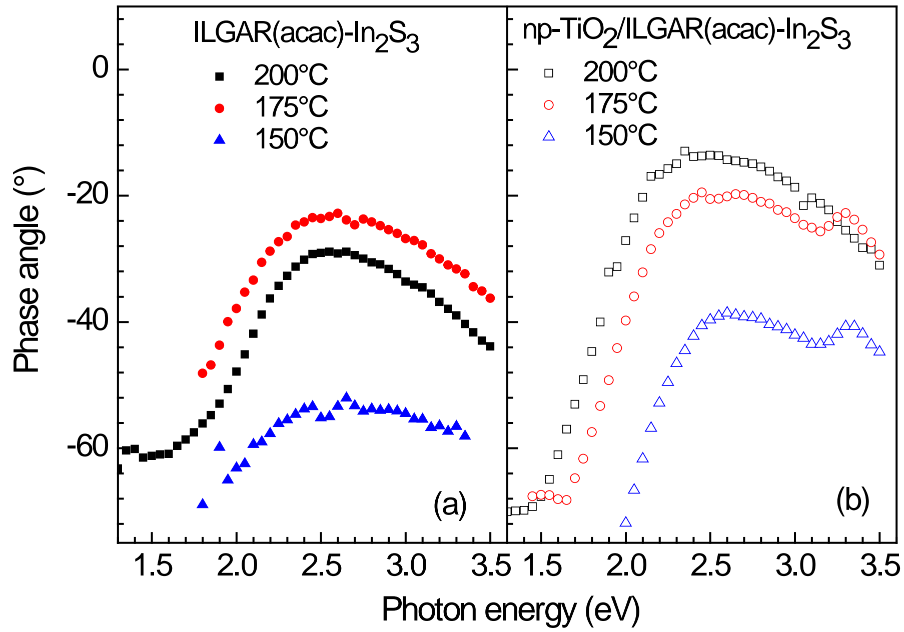

Figure 6.13: Phase for ILGAR(acac)-In_2S_3 (a) and np-TiO_2 / ILGAR(acac)-In_2S_3 (b) systems. ILGAR(acac)-In_2S_3 was deposited at temperatures of 150 (triangles), 175 (circles) and 200°C (squares).

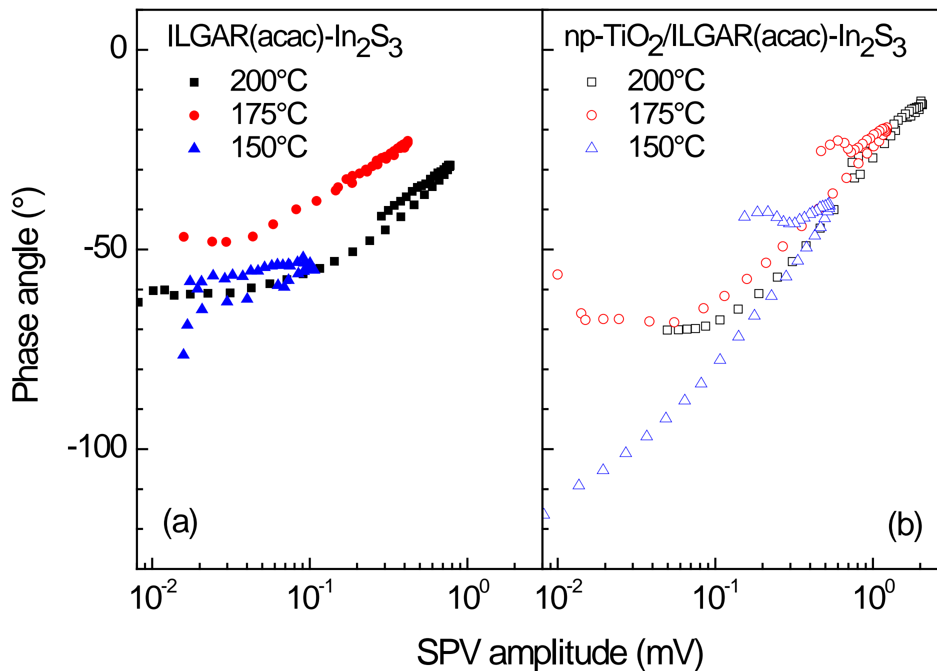

Figure 6.14: Change of phase angle with SPV amplitude for ILGAR(acac)-In_2S_3 (a) and np-TiO_2/ILGAR(acac)-In_2S_3 (b) systems. ILGAR(acac)-In_2S_3 was deposited at temperatures of 150 (triangles), 175 (circles) and 200°C (squares).

For np-TiO_2/ILGAR(acac)-In_2S_3 nanocomposites, the quality of the spectra of the phase angles was similar to those for bare ILGAR(acac)-In_2S_3. Photo-generated electrons were injected into np-TiO_2 [13]. A signal onset due to absorption in the np-TiO_2 was observed at a photon energy of about 3.2 eV. The change in the phase angle with photon energy for np-TiO_2/ILGAR(acac)-In_2S_3 nanocomposite was stronger than for bare ILGAR(acac)-In_2S_3 concomitant with the strong increase in the SPV amplitude above the absorption band edge.

The phase angle for bare ILGAR(acac)-In_2S_3 increased with SPV amplitude as shown in figure 6.14. For np-TiO_2/ILGAR(acac)-In_2S_3 nanocomposite, the phase angles increased with SPV amplitude.

6.4. Band diagram of TiO_2/In_2S_3 interface

The strong shift in the SPV onset energy and changes in E_t can be understood by considering charge transport across the np-TiO_2/ILGAR-In_2S_3 interfaces. The ionization energy and band gap of TiO_2 are known from literature to be 7.4 eV [143] and 3.3 eV [142], respectively. The conduction band of np-TiO_2 will be 0.3 eV below that of ILGAR(Cl)-In_2S_3 or 0.1 eV above that of ILGAR(acac)-In_2S_3 taking into account the mobility band gap of 2.2 and 1.9 eV, respectively, as obtained from modulated SPV measurements.

The conduction band offset of 0.3 eV for np-TiO_2/ILGAR(Cl)-In_2S_3 interface was equal to the shift in SPV onset energy. There was therefore an overlap of wave functions of occupied electronic states on the ILGAR(Cl)-In_2S_3 side and unoccupied electronic states on the np-TiO_2 side of the interface [135]. Electrons could therefore be excited with photon energies below the band gap of ILGAR(Cl)-In_2S_3 across the interface into empty states in np-TiO_2.

The shift in the SPV onset for np-TiO_2/ILGAR(acac)-In_2S_3 compared to ILGAR(acac)-In_2S_3 was about 0.05 eV but the difference in the conduction band edges was -0.1 eV or 0.1 eV taking into account the optical or mobility band gap, respectively. Considering the accuracy of the UPS measurement, the conduction band offset at the np-TiO_2/ILGAR(acac)-In_2S_3 interface was neglected [135].

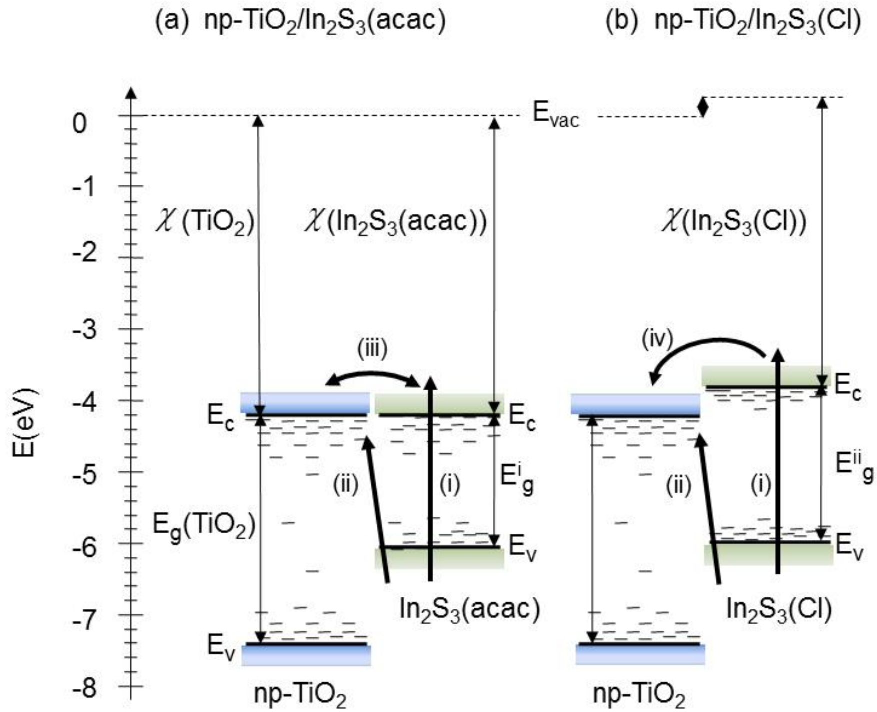

Figure 6.15: Band diagram for np-TiO_2/ILGAR(acac)-In_2S_3 (a) and np-TiO_2/ILGAR(Cl)-In_2S_3 (b) heterostructures. E_g^i and E_g^{ii} denote the band gaps of ILGAR(acac)-In_2S_3 and ILGAR(Cl)-In_2S_3, respectively and E_v and E_c are the valence and conduction band edges, respectively. $\chi(TiO_2)$, $\chi(In_2S_3(acac))$ and $\chi(In_2S_3(Cl))$ are the electron affinities for np-TiO_2, ILGAR(acac)-In_2S_3 and ILGAR(Cl)-In_2S_3, respectively.

In SPV experiments, the equilibrium voltage that depends on the rate of charging and discharging during modulation is usually measured while in UPS, the density of states is measured with reference to the Fermi energy [135]. The information depth differs but SPV has the advantage that it can measure directly charge transfer at interfaces to provide information about band alignment. There can be differences in the values of band offsets depending on the methods used.

A model of the band diagram for np-TiO_2/In_2S_3 heterostructures was developed as shown in figure 6.15. Process (i) represents photo-excitation of electrons from the valence band to the conduction band of ILGAR-In_2S_3, and process (ii) represents excitation with photon energies less than the band gap of ILGAR-In_2S_3 into states in np-TiO_2. Charge transfer across the np-TiO_2/ILGAR-In_2S_3 interface is shown by process (iii) and (iv).

In modulated SPV measurements, photo-excited electrons move back and forth across the np-TiO_2/ILGAR(acac)-In_2S_3 as shown by process (iii) due to the negligible conduction band offset. In the np-TiO_2/ILGAR(Cl)-In_2S_3 nanocomposite the back and forth motion is of photo-excited electrons is limited by the energy barrier of 0.3 eV at the interface as shown by process (iv). The interface dipole is indicated as the difference in the vacuum level at the np-TiO_2/ILGAR(Cl)-In_2S_3 interface in figure 6.15 (b). Current transport at heterojunctions depends on the composition and nature of the interface as well as the band alignment. Charge transfer across np-TiO_2/In_2S_3 interface is influenced by residual Cl which increases the band offset.

In summary, the results of charge separation in np-TiO_2/ILGAR-In_2S_3 nanocomposite have been presented. UPS measurements showed similar position for the valence band maximum for both ILGAR(acac)-In_2S_3 and ILGAR(Cl)-In_2S_3 although the optical band gap of ILGAR(Cl)-In_2S_3 is larger by 0.2 eV. The degree of disorder was minimum for ILGAR(Cl)-In_2S_3 compared to ILGAR(acac)-In_2S_3 pointing to a reduction of the distribution of band tail states due to residual Cl. A model for the energy band alignment was developed and the role of Cl discussed. The conduction band offsets amounted to 0.05 and 0.3 eV for ILGAR(acac)-In_2S_3 and ILGAR(Cl)-In_2S_3, respectively. It can be remarked that residual Cl shifted the conduction valence band upward, thereby increasing the band gap size. The nature of interfaces formed differs from each other due to difference in stoichiometry and composition.

7. Summary and outlook

Model experiments to investigate Cu diffusion from CuSCN source layer into different In_2S_3 layers and charge separation across interfaces in np-TiO_2/In_2S_3/CuSCN nanocomposite have been reported in this thesis. Diffusion experiments were performed in the temperature range between 150 and 250°C using RBS depth profiling method. Comparative analysis was performed to obtain activation energies and diffusion prefactors for Cu diffusion in PVD-In_2S_3, ILGAR(acac)-In_2S_3 and ILGAR(Cl)-In_2S_3 layers. On the other hand charge separation across PVD-In_2S_3/CuSCN and np-TiO_2/ILGAR(Cl/acac)-In_2S_3 was investigated by modulated and transient SPV techniques.

The RBS signals from diffused Cu increased with increasing annealing temperature due to enhanced diffusion of Cu into all the In_2S_3 layers. The depth profiles of Cu in In_2S_3 were extracted from the measured spectra by simulation and fitting using SPEWA software developed by the Ion beam analysis group at the Institute of Solid State Physics, University of Jena, Germany. To obtain values of the diffusion coefficients, the depth profiles were simulated using a one dimension diffusion model with a reflecting boundary.

The diffusion coefficients for Cu migration in PVD-In_2S_3 and ILGAR-In_2S_3 layers fitted well in Arrhenius plots from which the activation energies and diffusion prefactors were extracted. The diffusion prefactors of $9.0 \times 10^{-11}\ cm^2 s$ and $2.7 \times 10^{-11}\ cm^2 s$ were obtained for Cu diffusion in PVD-In_2S_3 and ILGAR(acac)-In_2S_3 layers with activation energies of 0.30 and 0.27 eV, respectively.

For the ILGAR(Cl)-In_2S_3 layers, with Cl content of 13.8 at.%, 11.3 at.%, 8.5 at.% and 7.8 at.%, the diffusion prefactors amounted to 6.0×10^{-6}, 3.0×10^{-6}, 3.2×10^{-5}, and $1.2 \times 10^{-5}\ cm^2 s$, respectively. The values of the activation energies were 0.70, 0.72, 0.75 and 0.78 eV, respectively.

The values of E_A and D_0 for Cl-free PVD- In_2S_3 and ILGAR(acac)-In_2S_3 were the same order of magnitude. E_A and D_0 values for Cl-containing ILGAR(Cl)-In_2S_3 were more than twice and five orders of magnitude higher than for Cl-free In_2S_3 layers, respectively. The relationship between E_A and D_0 satisfied the Meyer-Neldel compensation law with the Meyer-Neldel energy (40 meV) in the range of 25 -250 meV reported in literature. This corresponds to the isokinetic temperature of 191°C, which is close to the average temperature for the experimental range covered in this work.

The onset of the modulated-SPV absorption for PVD-In_2S_3 layers decreased to lower photon energies while the amplitude of the SPV signal increased with increase in layer thickness. After deposition of CuSCN, the onset of SPV absorption shifted to lower photon energies and the amplitude increased by almost twice for all layer thicknesses. After annealing PVD-In_2S_3/CuSCN heterostructures the amplitude of the SPV signal increased for short annealing times but decreased for prolonged annealing. The decrease was stronger for thinner In_2S_3 layers. SPV transients were positive, denoting charge separation with photogenerated electrons separated preferentially towards the internal interface. The SPV transients showed a negative component of the same transient after annealing for longer than 2 min. This means that a second process of charge separation in the opposite direction was initiated after annealing due to the formation of a defect band where hole are trapped.

The density of diffused Cu at the internal (ZnO-nr/In_2S_3) interface of a ZnO-nr/In_2S_3/CuSCN solar cell with absorber thickness of 30 nm was calculated as a function of annealing times. Comparison of the SPV results with open circuit voltages of the solar cell led to the conclusion that the optimal layer thickness for these kinds of solar cells is in the range of 30 – 40 nm. A density of Cu of 4 - 4.5 at.% is necessary at the ZnO/In_2S_3 interface of the solar cell for optimal performance contrary to what is found in literature. This is achieved after annealing the complete solar cell at 200°C for about 2 min.

It is therefore recommended that, to achieve higher conversion efficiencies, the CuSCN layer should be removed after annealing the ZnO-nr or TiO_2/In_2S_3/CuSCN solar cells at 200°C for about 2 min and a Cu-free hole conductor, for example an organic semiconductor, is deposited onto the ZnO-nr or TiO_2/In_2S_3:Cu heterostructure. The ZnO-nr/In_2S_3/CuSCN remained stable for close to about two month when stored in air

after moderate annealing [144]. In this time the efficiency of the solar cells increased and started to drop after about two months. The stability of the solar cells will be enhanced because the continuous diffusion that eventually degrades the solar cells will be eliminated by removal of the CuSCN layer after annealing.

The band alignment at np-TiO_2/ILGAR-In_2S_3 interface was investigated by modulated SPV technique as a function of the ILGAR precursor salt. Cl-free and Cl-containing In_2S_3 layers from In(acac)$_3$ and $InCl_3$ precursor salts, respectively, were deposited on SnO_2:F and np-TiO_2 substrates by ILGAR method at substrates temperatures of 150, 175 and 200°C. The optical band gap of ILGAR(Cl)-In_2S_3 and ILGAR(acac)-In_2S_3 was 2.22eV and 2.09 eV while the work function amounted to 4.14 and 4.34 eV, respectively. ILGAR(acac)-In_2S_3 showed the highest degree of disorder with higher energy parameter of tail states (E_t) compared to ILGAR(Cl)-In_2S_3. The shift in the onset of the SPV absorption to lower photon energies for np-TiO_2/ILGAR-In_2S_3 compared to SnO_2:F/ILGAR-In_2S_3 was interpreted as the difference in the conduction band edges between np-TiO_2 and ILGAR-In_2S_3. The conduction band offsets for np-TiO_2/ILGAR(Cl)-In_2S_3 and np-TiO_2/ILGAR(acac)-In_2S_3 were 0.30 eV and 0.05 eV, respectively.

Charge transport in the np-TiO_2/In_2S_3 nanocomposites showed characteristics of a trap limited mechanism. This means that the photogenerated electrons were injected into np-TiO_2 and therefore electron transport in the np-TiO_2 layer was the dominant process. It is known that electronic transport in np-TiO_2 is predominantly trap assisted, and it is explained using the trap filling concept. A model for the energy band alignment was proposed based on the band offsets, work function and band gap values. The difference on the conduction band offsets at the np-TiO_2/ILGAR(acac)-In_2S_3 and np-TiO_2/ILGAR(Cl)-In_2S_3 interfaces points to different interface properties and band line up. Cl ion carries a negative charge which modifies the interface dipole different from the Cl-free case.

First principle calculations of the structural and electronic properties of Cl-containing In_2S_3 will be helpful in understanding the role of Cl for interface formation and for Cu diffusion mechanisms. Understanding the role of Cl for the formation of charge selective contacts in np-TiO_2/In_2S_3/CuSCN requires systematic variation of Cl content in the In_2S_3 layers starting with very small amounts. This requires the optimization of

deposition parameters in the ILGAR process. This knowledge is beneficial also for the chalcopyrite solar cell community, which use In_2S_3 as a buffer layer between the chalcopyrite absorber and window layer. Extended investigations of charge separation in complete np-TiO_2/In_2S_3/CuSCN nanocomposites are required to understand processes of electronic transport in the whole system.

8. References

[1] V. Quaschning, Understanding Renewable Energy systems, London: Carl Hanser Verlag, 2005.

[2] S. Kim, J.-W. Chung, H. Lee, J. Park, Y. Heo and H.-M. Lee, "Remarkable progressin thin film silicon solar cells using high efficiency triple-junction technology," *Solar energy materials & solar cells,* vol. in press, 2013.

[3] D. Jordan and S. Kurtz, "Photovoltaic degradation rates - An analytical review," *Prog. Photovolt: Res. Appl.,* vol. 21, pp. 12-29, 2012.

[4] H. Musikowski and A. Styczynski, "Analysis of the operational behavior and long-term performance of a CIS PV system.," in *Proceedings of the 25th European Photovoltaic Solar Energy Conference*, Valencia, Spain., 2010.

[5] E. Becquerel, *Comptes Rendus,* vol. 9, p. 561, 1839.

[6] R. Ohl, "Light-sensitive electric device". Bell Telephone Laboratories, USA Patent US2402662 A, 25 June 1946.

[7] D. Dimova-Malinovska, "The state-of-the-art and future development of the photovoltaic technologies – the route from crystalline to nanostructured and new emerging materials," *J. Phys.: Conf. Ser.,* vol. 253, p. 012007, 2010.

[8] J. Bragagnolo, A. Barnett, J. Phillips, R. Hall, A. Rothwarf and J. Mearkin, "The design and fabrication of thin-film CdS/Cu2S Cells of 9.1 5-percent conversion

efficiency," *IEEE Trans. Electron. Dev.,* Vols. ED-27, pp. 645-650, 1980.

[9] P. Jackson, D. Hariskos, E. Lotter, S. Paetel, R. Wuerz, R. Menner, W. Wischmann and M. Powalla, "New world record efficiency for Cu(In,Ga)Se2 thin-film solar cells beyond 20%," *Prog. Photovolt: Res. Appl. ,* vol. 19, pp. 894-897, 2011.

[10] FirstSolar, "First Solar Sets New World Record for CdTe Solar Cell Efficiency," First Solar Inc., Ohio, February, 2013.

[11] T. Dittrich, A. Belaidi and A. Ennaoui, "Concepts of inorganic solid-state nanostructured solar cells," *Solar Energy Materials & Solar Cells,* vol. 95, pp. 1527-1536, 2011.

[12] J. Burschka, N. Pellet, S.-J. Moon, R. Humphry-Backer, P. Gao, M. Nazeeruddin and M. Graetzel, "Sequential deposition as a route to high-performance perovskite-sensitized solar cells," *Nature,* vol. 499, pp. 316-319, 2013.

[13] C. Herzog, A. Belaidi, A. Ogacho and T. Dittrich, "Inorganic solid state solar cell with ultra-thin nanocomposite absorber based on nanoporous TiO2 and In2S3," *Energy Environ. Sci.,* vol. 2, pp. 962-964, 2009.

[14] J. Moeller, C.-H. Fischer, S. Siebentritt, R. Koenenkamp and M. LuxSteiner, "CuInS2 as an extremely thin absorber in an eta solar cell," *Proceedings of the 2nd World Conference on Photovoltaic Solar Energy,* vol. 1, pp. 209-211, 1998.

[15] A. Belaidi, R. Bayón, L. Dloczik, K. Ernst, M. Lux-Steiner and R. Könenkamp, "Comparison of different thin film absorbers used in eta-solar cells," *Thin Solid Films,* Vols. 431-432, pp. 488-491, 2003.

[16] R. Bayon, R. Musembi, A. Belaidi, M. Baer, T. Guminskaya, C.-H. Fischer, M.-C. Lux-Steiner and T. Dittrich, "Highly structured TiO2/In(OH)xSy/PbS/PEDOTSS to be used in photovoltaic applications," *C.R. Chimie,* vol. 9, pp. 730-734, 2006.

[17] G. Larramona, C. Chone, A. Jacob, D. Sakakura, B. Delatouche, D. Pere, X. Cieren, M. Nagino and R. Bayon, "Nanostructured solar cells of the type titanium dioxide, cadmuim sulfide thin coating and copper thiocyanate showing high quantum efficiency," *Chem.Mater.,* vol. 18, pp. 1688-1696, 2006.

[18] M. Nanu, J. Schoonman and A. Goosens, "Inorganic nanocomposites of n- and p-semiconducotors: a new type of three dimensional solar cell," *Adv. Mater.,* vol. 16, pp. 453-456, 2004.

[19] A. Pattantyus-Abraham, I. Kramar, A. Barkhouse, X. Wang, G. Konstantatos, R. Depnath, L. Levina, I. Raabe, M. Nazeeruddin, M. Graetzel and E. Sargent, "Depleted-Heterojunction Colloidal Quantum Dot Solar Cells," *ACS Nano,* vol. 4, p. 3374–3380, 2010.

[20] H. Hsieh, "The effect of Cu diffusion in a Cu2S/CdS heterojunction solar cell," *J. Appl. Phys.,* vol. 53, no. 3, pp. 1727-1733, 1982.

[21] W. Gull and R. Bube, "Photovoltaic properties of Cu2S-CdS heterojunctions," *J. Appl. Phys.,* vol. 41, no. 9, pp. 3731-3738, 1970.

[22] T. Dittrich, D. Kieven, A. Belaidi, M. Rusu, J. Tornow, K. Schwarzburg and M. Lux-Steiner, "Formation of charge selective contacts in solar cells with extrememly thin absorber based on ZnO-nr/In2S3/CuSCN," *J. Appl. Phys.,* vol. 105, p. 034509, 2009.

[23] D. Abou-Ras, D. Rudmann, G. Kostorz, S. Spiering, M. Powalla and A. Tiwari, "Microstructural and chemical studies of interfaces between Cu(In,Ga)Se2 and In2S3 layers," *J. Appl. Phys. ,* vol. 97, p. 084908, 2005.

[24] M. Rusu, T. Glatzel, A. Neisser, C. Kaufmann, S. Sadewasser and M. Lux-Steiner, "Formation of the physical vapor deposited CdS/Cu(In,Ga)Se2 interface in highly efficient thin film solar cells," *Appl. Phys. Lett.,* vol. 48, p. 143510, 2006.

[25] M. Baer, A. Ennaoui, J. Klaer, T. Kropp, R. Saéz-Araoz, S. Lehman, A. Grimm, I.

Lauermann, C. Loreck, S. Sokoll, H.-W. Schock, C.-H. Fischer and M. Lux-Steiner, "Intermixing at the heterointerface between ZnS/Zn(S,O) bilayer buffer and CuInS2 thin film solar cell absorber," *J. Appl. Phys.,* vol. 100, p. 064911, 2006.

[26] M. Baer, N. Barreau, F. Couzinié-Devy, S. Pookpanratana, J. Klaer, M. Blum, Y. Zhang, J. Denlinger, H.-W. Schock, L. Weinhardt, J. Kessler and C. Heske, "Nondestructive depth-resolved spectroscopic investigation of the heavily intermixed In2S3/Cu(In,Ga)Se2 interface," *Appl. Phys. Lett.,* vol. 96, no. 18, p. 184101, 2010.

[27] L. Kranz, C. Gretener, J. Perrenoud, R. Schmitt, F. Pianezzi, F. La Mattina, P. Bloesch, E. Cheah, A. Chirilá, C. Fella, H. Hagendorfer, T. Jaeger, S. Nishiwaki, A. Uhl, S. Buescheler and A. Tiwari, "Doping of polycrystalline CdTe for high-efficiency solar cells on flexible metal foil," *Nature Communications,* p. DOI: 10.1038/ncomms3306, 2013.

[28] Z. Hameiri, K. McIntosh and G. Xu, "Evaluation of recombination processes using the local ideality factor of carrier lifetime measurements," *Sol. Energy Mater. & Solar cells,* vol. 117, pp. 251-258, 2013.

[29] A. Belaidi, T. Dittrich, D. kieven, J. Tornow, K. Schwarzburg, M. Kunst, N. Allsop, M.-C. Lux-Steiner and S. Gavrilov, "ZnO-nanorod arrays for solar cells with extremely thin sulfidic absorber," *Solar Energy Materials & Solar Cells,* vol. 93, pp. 1033-1036, 2009.

[30] N. Barreau, "Indium sulfide and relatives in the world of photovoltaics," *Solar Energy,* vol. 83, pp. 363-371, 2009.

[31] H. Mehrer, Diffusion in solids: Fundamentals, methods, materials, diffusion-controlled processes, Berlin: Springer-verlag Berlin Heidelberg, 2007.

[32] P. Kofstad and T. Norby, Defects and transport in crystalline solids, Oslo, Norway.: University of Norway, 2007.

[33] F. Frank and D. Turnbull, "Mechanism of Diffusion of Copper in Germanium," *Phys. Rev.,* vol. 104, no. 3, pp. 617-618, 1956.

[34] R. Hall and J. Racette, "Diffusion and Solubility of Copper in Extrinsic and Intrinsic Germanium, Silicon, and Gallium Arsenide.," *J. Appl. Phys.,* vol. 35, no. 2, pp. 379-397, 1964.

[35] A. Istratov and E. Weber, "Physics of Copper in silicon," *J. Electrochem. Soc.,* vol. 149, no. 1, pp. G21-G30, 2001.

[36] J. Doyle, A. Kuznetsov and B. Svensson, "Copper diffusion in amorphous germanium," *J. Vac. Sci. Technol. A. ,* vol. 16, no. 4, p. 2604.2607, 1998.

[37] G. Sullivan, "DifFusion and solubility of Cu in C18 Single Crystals," *Phys. Rev.,* vol. 184, pp. 796-805, 1969.

[38] J. McBrayer, R. Swanson and T. Sigmon, "Diffusion of Metals in Silicon Dioxide," *J. Electrochem. Soc. ,* vol. 133, no. 6, pp. 1242-1246, 1986.

[39] A. Juma, P. Pistor, S. Fengler, T. Dittrich and E. Wendler, "Copper diffusion in thin In2S3 layers investigated by Rutherford Backscattering Spectroscopy," *Thin Solid Films,* vol. 520, pp. 6740-6743, 2012.

[40] F. Py, M. Womes, J. Durand, J. Oliver-Fourcade, J. Jumas, J. Esteva and R. Karnatak, "Copper in In2S3: a study by x-ray diffraction, diffuse reflectance and x-ray absorption," *J.Alloys and compounds,,* vol. 178, no. 1-2, pp. 297-304, 1992.

[41] C. Guillot-Deudon, S. Harel, A. Mokrani, A. Lafond, N. Barreau, V. Fernandez and J. Kessler, "Electronic structure of NaxCu1−xIn5S8 compounds: X-ray photoemission spectroscopy study and band structure calculations," *Phys. Rev.,* vol. 78, p. 235201, 2008.

[42] D. Abou-Ras, G. Kostorz, A. Strohm and A. Tiwari, "Interfacial layer formations between Cu(In,Ga)Se2 and InxSy layers," *J. Appl. Phys. ,* vol. 98, p. 123512, 2005.

[43] M. Demtsu, D. Albin and J. Sites, "Role of copper in the performance of CdS/CdTe solar cells," in *4th IEEE World conference on photovoltaic energy conversion (WCPEC-4)*, Waikoloa, Hawaii, May 7-12, 2006.

[44] T. Gessert, W. Metzger, P. Dippo, S. Asher, R. Dhere and M. Young, "Dependence of carrier lifetime on Cu-contacting temperature and ZnTe:Cu thickness in CdS/CdTe thin film solar cells," *Thin Solid Films,* vol. 517, pp. 2370-2373, 2009.

[45] J. Wilson and J. Woods, "Photovoltaic properties of single-crystal CdS-Cu2S cells," *J. Phys: D,* vol. 5, pp. 1700-1711, 1972.

[46] T. Dittrich, D. Kieven, M. Rusu, A. Belaidi, J. Tornow, K. Schwarzburg and M. Lux-Steiner, "Current-voltage characteristics and transport mechanism of solar cells based on ZnO nanorods/In2S3/CuSCN," *Appl. Phys. Lett.,* vol. 93, p. 053113, 2008.

[47] T. Dittrich, D. Kieven, M. Rusu, A. Belaidi, J. Tornow, K. Schwarzburg and M. Lux-Steiner, "Current-voltage characteristics and transport mechanism of solar cells based on ZnO nanorods/In2S3/CuSCN," *Appl. Phys. Lett.,* vol. 93, no. 5, p. 053113, 2008.

[48] R. Diehl and R. Nitsche, "Vapour growth of three In2S3 modifications by iodine transport," *J. Cryst. Growth.,* vol. 28, pp. 306-310, 1975.

[49] C. Rooymans, "A new type of cation-vacancy ordering in the spinel lattice of In2S3," *J. Inorg. Nucl. Chem.,* vol. 11, pp. 78-79, 1959.

[50] A. Lafond, C. Guillot-Deudon, S. Harel, A. Mokrani, N. Barreau, S. Gall and J. Kessler, "Structural study and electronic band structure investigations of the solid solution NaxCu1 − xIn5S8 and its impact on the Cu(In,Ga)Se2/In2S3 interface of solar cells," *Thin Solid Films,* vol. 515, pp. 6020-6023, 2007.

[51] N. Barreau and M. Tessier, "Characterization of indium sulfide thin films containing copper," *MRS Proceedings,* vol. 1165, pp. M08-21, 2009.

[52] G. Boisvert, L. Lewis and A. Yelon, "Many-body nature of the Meyer-Neldel compensation law for diffusion," *Phys. Rev. Lett.,* vol. 75, no. 3, pp. 469-472, 1995.

[53] A. Yelon, B. Movaghar and H. Branz, "Origin and consequences of the compensation (Meyer-Neldel) law," *Phys. Rev. B,* vol. 46, no. 19, pp. 12244-12250, 1992.

[54] D. Dustan, "The role of experimental error in Arrhenius plots: Self diffusion in semiconductors," *Solid state communications,* vol. 107, no. 4, pp. 159-163, 1998.

[55] R. Widenhorn, M. Fitzgibbons and E. Bodegon, "The Meyer-Neldel rule for diodes in forward bias," *J. Appl. Phys.,* vol. 96, no. 12, pp. 7379-7382, 2004.

[56] R. Kirchheim and X. Huang, "A Relationship between prefactor and activation energy for diffusion.," *phys. stats. sol (b),* vol. 144, pp. 253-257, 1987.

[57] P. Mialhe, J. Charles and A. Khoury, "The thermodynamic compensation law," *J. Phys. D: Appl. Phys.,* vol. 21, pp. 383-384, 1988.

[58] K. Shimakawa and M. Aniya, "Dynamics of atomic diffusion in condensed matter: origin of the Meyer–Neldel compensation law," *Monatsh Chem,* vol. 144, pp. 67-71, 2013.

[59] A. Yelon and B. Movaghar, "Microscopic explanation of the compensation (Meyer-Neldel) rule," *Phys. Rev. Lett.,* vol. 65, no. 5, p. 618620, 1990.

[60] H. Overhof and P. Thomas, Electronic transport in hydrogenated amorphous semiconductors, Berlin: Springer, 1989.

[61] R. Crandall, "Defect relaxation in amorphous silicon: Stretched exponentials, the Meyer-Neldel rule and the Staebler-Wronski effect," *Phys. Rev. B,* vol. 43, pp. 4057-4070, 1991.

[62] J. Singh, Electronic and optoelectronic properties of semiconductor structures, New York: Cambridge University press, 2003.

[63] M. Ansari-Rad, J. Anta and J. Bisquert, "Interpretation of diffusion and recombination in nanostructured and energy-disordered materials by stochastic quasiequilibrium simulation.," *J. Phys. Chem. C,* vol. 117, pp. 16275-16289, 2013.

[64] S. Baranovski and O. Rubel, "Description of Charge Transport in Amorphous Semiconductors," in *Charge transport in disordered solids with applications in electronics*, R. Baranovski, Ed., West Sussex, England, John Wiley & Sons ltd, 2006, pp. 49-93.

[65] R. Schwarz, "Dispersive transport in disordered semiconductors," *J. Non-cryst. Solids,* Vols. 227-230, pp. 148-152, 1998.

[66] T. Tiedje and A. Rose, "A physical interpretation of dispersive transport in disordered semiconductors," *Solid State Communications,* vol. 37, pp. 49-52, 1981.

[67] J. Orenstein and M. Kastner, "Thermalization and recombination in amorphous semiconductors," *Solid state communication,* vol. 40, pp. 85-89, 1981.

[68] A. Miller and E. Abrahams, "Impurity conduction at low concentrations," *Phys. Rev.,* vol. 120, pp. 745-754, 1960.

[69] D. Monroe, "Hopping in the band tails," *Phys. Rev. Lett.,* vol. 54, no. 2, pp. 146-149, 1985.

[70] N. Mott, "Conduction in non-crystalline materials III: Localized states in a pseudogap and near extremities of conduction and valence bands," *Phil. Mag.,* vol. 19, no. 160, pp. 835-852, 1969.

[71] N. Mott and E. Davis, "Conduction in non-crystalline solids," *Phil. Mag.,* vol. 17, pp. 1259-1284, 1968.

[72] J. Anta, I. Mora-Seró, T. Dittrich and J. Bisquert, "Dynamics of charge separation and trap-limited electron transport in TiO2," *J. Phys. Chem. C.,* vol. 111, pp.

13997-14000, 2007.

[73] J. Anta, J. Nelson and N. Quirke, "Charge transport model for disordered materials: Application to sensitized TiO2," *Phys. Rev. B,* vol. 65, p. 125324, 2002.

[74] J. Nelson, "Continuous-time random-walk model of electron transport in nanocrystalline TiO2 electrodes," *Phys. Rev. B.,* vol. 59, no. 23, pp. 15374-15380, 1999.

[75] P. de Jongh and D. Vanmaekelbergh, "Trap-limited electronic transport in assemblies of nanometer-size TiO2 particles," *Phys. Rev. Lett.,* vol. 77, no. 16, pp. 3427-3430, 1996.

[76] V. Dhuzko, V. Timoschenko, F. Koch and T. Dittrich, "Photovoltage in nanocrystalline porous TiO2," *Phys. Rev. B,* vol. 64, p. 075204, 2001.

[77] W. Jaegermann, A. Klein and T. Mayer, "Interface engineering of inorganic thin-fim solar cells - materials science's challenges for advanced physical concepts.," *Adv. Mater.,* vol. 21, no. 42, pp. 4196-4206, 2009.

[78] R. Anderson, "Experiments on Ge-GaAs heterojunctions," *Solid State Electron.,* vol. 5, no. 5, pp. 341-344, 1962.

[79] H. Kroemer, "Barrier control and measurements: abrupt semiconductor heterojunctions," *J. Vac. Sci. technol. b,* vol. 2, no. 3, pp. 433-439, 1984.

[80] R. Street, hydrogenated amorphous silicon, Cambridge: Cambridge university press, 1991.

[81] S. Sze, Physics of semiconductor devices, New York: Wiley, 1985.

[82] J. McCaldin, T. McGill and C. Mead, "Correlation for III-V and II-VI semiconductors of the Au Schottky barrier energy with anion electronegativity," *Phys. Rev. Lett.,* vol. 36, no. 1, pp. 56-58, 1976.

[83] S.-H. Wei and A. Zunger, "Calculated natural band offsets of all II–VI and III–V semiconductors: Chemical trends and the role of cation d orbitals," *Appl. Phys.*

Lett. , vol. 72, p. 2011, 1998.

[84] E. Yu, J. McCaldin and T. McGill, "Band Offsets in Semiconductor Heterojunctions," *Solid state physics,* vol. 46, pp. 1-146, 1992.

[85] J. Tersoff, "Theory of semiconductor heterojunctions: the role of quantum dipoles," *Phys. Rev. B,* vol. 30, no. 8, pp. 4874-4877, 1984.

[86] J. Tersoff, "Band lineups at II-VI heterojunctions: failure of the common-anion rule," *Phys. Rev. Lett.,* vol. 56, no. 25, pp. 2755-2758, 1986.

[87] A. Sasaki and P. Robson, "Carrier transport processes in p-n junctionlayers with a distribution of tra levels," *Solid state electronics,* vol. 34, no. 9, pp. 959-967, 1991.

[88] A. Klein, F. Saeuberlich, B. Saeth, T. Schulmeyer and D. Kraft, "Non-stoichiometry and electronic properties of interfaces," *J. Mater. Sci.* , vol. 42, p. 1890–1900, 2007.

[89] A. Kitai, Principles of solar cells, LEDs and diodes: Role of PN junction, West Sussex, UK: John Wiley & Sons, 2011.

[90] A. Goetzberger, E. Klausmann and M. Schulz, "Interface states on semiconductor/insulator surfaces," *C R C Critical Reviews in Solid State Sciences,* vol. 6, no. 1, pp. 1-43, 1976.

[91] A. Rockett, The materials science of semiconductors, Ney York: Springer science and Business media, LLC, 2008.

[92] M. Peressi, F. Favot, G. Cangiani and A. Baldereschi, "Interface states at ZnSe/Ge heterojunctions: the role of atomic interdiffusion and disorder," *Appl. Phys. Lett.,* vol. 81, pp. 5171-5173, 2002.

[93] L. Peter, "Dynamic aspects of semiconductor photoelectrochemistry," *Chem. Rev.,* vol. 90, pp. 753-769, 1990.

[94] P. Pistor, *Formation and Electronic Properties of In2S3/ Cu(In,Ga)Se2 Junctions and Related Thin Film Solar Cells,* PhD Thesis: Free University Berlin, Germany, 2009.

[95] A. Miller and A. Searcy, "The sublimation of indium sesquisulfide," *J. Phys. Chem.,* vol. 67, pp. 2400-2404, 1963.

[96] P. Pistor, R. Caballero, D. Hariskos, V. Izquierdo-Roca, R. Wächter, S. Schorr and R. Klenk, "Quality and stability of compound indium sulphide as source material for buffer layers in Cu(In,Ga)Se2 solar cells," *Solar Energy Materials & Solar Cells,* no. 93, pp. 148-152, 2009.

[97] P. Pistor, N. Allsop, W. Braun, R. Caballero, C. Camus, C.-H. Fischer, M. Gorgoi, A. Grimm, B. Johnson, T. Kropp, I. Lauermann, H. Mönig, S. Schorr, A. Weber and R. Klenk, "Cu in In2S3: interdiffusion phenomena analysed by high kinetic energy X-ray photoelectron spectroscopy," *Phys. Status Solidi A,* no. 206, p. 1059–1062, 2009.

[98] C.-H. Fischer, R. Koenenkamp, M. Lux-Steiner, J. Moeller and S. Siebentritt, "Verfahren und Anordnung zur Herstellung dünner Metallchalkogenid-Schichten". Germany Patent 198 16 403.7, 1998.

[99] N. Allsop, A. Schönmann, A. Belaidi, H.-J. Muffler, B. Mertesacker, W. Bohner, E. Strub, J. Röhrich, M. Lux-Steiner and C.-H. Fischer, "Indium sulfide thin films deposited by the spray ion layer gas reaction," *Thin Solid Films,* vol. 513, pp. 52-56, 2006.

[100] C.-H. Fischer, H.-J. Muffler, M. Bär, S. Fiechter, B. Leupolt and M. Lux-Steiner, "Ion layer gas reaction (ILGAR) - conversion, thermodynmics and related FTIR," *J. Cryst. Growth,* vol. 241, pp. 151-158, 2002.

[101] J. Möller, C.-H. Fischer, H.-J. Muffler, R. Könenkamp, I. Kaiser, C. Kelch and M. Lux-Steiner, "A novel deposition technique for compound semiconductors on highly porous substrates:ILGAR," *Thin Solid Films,* Vols. 361-362, pp. 113-117, 200.

[102] S. Gledhill, R. Allison, N. Allsop, Y. Fu, E. Kanaki, R. Sáez-Araoz, M. Lux-Steiner and C.-H. Fischer, "The reaction mechanism of the spray Ion Layer Gas Reaction process to deposit In2S3 thin films," *Thin Solid Films,* vol. 519, pp. 6413-6419, 2011.

[103] "Wikipedia, The Free Encyclopedia," [Online]. Available: http://en.wikipedia.org/wiki/Indium%28III%29_chloride. [Accessed 04 07 2013].

[104] "Chemical Book," [Online]. Available: http://www.chemicalbook.com/ChemicalProductProperty_EN_CB3448575.htm. [Accessed 04 07 2013].

[105] K. Miller, S. McCullough, E. Lepekhina, I. Thibau, R. Pike, X. Li, J. Killarney and H. Paterson, "Copper(I) thiocyanate-amine networks: synthesis, structure, and luminescence behavior.," *Inorg. Chem.,* vol. 50, no. 15, p. 7239–7249, 2011.

[106] A. Juma, J. Kavalakkatt, P. Pistor, B. Latzel, K. Schwarzburg and T. Dittrich, "Formation of a disorderd hetero-junction by diffusion of Cu (I) from CuSCN into In2S3 layers: A surface photovoltage study," *Phys. Status Solidi A,* no. 209, p. 663–668, 2012.

[107] G. Kumara, A. Konno, G. Senadeara, P. Jayaweera, D. De-Silva and K. Tennakone, "Dye-sensitized solar cell with the hole collector p-CuSCN deposited from a solution in n-propyl sulphide," *Sol.Energy Mater. & Solar cells,* vol. 69, pp. 195-199, 2001.

[108] H. Bukhru, "Rutherford backscattering spectroscopy," in *Encyclopedia of Materials: Science and Technology (2nd edition)*, Oxford, Elsiever, 2001, pp. 8242-8247.

[109] G. Götz and K. Gärtner, "High Energy Ion beam Analysis of Solids," in *Physical Research*, Berlin, Akademie-Verlag, 1988.

[110] IAEA (International Atomic Energy Agency), "Instrumentation for PIXE and RBS," IAEA;TECDOC-1190, Vienna, Austria, 2000.

[111] W. Chu, J. Mayer and M. Nicolet, Rutherford Backscattering Spectrometry, California: Academic Press Inc, 1978.

[112] T. Alford, L. Feldman and J. Mayer, Fundamentals of Nanoscale Film Analysis, Springer Science and Business Media, Inc, 2007.

[113] D. O'Connor and T. Chunyu, "Appplication of heavy ions to high depth resolution RBS," *Nucl. Instr. and Meth.in Phys. Res. B,* no. 36, pp. 178-188, 1989.

[114] C. Jeynes, N. Barradas, H. Rafla-Yuan, B. Hichwa and R. Close, "Accurate depth profiling of complex optical coatings," *Surf. Interface Anal.,* vol. 30, pp. 237-242, 2000.

[115] N. Barradas, C. Jeynes and R. Webb, "Simulated annealing analysis of Rutherford backscattering data," *Appl. Phys. Lett.,* vol. 71, pp. 291-293, 1997.

[116] U. Barth, "RBS data handling software," Institut für Festkörperphysik, Friedrich-Schiller-Universität Jena, Jena, 2010.

[117] B. Goldstein and D. Szostak, "Surface Photovoltage, band bendng and surface states on a-Si:H," *Surface Science,* no. 99, pp. 235-258, 1980.

[118] J. Lagowski, C. Balestra and H. Gatos, "Photovoltage inversion effect and its application to semiconductor surface studies: CdS," *Surface Science,* no. 27, pp. 547-558, 1971.

[119] A. Goodman, "A method for the measurement of short minority carrier diffusion lengths," *J. Appl. Phys.,* no. 32, pp. 2550-2552, 1961.

[120] L. Kronik, L. Burstein, M. Leivobitch, Y. Shapira, D. Gal, E. Moons, J. Beier, G. Hodes, D. Cahen, D. Hariskos, R. Klenk and H.-W. Schock, "Band diagram of the polycrystalline CdS/Cu(In,Ga)Se2 heterojunction," *Appl. Phys. Lett.,* no. 67, pp. 1405-1407, 1995.

[121] L. Kronik and Y. Shapira, "Surface photovoltage phenomena: theory, experiment, and applications," *Surface Science Reports,* no. 37, pp. 1-206, 1999.

[122] T. Dittrich, "Principles of surface photovoltage (SPV) techniques and applications on solar cell materials: extended lecture at HZB," [Online]. Available: http://www.helmholtz-berlin.de/media/media/forschung/energie/heterogen/eta/methods/spv-techniques-2010-08-09.pdf. [Accessed 05 07 2013].

[123] L. Macor, M. Gervaldo, F. Fungo, L. Otero, t. Dittrich, C.-Y. Lin, L.-C. Chi, F.-C. Fang, S.-W. Lii, C.-H. Tsai and C.-C. Wu, "Photoinduced charge separation in donor-acceptor spiro compounds at metal and metal oxide surfaces: application in dye solar cell," *RCS Advances,* vol. 2, pp. 4869-4878, 2012.

[124] T. Jiang, T. Xie, Y. Zhang, L. Chen, L. Peng, H. Li and D. Wang, "Photoinduced charge transfer in ZnO/Cu2O heterostructure films studied by surface photovoltage technique," *Phys. Chem. Chem. Phys.,* vol. 12, pp. 15476-15481, 2010.

[125] C. Berglund and W. Spicer, "Photoemission studies of copper and silver: theory," *Phys. Rev.,* vol. 136, pp. A1030-A1043, 1964.

[126] S. Gutman, M. Wolak, M. Conrad, M. Beerborn and R. Schlaf, "Effect of ultraviolet and x-ray radiation on the work function of TiO2 surfaces," *J. Appl. Phys.,* vol. 107, pp. 103705-1-8, 2010.

[127] R. Guinebreitiére, X-ray diffraction by polycrystalline materials, London: ISTE Ltd, 2007.

[128] Y. Waseda, E. Matsubara and K. Shinoda, X-ray diffraction crystallography: introduction, examples and solved problems, Berlin: Springer-Verlag Berlin Heidelberg, 2011.

[129] D. Basu, Dictionary of materials science and high energy physics, London: CRC Press LLC, 2001.

[130] S. Sze, Physics of semiconductor devices, New York: John Wiley & Sons Inc., 1969.

[131] N. Barradas, "Rutherford backscattering analysis of thin films and superlattices with roughness," *J. Phys. D: Appl. Phys.* , vol. 34, pp. 2109-2116, 2001.

[132] T. Nakaraha, S. Ohkura, F. Shoji and T. Hanawa, "RBS/channeling study on the annealing behavior of Cu thin films on Si(100) and (111) substrates," *Nucl. Instrum. Methods B,* vol. 45, no. 1-4, pp. 467-470, 1990.

[133] K. Sekar, P. Satyam, G. Kuri, D. Mahapatra and P. Dev, "An RBS study on the annealing behaviour of Cu thin films on brominated Si(111) and Si(100) substrates," *Nucl. Instrum. Methods B,* vol. 71, no. 3, pp. 308-3013, 1992.

[134] A. Cherian, M. Mathew, C. Kartha and K. Vijayakumar, "Role of chlorine on the opto-electronic properties of β-In2S3 thin films," *Thin Solid films,* vol. 518, pp. 1779-1783, 2010.

[135] A. Juma, A. Azarpira, A. Steigert, M. Pomaska, C.-H. Fischer, I. Lauermann and T. Dittrich, "Role of chlorine in In2S3 for band alignment at nanoporous-TiO2/In2S3 interfaces," *J. Appl. Phys.,* vol. 114, no. 5, p. 053711, 2013.

[136] B. Boltaks, Diffusion in Semiconductors, London: Inforsearch ltd, 1963.

[137] Y.-R. Luo, Comprehensive handbook of chemical bond energies, Boca Raton: CRC Press, Taylor & Francis Group, 2007.

[138] N. Revathi, P. Prathap and K. Ramakrishna Reddy, "Thickness dependent physical properties of close space evaporated In2S3 films," *Solid State Sciences,* vol. 11, pp. 1288-1296, 2009.

[139] F. Mesa, W. Chamorro, W. Vallejo, R. Baier, T. Dittrich, A. Grimm and M. Lux-Steiner, "Junction formation of Cu3BiS3 investigated by Kelvin probe force microscopy and surface photovoltage measurements," *Beilstein J. Nanotechnology,* vol. 3, pp. 277-284, 2012.

[140] V. Donchev, K. Kirilov, T. Ivanov and K. Germanova, "Surface photovoltage phase spectroscopy - a handy tool for characterization of bulk semiconductors and

nanostructures," *Mater. Sci. Eng.,* vol. 129, pp. 186-192, 2006.

[141] W. Rehwald and G. Harbeke, "On the conduction mechanism in single crystal beta-Indium sulfide in2S3," *J. Phys. Chem. Solids,* vol. 26, pp. 1309-1324, 1965.

[142] C. Patrick and F. Guistino, "GW quasiparticle bandgaps of anatase TiO2 starting from DFT + U," *J. Phys: Condens. Matter.,* vol. 24, p. 202201, 2012.

[143] G. Liu, W. Jägermann, J. He, V. Sundström and L. Sun, "XPS and UPS Characterization of the TiO2/ZnPcGly Heterointerface: Alignment of Energy Levels," *J. Phys. Chem. B,* vol. 106, no. 23, pp. 5814-5819, 2002.

[144] A. Belaidi and T. Dittrich, "Private communication," *Unpublished,* 2013.

[145] H. Mehrer, Diffusion in solids: Fundamentals, methods, materials, diffusion-controlled processes, New York: Springer-verlag Heidelberg, 2007.

Declaration

I hereby declare that this dissertation is my work and that all other sources and aids used are accordingly acknowledged in the text. To the best of my knowledge, the dissertation contains no materials previously accepted or rejected as insufficient within the context of previous doctoral studies. I also declare that this work was mainly carried out at Helmholtz-Zentrum Berlin für Materielien und Energie in the period between October 2010 and September 2013 under the supervision of PD. Dr. Thomas Dittrich.

List of publications

Journal articles

A. Juma, A. Azarpira, A. Steigert, M. Pomaska, C.-H. Fischer, I. Lauermann and T. Dittrich, "Role of chlorine in In_2S_3 for band alignment at nanoporous-TiO_2/In_2S_3 interfaces," *J. Appl. Phys.,* vol. 114, no. 5, p. 053711, 2013.

A. Juma, P. Pistor, S. Fengler, T. Dittrich and E. Wendler, "Copper diffusion in thin In_2S_3 layers investigated by Rutherford Backscattering Spectroscopy," *Thin Solid Films,* vol. 520, pp. 6740-6743, 2012.

A. Juma, J. Kavalakkatt, P. Pistor, B. Latzel, K. Schwarzburg and T. Dittrich, "Formation of a disorderdhetero-junction by diffusion of Cu (I) from CuSCN into In_2S_3 layers: A surface photovoltage study," *Phys. Status Solidi A,* vol. 209, no. 4, pp. 663-668 2012.

A. Juma, E. Wendler, H.B. Wafula, C.-H. Fischer and Th. Dittrich, "Meyer-Neldel rule of Cu(I) diffusion in In_2S_3 layers," to be submitted.

A. Juma, Th. Dittrich, "Defects at In_2S_3:Cu/CuSCN interfaces," to be submitted.

Conference contributions: oral presentations

A. Juma, P. Pistor, B. Latzel, K. Schwarzburg and Th. Dittrich. "Formation of a disordered heterojunction by diffusion of CU^I from CuSCN into In_2S_3 layers: a surface photovoltage study." *13th International conference on formation of semiconductor interfaces (ICFSI-13)*, Prague, Czech Republic, July 3 - 8 2011.

A.O. Juma, P. Pistor, S. Fengler, Th. Dittrich, E. Wendler. "Diffusion of Cu (I) in In_2S_3 thin films investigated by Rutherford backscattering spectroscopy (RBS)." *76th Annual Meeting of the DPG and DPG Spring Meetin, Berlin, Germany*, 25 - 30 of March 2012.

A. Juma, R. Sáez-Araoz, Ch-H. Fischer, and Th. Dittrich. “Copper diffusion in In_2S_3 layers deposited by spray-ion layer gas reaction (ILGAR) method.” *DPG Spring Meeting Regensburg, Germany*, 10 - 15 March 2013.

Conference contributions: Poster presentations

Juma, A. Azarpira, Ch-H. Fischer, and Th. Dittrich. “Role of Cl in In_2S_3 for band alignment at nanoporous-TiO_2 / In_2S_3 interfaces.” *DPG Spring Meeting, Regensburg, Germany*, 10 - 15 March 2013.

Albert O. Juma, Anahita Azarpira, Rodrigo Sàez Araoz, Christian-Herbert Fischer, and Thomas Dittrich, “Penetration of In_2S_3 and Sb_2S_3 deposited by ion layer gas reaction into nanoporous - TiO_2,” *EMRS spring meeting, Strasbourg, France*. 27-31 May 2013.

Albert Owino Juma, Rodrigo Sáez-Araoz, Christian-Herbert Fischer and Thomas Dittrich, “Diffusion of copper in In_2S_3 layers prepared by ion layer gas reaction method,” *EMRS spring meeting, Strasbourg, France*. 27-31 May 2013.

Acknowledgements

This work is complete because of the support, both direct and indirect, of several people and institutions, whom I would like to appreciate at this point. First and foremost I greatly thankful to the Germany academic exchange services (DAAD) for offering a scholarship to come to Germany to pursue my doctoral studies. I also thank Prof. Lux-Steiner for allowing me to work in her department at Helmholtz-Centre Berlin (HZB). In the same breathe, I appreciate very much my supervisor and mentor Dr. Thomas Dittrich for accepting me as his student and for his tireless and professional guidance and training during my entire research work. I am also grateful to Prof. Weinelt for accepting to be my second examiner.

I thank Dr. Wendler of Jena University for accepting and training me in RBS measurements and analysis, together with the technician Mr Barth and her student Phillip. Thanks to Prof. Baradas and Prof. Meyer for the discussions and consultations regarding RBS analysis.

I am grateful to the ILGAR group at HZB led by Prof. Fischer for allowing me to use their laboratory facilities for deposition of In_2S_3 layers. Thanks to Paul Pistor for providing thermally evaporated In_2S_3 layers and for the constructive discussions. Thanks to Iver Lauermann and Alex Steigert for UPS measurements.

Thanks to group mates Elisabeth Zillner and Stefan Fengler for constructive discussions regarding SPV experiments, and especially for Stefan for assistance with simulation of diffusion profiles.

I thank Jaison Kavalakatt and Xianzong Lin for assistance in XRD and SEM measurements, Björn Latzel for introducing me to the deposition of CuSCN, Anahita Azarpira and Henry Wafula for working together in the labs. Thanks also to Rodrigo Aráoz-Saez, Jesús Martinez and Isabel Fernández for corrections and feedback. I also thanks Amina Grunewald for assistance with administrative work.

Last but not least, I am very grateful to my wife Esther and kids Purity and Pelaiah for their patience, motivation and understanding during my studies.

Curriculum Vitae

For reasons of data protection, the Curriculum vitae is not published in the online version”